Numerical Modelling of Photonic Crystal Based Switching Devices

Ramsey Selim

A submission presented in partial fulfilment of the requirements
of the University of Glamorgan/Prifysgol Morgannwg
for the degree of Doctor of Philosophy

This research programme was carried out in collaboration
with the Engels' Historical Society

February 2010

Acknowledgements

"It is the glory of God to conceal a matter;

to search out a matter is the glory of kings" - Proverbs 25:2

First, I would like to express my deepest gratitude and appreciation to my project supervisor Prof. Salah Obayya. He identified the potential in me, and unlocked the research within. His guidance, continuous encouragement, skilful academic excellence, and brilliant scientific mind have played the major role in the progress, development, and success of my research career.

I would also like to thank Dr. Domenico Pinto, and Dr. Rosa Letizia for their valuable input academically and non-academically. They have had a positive lasting impact on me.

I wish to mention Mo, and the 24 crew, Anna, Jonny, Matt, "Sam," Steph, and Dr. Trevor Dodds, who have all had a great influence in keeping me motivated throughout this PhD journey, when things made no sense, they made the PhD life look all the brighter and gave me the extra push when I needed one.

Mr. and Mrs. Brain, Mr. and Mrs. Sunderland, and Dr. and Dr. Payne, I thank them for their commitment to my cause, the PhD, for giving me a place to stay when I needed one, and for being there for me every time and all the time.

To my dearest parents, Prof. and Mrs. Selim, and to my dear siblings, Suzanne, Sam and Adam; I will never be able to repay them for their absolute backing and support to me, meeting my needs before I knew I needed them. They have a special place in my heart.

My beloved, my wife, Naomi, her prayers, patience, hard work, energy, dedication, enthusiasm, passion, support, and, most of all, her love; to these I owe where I stand today.

Finally, to Him that made all this possible, the Rock of my foundation, my God, I thank.

Abstract

In the last few years research has identified Photonic Crystals (PhCs) as promising material that exhibits strong capability of controlling light propagation in a manner not previously possible with conventional optical devices. PhCs, otherwise known as Photonic Bandgap (PBG) material, have one or more frequency bands in which no electromagnetic wave is allowed to propagate inside the PhC. Creating defects into such a periodic structure makes it possible to manipulate the flow of selected light waves within the PhC devices outperforming conventional optical devices. As the fabrication of PhC devices needs a high degree of precision, we have to rely on accurate numerical modelling to characterise these devices.

There are several numerical modelling techniques proposed in literature for the purpose of simulating optical devices. Such techniques include the Finite Difference Time Domain (FDTD), the Finite Volume Time Domain (FVTD), and the Multi-Resolution Time Domain (MRTD), and the Finite Element (FE) method among many others. Such numerical techniques vary in their advantages, disadvantages, and trade-offs. Generally, with lower complexity comes lower accuracy, while higher accuracy demands more complexity and resources.

The Complex Envelope Alternating Direction Implicit Finite Difference Time Domain (CE-ADI-FDTD) method was further developed and used throughout this thesis as the main numerical modelling technique. The truncating layers used to surround the computational domain were Uniaxial Perfectly Matched Layers (UPML). This thesis also presents a new and robust kind of the UPML by presenting an accurate physical model of discretisation error.

This thesis has focused on enhancing and developing the performance of PhC devices in order to improve their output. An improved and new design of PhC based Multiplexer/Demultiplexer (MUX/DEMUX) devices is presented. This is achieved using careful geometrical design of microcavities with respect to the coupling length of the propagating wave. The nature of the design means that a microcavity embedded between two waveguides selects a particular wavelength to couple from one waveguide into the adjacent waveguide showing high selectivity.

Also, the Terahertz (THz) frequency gap, which suffers from a lack of switching devices, has been thoroughly investigated for the purpose of designing and simulating potential PhC based switching devices that operate in the THz region.

The THz PhC based switching devices presented in this thesis are newly designed to function according to the variation of the resonant frequency of a ring resonator embedded between two parallel waveguides. The holes of the structures are filled with polyaniline electrorheological fluids that cause the refractive index of the holes to vary with applied external electric field. Significant improvements on the power efficiency and wavelength directionality have been achieved by introducing defects into the system.

Table of Contents

List of Tables

List of Figures

List of Abbreviations

1D	One Dimensional
2D	Two Dimensional
3D	Three Dimensional
ABC	Absorbing Boundary Conditions
ADI	Alternating Direction Implicit
ADI-FDTD	Alternating Direction Implicit Finite Difference Time Domain
BC	Boundary Conditions
C1	Cavity One
C2	Cavity Two
CL	Cavity Length
CW	Continuous Wave
CE-ADI-FDTD	Complex Envelope Alternating Direction Implicit Finite Difference Time Domain
DRL	Direct Reflection Losses
DEL	Discretisation Error Losses
E-Field	Electric Field
EM	Electromagnetic
FDTD	Finite Difference Time Domain
FFT	Fast Fourier Transform
GaAs	Gallium Arsenide
H-Field	Magnetic Field
MUX/DEMUX	Multiplexer/Demultiplexer
P1	Port One

P2	Port Two
PBG	Photonic Bandgap
PEC	Perfect Electric Conductor
PhC	Photonic Crystal
PCF	Photonic Crystal Fibre
PCW	Photonic Crystal Waveguide
PML	Perfectly Matched Layers
SiO_2	Silicon Oxide
SP-PhC	Surface Plasmonic Photonic Crystal
SVEA	Slowly Varying Envelope Approximation
TE	Transverse Electric
THz	Terahertz
TM	Transverse Magnetic
UPML	Uniaxial Perfectly Matched Layers
WG	Waveguide
WG1	Waveguide One
WG2	Waveguide Two

Chapter 1

Introduction

1.1 Photonic Crystals

The Photonic Crystal (PhC) is a periodic arrangement of a dielectric or metallic structure. It is a new material that has gained much attention amongst researchers due to its ability to control the propagation of optical waves. This ability is made possible through what is known as the Photonic Bandgap (PBG) [1]. The PBG is a frequency range in which electromagnetic (EM) wave is not permitted to propagate inside the PhCs.

Photonic crystal devices are in the $nm - \mu m$ range. This minute size requires complex fabrication techniques that depend on highly accurate simulations of realistic performances of PhC devices. Hence, realistic simulations that accurately predict the

performance of the PhC devices are of major importance. There are many benefits of these simulations, some include;

1. Saving time and cost of re-fabrication.
2. Accurate analytical simulations leading to modifications and enhancements of the PhC device that in turn leads to better developed designs.

1.2 Numerical Techniques

There are several techniques for modelling PBG structures. One of the techniques highly appreciated for its robustness is the Complex Envelope Alternating Direction Implicit Finite Difference Time Domain (CE-ADI-FDTD) method [2]. The advantage of this method is that it overcomes the Courant limitations in stability problems without sacrificing in the accuracy of the results, as well as saving simulation running time. In this method there exists the Perfectly Matched Layer (PML) boundary conditions that maintain uniform physical parameters such as the permittivity (ε), permeability (μ) and electric conductivity (σ). However, this research presents new additions and contributions to the CE-ADI-FDTD PML by introducing gradual profile attenuation that results in overall better performance of the system.

1.3 Motivations

A Photonic Crystal Waveguide (PCW) can be constructed by creating linear defects in the PBG structures. PCWs permit directed light transmission for frequencies inside the PBG. PBG waveguides are of interest because of their potential ability for strongly controlling the propagation of light, with the prospect of the design and

development of PBG-based directional couplers for multiplexing/demultiplexing (MUX/DEMUX) applications [3].

As it stands now, fabrication of PhC devices require ultra-high degree of precision in addition to highly complicated laboratory facilities. Therefore, modelling looks as the most reliable tool to rely on when designing such devices: in the range of *μm* even *nm* dimensions.

Recently, Obayya *et al.*, have developed the versatile and powerful CE-ADI-FDTD which has a number of advantages:

1. It is unconditionally stable.
2. It has no limit on time-step size.
3. It is numerically efficient.

However, one drawback that still exists is the truncation of computational domain. Starting from this point, the main aim of the thesis was drafted around the development of a new perfectly matched layer CE-ADI-FDTD technique, and apply it to design a number of various photonic switches.

To meet this aim, the following milestones have been set:

1. Create new PML-CE-ADI-FDTD.
2. Numerical assessment of the PML-CE-ADI-FDTD through comparisons with results in literature.
3. New designs of PhC switching devices that are highly efficient in their transmission and crosstalk. The assessed new PML-CE-ADI-FDTD was used as the numerical modelling technique.
4. Investigation of ring resonator performance in the Terahertz (THz) range.

5. Suggest and demonstrate a novel design of THz switch based on PhCs.

1.4 Outline of the Thesis

This thesis presents the outcomes of thorough investigations carried out with a two-fold focus; using existing photonic crystal technology to create high performance optimised optical devices, and the simulation of such devices with existing or enhanced numerical modelling techniques. Such improved numerical techniques and photonic crystal designs have been extensively investigated with careful attention to the accuracy of simulation results, the computational burden or resources required, as well as the sensitivity of those designs. In order to do so, the thesis has been organised as follows.

In chapter 2 the features of the photonic crystal technology are described and their many benefits explained. This covers all the necessary mathematical, physical, and material properties which are all well established in literature. The optical properties of PhCs are gradually analysed – starting with forms of a one-dimensional (1D) crystal, that is useful for understanding the properties of photonic crystal structures such as the bandgap phenomenon. Also, electromagnetic derivations based on the one-dimensional photonic crystal can be extended and applied in the analysis of more complex structures including the two-dimensional (2D) photonic crystals. The end of this chapter, emphasis is placed upon defects in the PhC structure; this includes point defects, *cavities*, and line defects, *waveguides*. Cavities and waveguides can be easily designed by engineering a defect inside the geometry of a periodic lattice.

Chapter 3 gives an in depth and comprehensive investigation of the computational techniques used. The emphasis here is on the Finite-Difference-Time-

Domain (FDTD), its advantages and main drawbacks. After this, existing solutions to these drawbacks are covered through the Alternating-Direction-Implicit FDTD (ADI-FDTD) and the CE-ADI-FDTD techniques.

In chapter 4, analytical Absorbing Boundary Conditions (ABCs) and PML ABCs are reviewed. The emphasis here is on the Uniaxial PML (UPML) boundary conditions for the CE-ADI-FDTD. Since many electromagnetic interaction problems modelled using FDTD are defined in regions where the spatial domain of the computed field is unbounded in one or more coordinate directions, and computers cannot store an unlimited amount of data. Therefore, boundary conditions are introduced at the outer lattice boundary to simulate the extension of the lattice to infinity. In the end of this chapter, a new PML technique that accounts for error discretisation is introduced with comprehensive analysis on the implementation of this technique in the CE-ADI-FDTD method.

In chapter 5 several examples have been analysed in order to assess the new formulation of the PML boundary conditions for the CE-ADI-FDTD in the context of optical slab waveguide devices.

Chapter 6 presents and investigates novel designs of PhC based switching devices. These switches perform multiplexing and demultiplexing upon the selected frequencies of the signal excited into the structure. These switches are based on careful geometrical design of cavities with respect to the coupling length of the required output wave.

In chapter 7, ring resonator switches based on a PhC structures in the Terahertz (THz) range are presented. In particular, this chapter investigates the enhancement of existing optical THz region PhC based devices. The numerical technique used here is

CE-ADI-FDTD method.

Finally, in Chapter 8, conclusions and final remarks of the presented research are drawn, and a view of the potential future topics is given.

Chapter 2

Photonic Crystals

2.1 Introduction

This chapter gives a rigorous overview of the photonic crystals, otherwise known as photonic bandgap structures, and their properties. The chapter covers some essential background theory, and Maxwell's equations, which in turn shed light on the origin of the bandgap. The properties of the one and two dimensional PhCs are presented, as well as the case of the PhC slab and creating defects in PhC structures.

2.2 Background

Over the last two decades, ever since the pioneering work of Yablonovitch in the late 1980's [1], photonic crystals have gained much attention and have been comprehensively investigated. These photonic bandgap structures started off as eligible candidates to enhance the material properties of spontaneous light-emitters. However, it did not take long before their dispersive properties and strong capability for selecting specific wavelengths were identified and implemented in optical communications.

The periodicity of the refractive index along one or more directions of the photonic crystal structure gives it a photonic bandgap. This photonic bandgap is a frequency range in which no electromagnetic wave is allowed to propagate. It has a similar effect as an electronic bandgap has on electrons, which gives electrical semiconductors their properties [4]. From a practical point of view, photonic crystals are an excellent base system to build compact, integrated optical circuits, as the PBG confines and directs light and thus has many potential applications in optical communications and computing, including, but not limited to, devices with sharp bends [5], filters [6-7], cavities [8-9], and lasers [11], [12].

Such a medium, impenetrable by light, enables the manipulation of the lightwaves by creating channels in the material that act as optical "wire", or making cavities in the middle of the crystal that act as optical "wells" where light modes resonate.

Photonic crystals exist in nature, producing the iridescent colours of soap bubbles, butterfly wings, seashells, and some gemstones. This occurs as a direct effect of an alternation of layers of two substances, or two arrangements of the same substance

in the surface material of the object. However, this alternation is only periodic in one direction, that is, 1D photonic crystals, as shown in Fig. 2.1. Such cases in nature usually have a narrow bandgap, and as the angle of view changes, the periodicity in that direction also changes causing different colours to be reflected producing shimmering light [4].

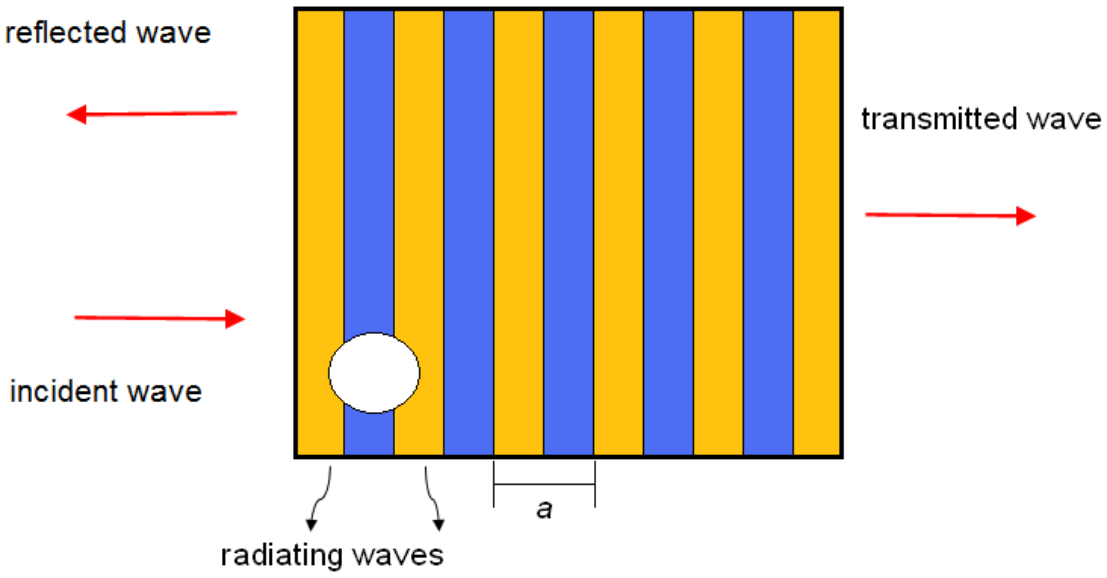

Figure 2.1 Schematic diagram of a 1D PhC with alternating dielectric layers represented by orange and blue

2.3 Maxwell's Equations

This section will review the main manner by which an electromagnetic wave travels through a dielectric medium. This review focuses on the properties of Maxwell's equations, and the Bloch-Floquet theorem in order to better discuss the origin of the bandgap in photonic crystals, which follows in the next section.

There are four electromagnetic field vectors that govern the electromagnetic

phenomena. These four electromagnetic vectors are functions of both position r [m] and time t [s] [12]. The electromagnetic field can be described by electric flied E [V/m], magnetic field H [A/m], electric flux density D [C/m^2], and magnetic flux density B [Wb/m^2]. These electromagnetic field vectors all conform to the Maxwell's equations as follows

Gauss' law for the electric field: $$\nabla \bullet D = \rho \quad (2.1)$$

Gauss' law for the magnetic field: $$\nabla \bullet B = 0 \quad (2.2)$$

Faraday's law: $$\nabla \times E + \frac{\partial B}{\partial t} = 0 \quad (2.3)$$

Ampere's law: $$\nabla \times H + \frac{\partial D}{\partial t} = J \quad (2.4)$$

Constitutive relationships: $$B = \mu_0 H \quad (2.5)$$

$$D = \varepsilon_0 \varepsilon_r E \quad (2.6)$$

Here, J [A/m^2] is the electric current density, and ρ [C/m^3] is the charge density of free space [13].

The above equations can fully describe the electromagnetic wave propagation through any medium, including dielectric materials, which are of special interest in this research. As the research is primarily dedicated to photonic crystal waveguides, the focus here is on electromagnetic wave propagation in dielectric medium, especially in a two-dimension photonic crystal waveguide. These PCWs will be discussed in detail later in this chapter.

In optical communication the importance is usually only in cases where no free charge densities or free current densities are included, $\rho = 0$, and $J = 0$. Then, combining equations (2.1) – (2.6) leads to the wave equation

$$\nabla \times \left(\nabla \times E(r)\right) + \left[1 - \varepsilon(r)\right] \cdot \frac{\omega^2}{c^2} \cdot E(r) = \frac{\omega^2}{c^2} \cdot E(r) \tag{2.7}$$

where c is the speed of light in vacuum. It can be noticed that this formula is very similar to Schrödinger's equation from quantum mechanics [4].

Since this medium is not ferromagnetic, Eq. (2.7) can be solved for the magnetic field, H, as follows

$$\nabla \times \frac{1}{\varepsilon(r)} \nabla \times H(r) = \left(\frac{\omega}{c}\right)^2 \cdot H(r) \tag{2.8}$$

Eq. (2.8) is known as the master equation as it, alongside the divergence equations (2.5) and (2.6), fully describes the magnetic field for a given problem. It should be noted here that the eigenvectors *H(r)* are the spatial patterns of the harmonic modes. The eigenvalues $\left(\frac{\omega}{c}\right)^2$ are proportional to the squared frequencies of those modes, and is the solution to the eigenvalues problem with an Hermitian operator $\nabla \times \frac{1}{\varepsilon} \nabla \times$. Consequently, the eigenvalues are real, and the magnetic field modes are orthogonal and can be categorised according to the symmetry properties [4, 14].

The periodic dielectric constant, $\varepsilon(r)$, with period R can be written as

$$\varepsilon(r) = \varepsilon(r + a) \tag{2.9}$$

This periodicity means that the Bloch-Floquet theorem can be applied. The Bloch-Floquet theorem simply shows that Hermitian eigen problems with operators that are periodic functions of position have solutions that are always from the periodic function $u_{n,k}(r)$, A corollary of the Bloch-Floquet theorem is that the wavevector $\vec{k}$ is a conserved quantity, and therefore, propagating waves with a fixed $\vec{k}$ cannot scatter, and as another consequence of the Bloch-Floquet theorem is that the solutions are periodic

as a function of the wavevector, $\vec{k}$ [4].

Hence, applying the Bloch-Floquet theorem for a periodic ε, the master equation, Eq. (2.8), becomes

$$H_{n,k}(r) = e^{jk\cdot r} u_{n,k}(r), \tag{2.10}$$

where $u_{n,k}$ has the periodicity of the crystal lattice.

k is repeated outside the Brillouin zone causing the angular frequency, ω, to fold back into the Brillouin zone when it reaches the edges. The angular frequency, which is a function of the wavevector, is organised as bands that are described by index n. Consequently, all modes are described in the first Brillouin zone by the wavevector k, and the integer index n.

Expanding the Bloch modes and the inverse of the dielectric into Fourier series on the reciprocal vector of the lattice, G, leads to an explicit solution of the master equation Eq. (2.8).

$$\eta(r) = \frac{1}{\varepsilon(r)} = \sum_G \eta_G e^{jk\cdot r} \text{ , where } a_i \bullet b_j = 2\pi\delta_{ij}, \text{ with } a_i = G, \text{ and } b_j = a \tag{2.11}$$

$$\vec{H}_{n,k}(r) = \sum_G u_G^{n,k} e^{j(k+G)\cdot r} \tag{2.12}$$

Then, appropriately substituting the Fourier series into Eq. (2.8) gives a set of infinite linear eigenvalue equations

$$\sum_G \eta_{G-G'}(k+G') \times \left[(k+G) \times u_G^{n,k}\right] = \frac{\omega_n(k)^2}{c^2} u_{G'}^{n,k}, \text{ for all } G' \tag{2.13}$$

The mode that corresponds to vector k is exactly the same as the mode at $k + G$ that corresponds to an increment of $G \bullet a$ at multiple integers of 2π. This occurs as a result of the translational symmetry property of the periodic structure [15]. Hence, k can

be investigated within a finite range of values where non redundant modes are obtained. This range is called Brillouin zone and is

$$-\frac{\pi}{a} < k \leq \frac{\pi}{a} \tag{2.14}$$

2.4 Origin of the Bandgap

A photonic bandgap is a range of frequencies, ω, into which there intrude no propagating solutions, real k, for any vector k and is surrounded by propagation states, $\omega(k)$, above and below the prohibited gap. Such bandgaps can be incomplete or complete bandgaps, where incomplete bandgaps refer only to specific wavevectors k, polarisations and/or symmetries. Whereas a complete, or omnidirectional, bandgap is one in which gaps at all k points overlap for a given frequency range. Nevertheless, the idea behind the origin of various bandgaps is still the same and can be made clear by considering periodicity in a simple one-dimensional system.

2.4.1 One-dimensional photonic crystal

Looking closely at a one-dimensional uniform system, as in Fig. 2.2, where ε = 1, in which $\omega(k) = ck$ are the planewave eigensolutions as shown in Fig. 2.3. The periodicity of this uniform system is a trivial periodicity a, where $a \geq 0$ at which point, a = 0 gives the usual unbounded dispersion. In the case that $a \neq 0$ Bloch's theorem with artificial periodicity a such that $|k| > \frac{\pi}{a}$ means that bands are folded into the first Brillouin zone, which is expressed by the dashed line in Fig. 2.3 [15]. In this figure, it can be noticed that the result of the artificial period is that $k = -\frac{\pi}{a}$ mode is equivalent to

$k = \frac{\pi}{a}$ mode. This can be expressed by the following linear combinations

$$e(x) = \cos\left(\frac{\pi \cdot x}{a}\right) \tag{2.15}$$

$$o(x) = \sin\left(\frac{\pi \cdot x}{a}\right) \tag{2.16}$$

where $\omega = \pi / a$ as in Fig. 2.4.

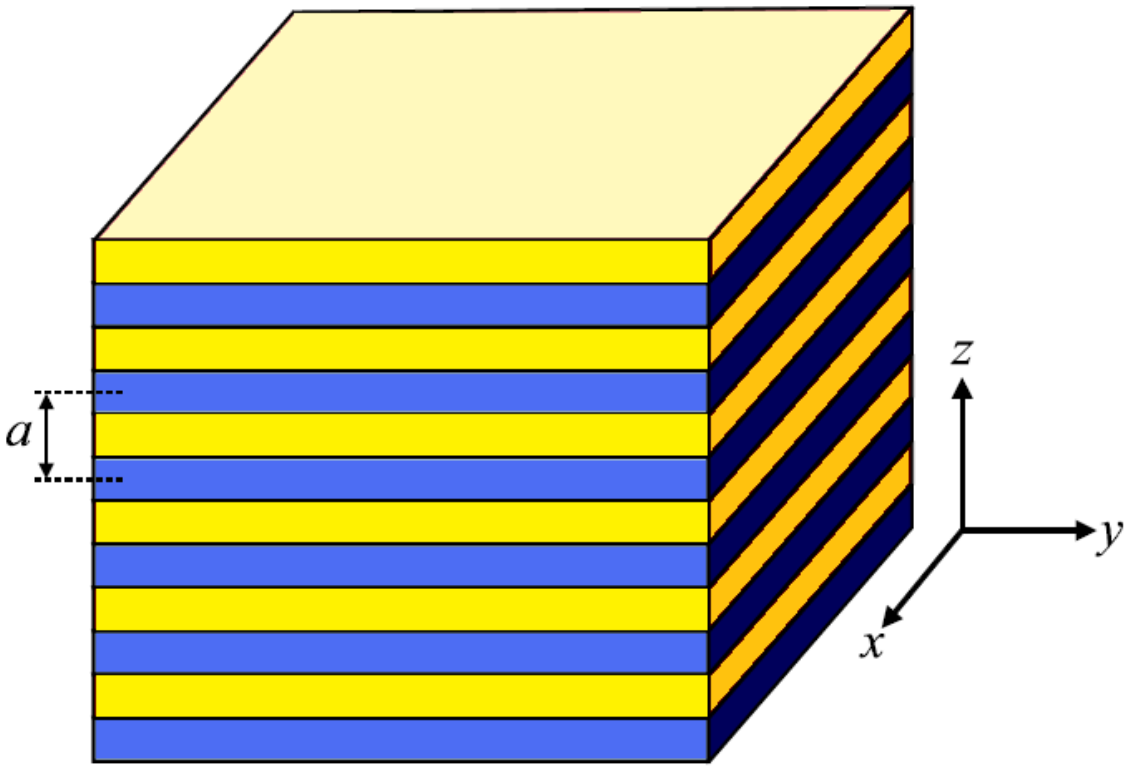

Figure 2.2 One-dimensional photonic crystal known as multilayer film or Bragg mirror. It is composed of infinitely extended layers of two types of dielectric material repeated in the *z*-direction with a period *a*.

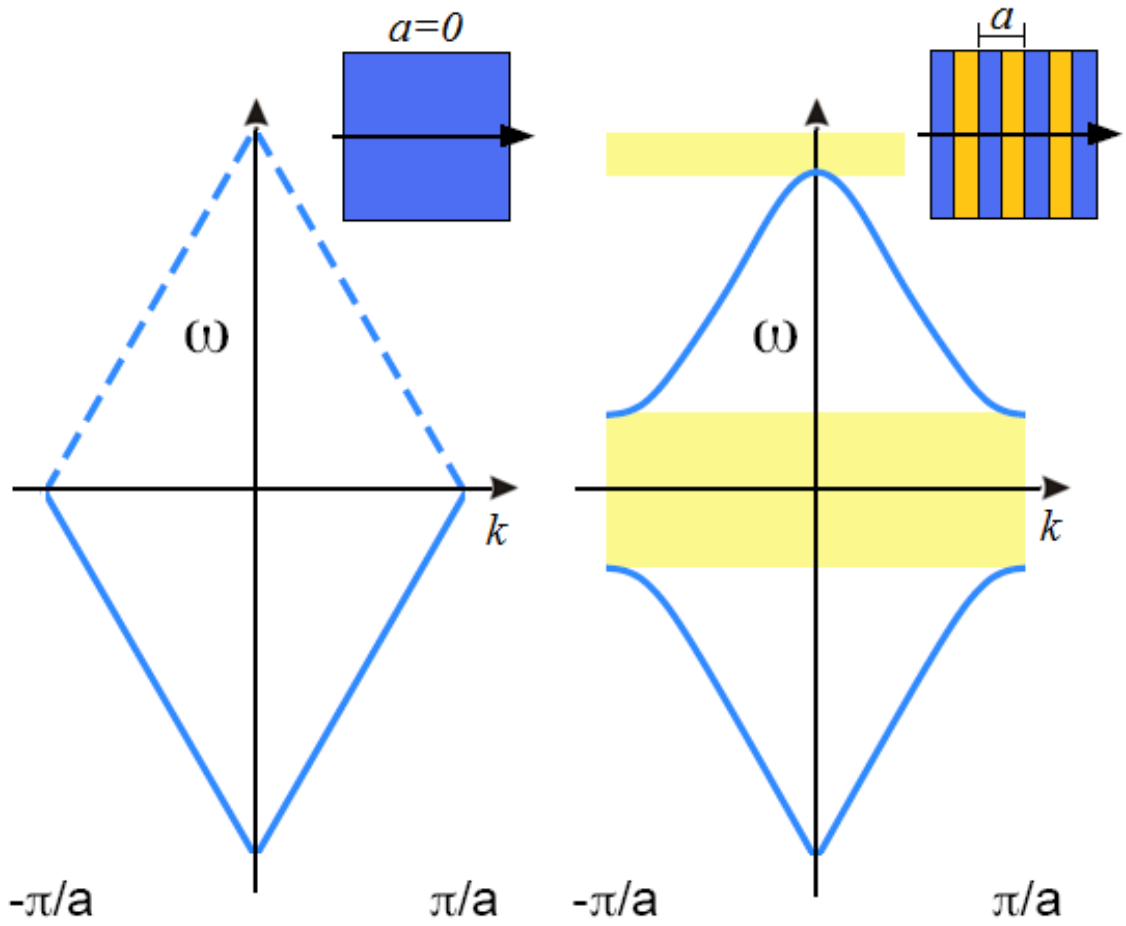

Figure 2.3 Dispersion relation, ω vs. k, for a uniform 1D structure with artificial periodicity a (on the left), and with actual periodicity a (on the right). Folding can be seen when adding the periodicity in Bloch's theorem by the dashed lines on the left while on the right the gap due to the split degeneracy at $k = \pm\pi/a$ is seen.

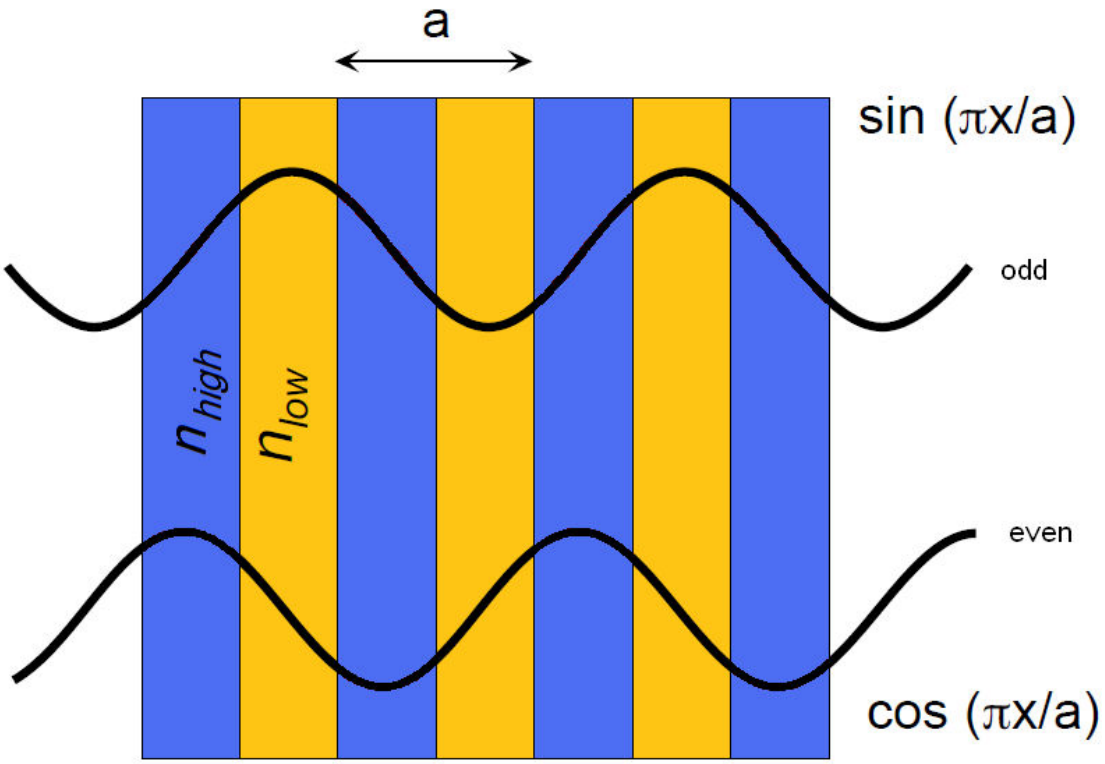

Figure 2.4 Schematic origin of the bandgap in 1D. The degenerate $k = \pm \pi/a$ planewaves of a uniform medium are split into $\cos(\pi x/a)$ and $\sin(\pi x/a)$ standing waves by a dielectric periodicity, forming the lower and upper edges of the bandgap, respectively—the former has electric-field peaks in the high dielectric (n_{high}) and so will lie at a lower frequency than the low dielectric (n_{low}) that lies at a higher frequency.

For a periodic function ε with period a, sinusoidal or square wave like in shape, as shown on the right in Fig. 2.3 there exists an oscillating "potential". This oscillating potential causes the accidental degeneracy between the waves $e(x)$ and $o(x)$ to be broken. This happens when $\Delta > 0$, $e(x)$ field concentrates inside the dielectric of higher ε. Thus, it lies at the lower frequencies, whereas for $o(x)$ the opposite occurs, as shown in Fig. 2.4. This shift of the bands causes the formation of a bandgap as shown on the

right side in Fig. 2.3. It should be noted here that in one-dimensional photonic crystals the bandgap always appears for any index contrast as soon as $\varepsilon_1 \neq \varepsilon_2$. This relationship is proportional; the smaller the contrast, the smaller the bandgap size [14].

2.4.2 Evanescent modes in photonic bandgaps

If an external source is used to excite a 1D photonic crystal with an electromagnetic wave, and the frequency of the electromagnetic wave is within the range of the photonic bandgap of that particular crystal, then the EM wave will not propagate inside the crystal but will decay exponentially. These modes are known as evanescent and can be represented as

$$H(r) = e^{ikr}u(r)e^{-kr} \tag{2.17}$$

These evanescent modes are categorised as Bloch modes, expressed by Eq. (2.10). However, the wavevector is a complex quantity and not real. The imaginary component of the wavevector, $k + j\kappa$, causes the decay of the mode at a rate of $1 / \kappa$. The origin of these evanescent modes can be explained approximating the second band near the gap, shown on the right in Fig. 2.3, by expanding $\omega_2(k)$ in powers of k about the zone edge $k = \frac{\pi}{a}$. Because of time-reversal symmetry [14–18], the expansion cannot contain odd powers of k, giving

$$\Delta\omega = \omega_2(k) - \omega_2\left(\frac{\pi}{a}\right) \approx \alpha\left(k - \frac{\pi}{a}\right)^2 = \alpha(\Delta k)^2 \tag{2.18}$$

where α is a constant that depends on the curvature of the band (i.e. the second derivative). For frequencies higher than the top of the gap, $\Delta\omega > 0$, Δk is real and the modes are within the second band. However, for $\Delta\omega < 0$, $\Delta k = jk$ which is an imaginary quantity that leads to the states decaying exponentially, and the modes are within the

bandgap. The variation of κ throughout the gap is displayed in Fig. 2.5. Derivations can be made to show that larger gaps usually result in larger κ at the centre and thus less light can propagate into the crystal. Although evanescent modes are genuine solutions of the eigenvalue problem, they diverge as z goes to $\pm\infty$. In an ideal crystal of infinite dimensions, there is no physical way to excite one of these modes. Then again, the existence of a defect in an otherwise pure crystal may break this exponential growth and sustain a mode. If the geometry and symmetry of the defect is compatible with one of these evanescent modes then a state can be localised at the centre of the gap much more tightly than modes near to the edge of the gap [14], and [18]. Examples of defects that can be placed in a one−dimensional photonic crystal are shown in Fig. 2.6.

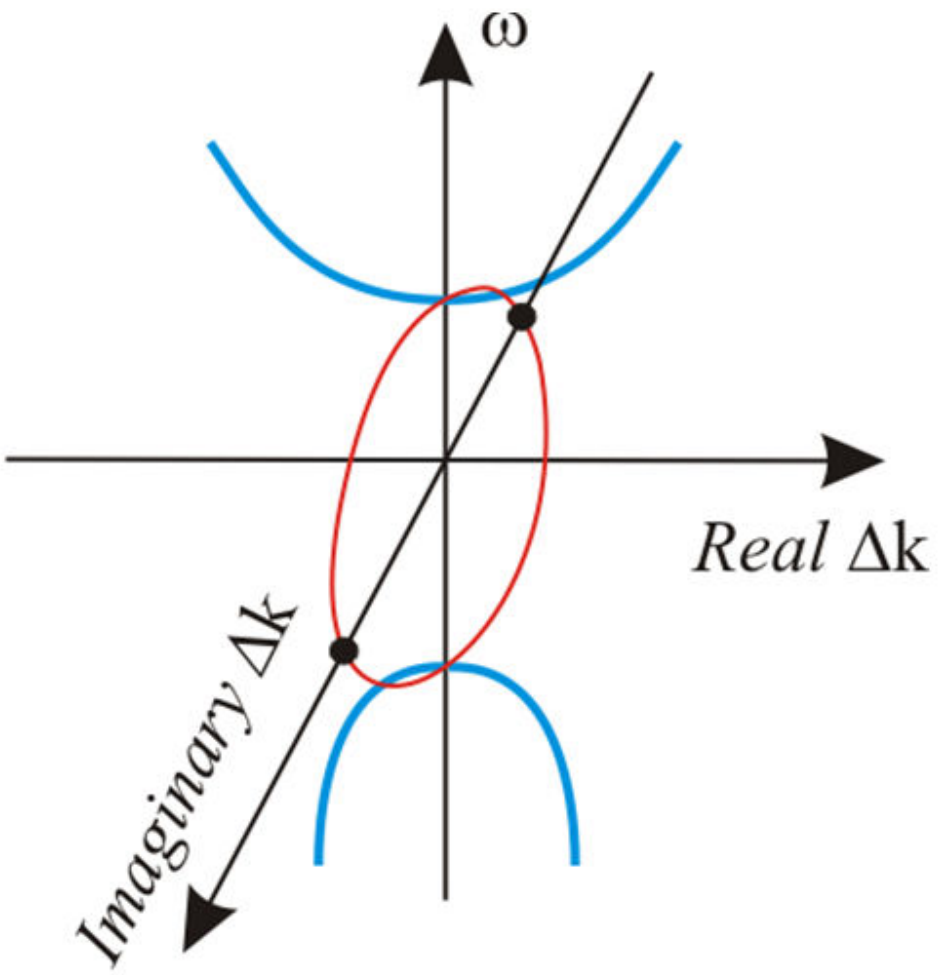

Figure 2.5 Schematic illustration of the complex band structure of a multilayer film. The upper and lower blue lines correspond to the edges of band 2 and band 1, respectively. The possible evanescent states in the red band.

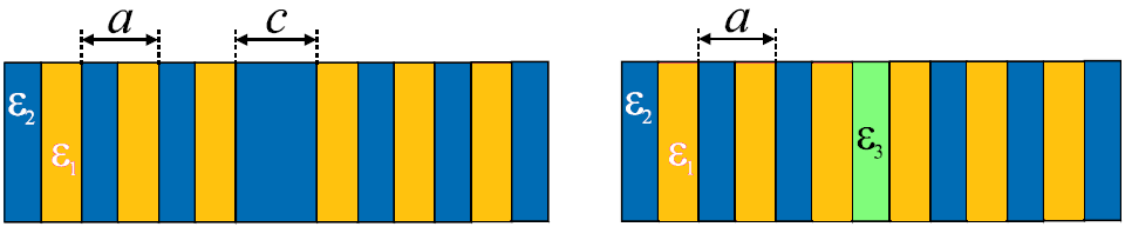

Figure 2.6 a) Defect for a 1D PhC by changing the width of one of the layers.

b) Defect created by changing the dielectric constant in one of the layers.

In Fig. 2.6 a, the defect has been created by varying the thickness of one of the layers of the photonic crystal. Whereas, in Fig. 2.6 b, the defect was created by introducing a layer of dielectric material with a different dielectric constant then that of the dielectric material used to make the crystal. In both cases it is possible to localise a mode in the defect, with respect to the geometry of the defect and the frequency range of the bandgap of the crystal.

2.5 Two-Dimensional Photonic Crystals

For a two-dimensional photonic crystal the periodicity is along two directions, while it is homogeneous along the third. This type of structure makes manipulating the direction of the propagation of light along a plane possible. A classic layout is shown in Fig. 2.7 for a 2D square lattice of dielectric pillars in air.

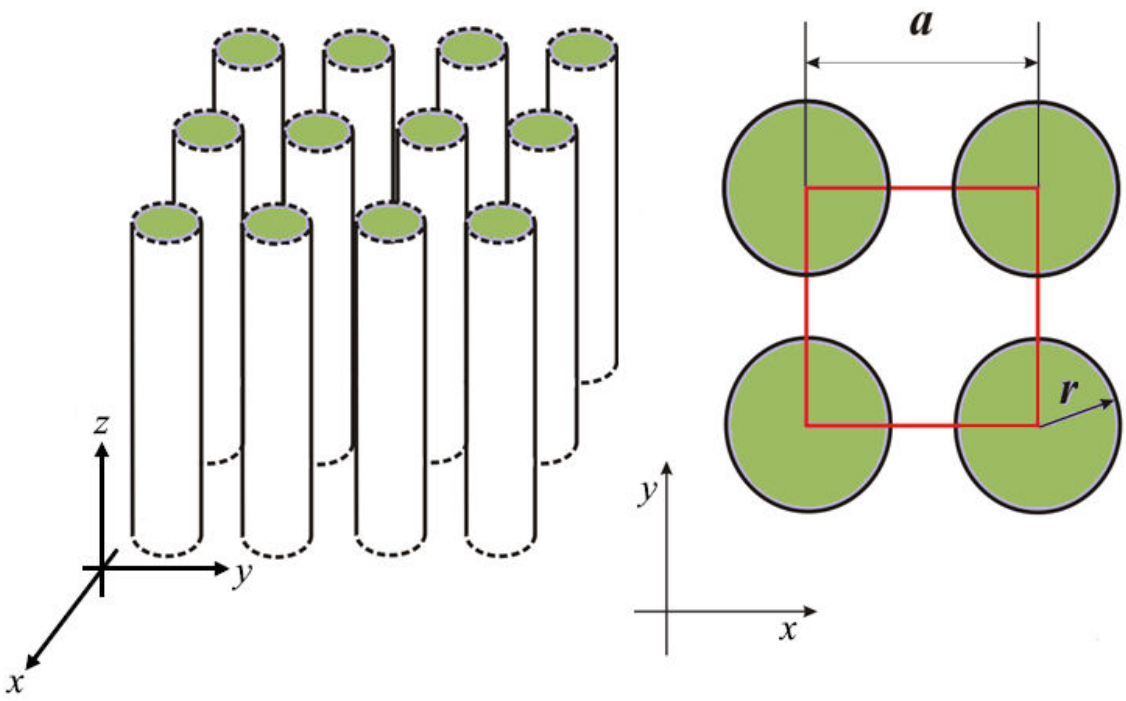

Figure 2.7 2D PhC square lattice of dielectric pillars with radius *r* in air with period *a*. The inset on the right displays the in-plane view of the structure where the unit cell is highlighted in red.

The key to understanding photonic crystals in two dimensions is to understand that the components in 2D can be split into two polarisations according to their symmetry: Transverse Magnetic (TM), where the magnetic field is in the *xy* - plane and the electric field is perpendicular in the *z* - direction; and Transverse Electric (TE), where the electric field is in the plane and the magnetic field is perpendicular. These two polarisations usually correspond to different topologies of 2D PhCs, as depicted in Fig. 2.8; high index rods surrounded by low index (a) and low-index holes in high index (b).

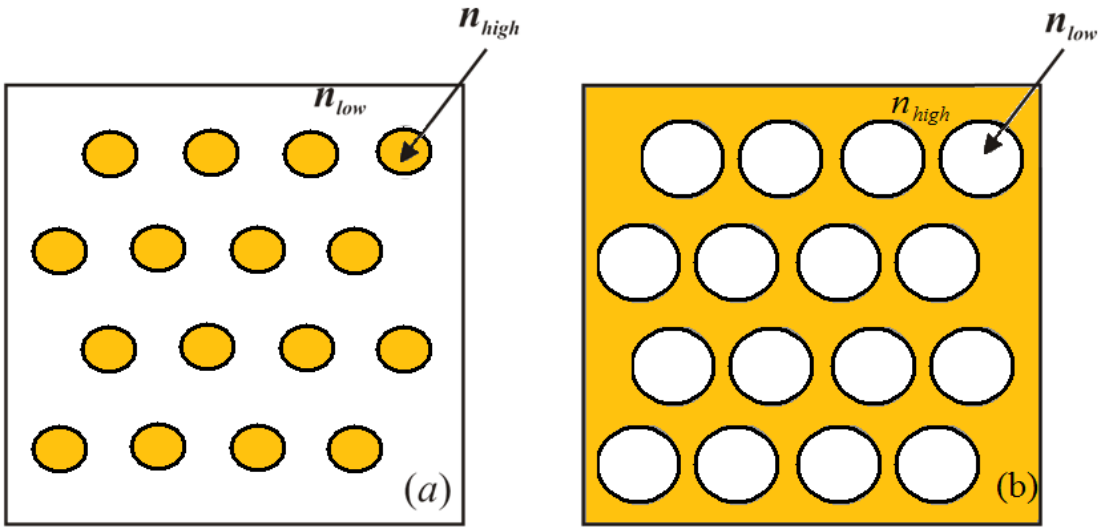

Figure 2.8 Topology of 2D PhCs: (a) Pillars of high index, n_{high}, in low index material, n_{low}. (b) Holes of low index, n_{low}, placed in high index, n_{high} material.

In Fig. 2.8, a hexagonal lattice is used, there are many advantages of having such lattices; they enjoy the highest symmetry in comparison with other lattices, such as square lattices, and the Brillouin zone is a hexagon, with almost a circular shape. As a result of the circular shape, the crystal shows a high degree of isotropy. The higher isotropy means that they show better appearance of omnidirectional bandgaps. This means that the lattice provides the largest bandgaps. That is because a photonic bandgap requires that the electric field lines run along thin veins, thus, the rods are best suited to TM light where the electric field are parallel to the rods, while the holes are best suited to TE light where the electric field runs around the holes. This can also be seen clearly in the band diagrams, shown in figures 2.9 and 2.10, where the rods, Fig. 2.9, and holes, Fig. 2.10, have a strong TM and TE bandgap, respectively.

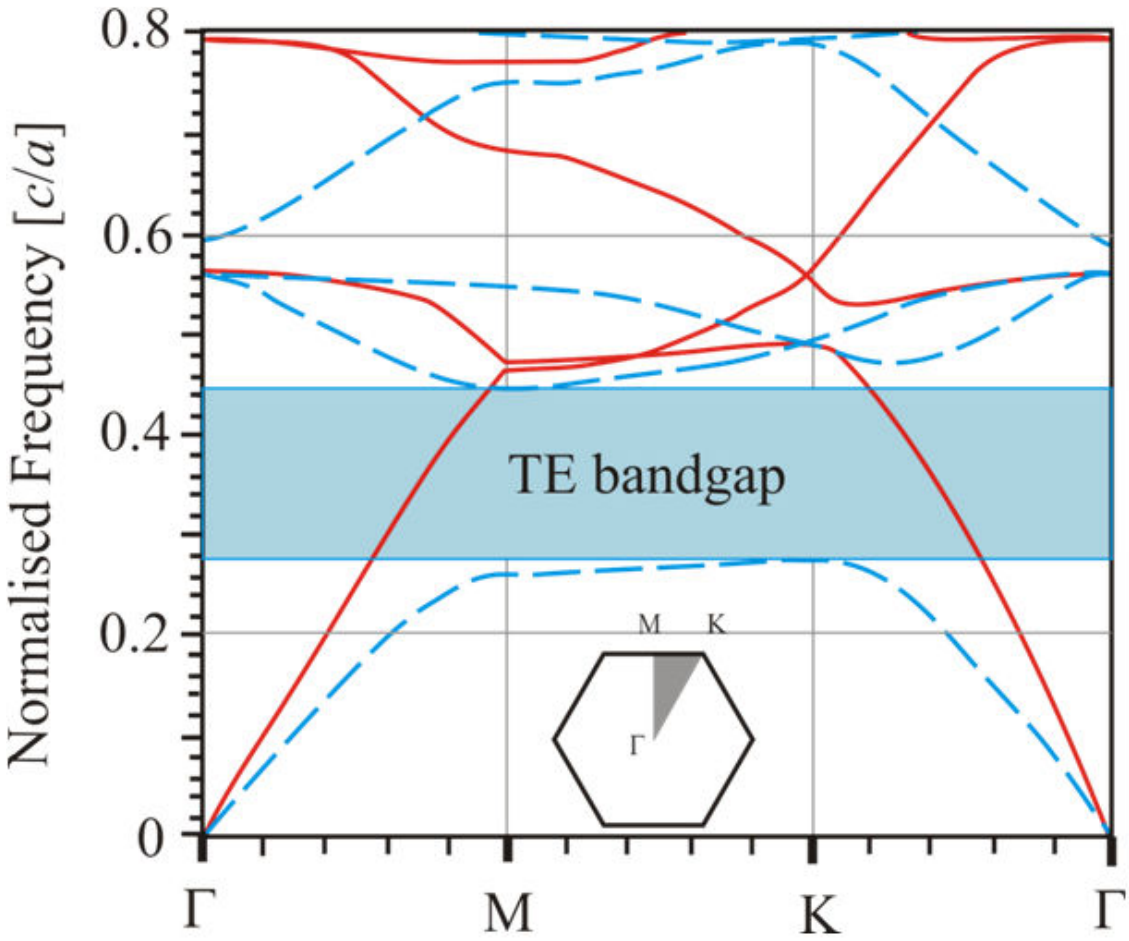

Figure 2.9 Bandgap diagram of a hexagonal lattice of high dielectric rods (n_{high} = 3.46, r = 0.2a) in air. TE modes are the blue dashed lines and the TM modes are the red solid lines. It is clear that dielectric rods produce a gap for TE polarisation.

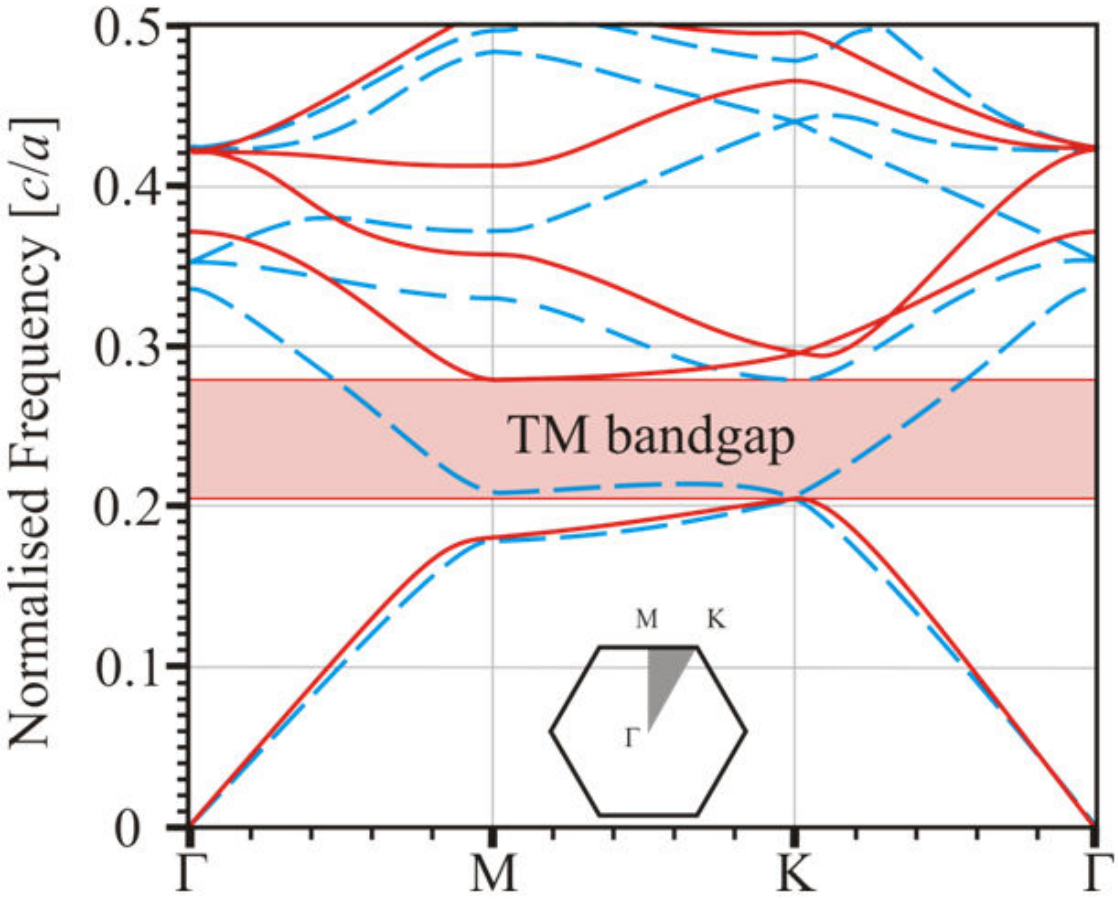

Figure 2.10 Bandgap diagram of a hexagonal lattice of air holes in high dielectric (n_{high} = 3.46, r = 0.3a). TE modes are the blue dashed lines and the TM modes are the red solid lines. It is clear that holes in dielectric produces a gap for TM polarisation.

The frequencies, ω, are conventionally represented in units of $2\pi c/a$, which correspond to a/λ where λ is the wavelength in vacuum. Conveniently, Maxwell's equations are scale-invariant, that is, they are characterised by the discrete translational symmetry that means their solutions are invariant under translations of distances that are multiples of a constant (the lattice constant a), [15]. A simple example, for a central

bandgap frequency with normalised units at 0.36, to have it correspond to λ = 1.55 μm, one would use $a = 0.36 \cdot 1.55\mu m = 0.56\mu m$.

The Brillouin zone (a hexagon) is displayed in the inset of figures 2.9 and 2.10 with the irreducible zone shaded in grey. The vertices of this zone signify specific directions: Γ corresponds to k = 0, K represents the direction of the minimum distance with the adjacent cell, and M is the next one among these minimum distances. So, M-Γ and K-Γ are the directions in which the source can be injected and the whole bandgap can be studied. The Brillouin zone is a 2D section of wavevectors, so the bands $\omega_n(k)$ are in fact surfaces, however, in practice the outermost band usually occur along the boundaries of the irreducible zone (i.e. the high-symmetry directions). Therefore, it is conventional to plot the bands along the zone boundaries in order to identify the bandgap, as done in Fig. 2.10 [15].

For certain topologies, holes in dielectric material, a complete photonic bandgap can be created that holds for both the polarisations, TE and TM. This can occur if the holes are large enough, almost touching. This causes the narrow veins between the holes to create a bandgap for the TM polarisation, while the intervals existing between groups of three holes realise a structure very similar to the one with pillars in air, thus a bandgap for TE can be created that overlaps the TM modes in frequency.

2.6 Photonic Crystal Slab

Two dimensional photonic crystals of finite length are the simplest way to realise three dimensional photonic crystals, this is known as photonic crystal slabs as it is shown in Fig. 2.11.

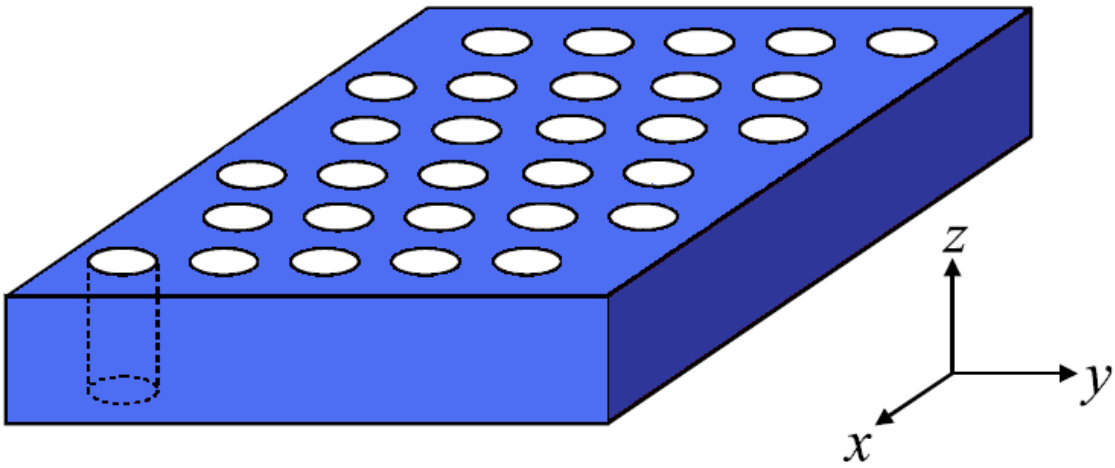

Fig. 2.11 Two dimensional photonic crystal of finite thickness and air holes in a dielectric slab.

The photonic crystal slab structure in Fig. 2.11 confines light inside it along the vertical direction through the index guiding effect, which generalises the total internal reflection technique. In such a structure, the 2D periodicity means that the two-dimensional Bloch wavevector $\vec{k}_{//}$ is a conserved quantity. This means that the projected band diagram of the all states in the bulk substrate/superstrate versus their in-plane wavevector components produces the map of what states can radiate vertically. A simple example is having the slab surrounded by air, which leads to the eigensolutions

$$\omega = c \cdot \sqrt{\left|\vec{k}_{//}\right|^2 + k^2{}_{\perp}} \tag{2.18}$$

when plotted in a diagram versus $\vec{k}_{//}$, as shown in Fig. 2.12, forms the continuous light cone $\omega \geq c \cdot \left|\vec{k}_{//}\right|$, shaded in grey in Fig. 2.12.

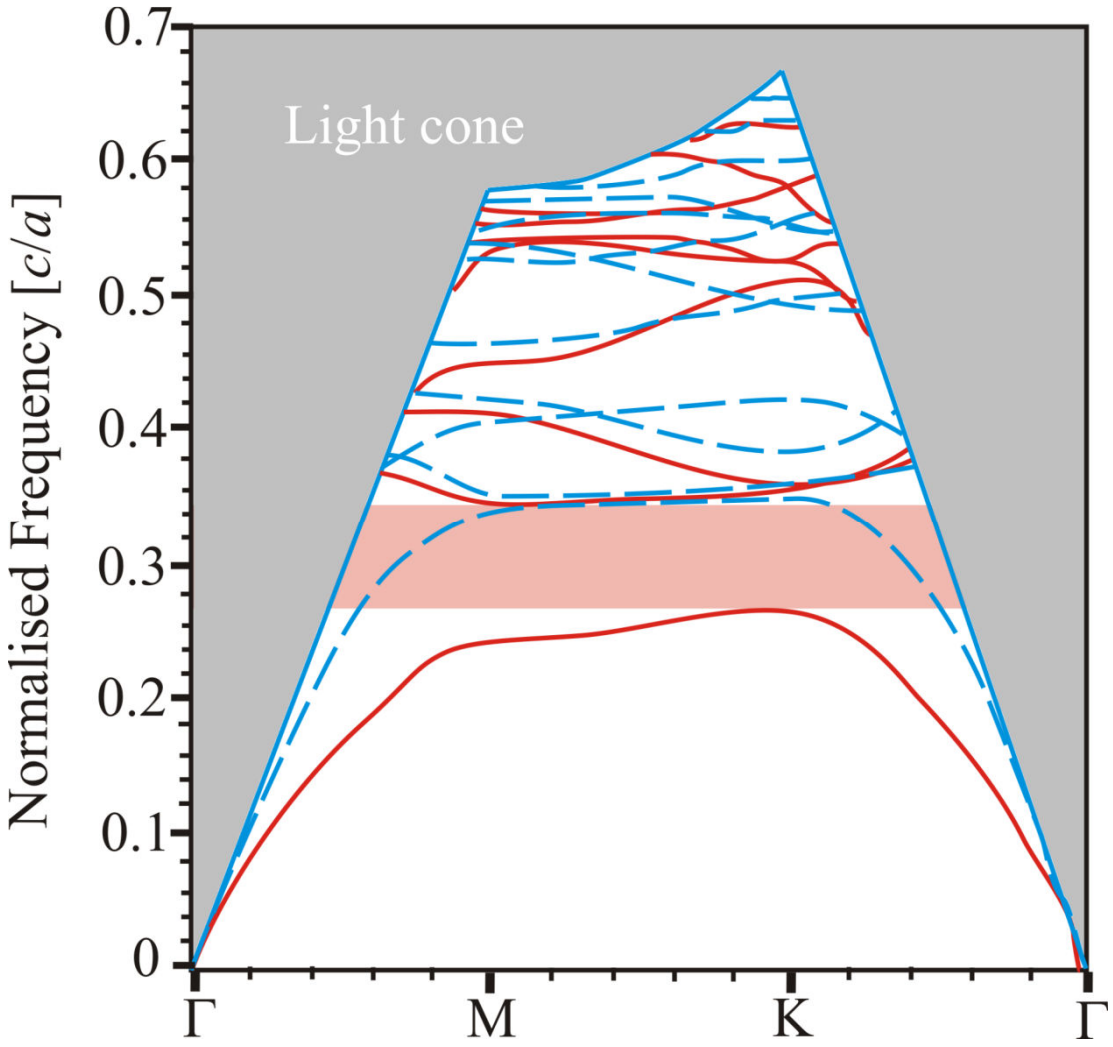

Figure 2.12 Band diagram of finite thickness (0.5 *a*) where PhC slab is made of air holes in dielectric. The light cone, in grey, corresponds to all the states that can radiate vertically in air. Whereas, the dashed blue lines, and solid red lines correspond to the guided modes trapped inside the PhC slab by the guided modes. These guided modes have TE- and TM-like polarisations, respectively. A bandgap for the TM-like guided modes occurs only.

The bands under the shaded region are guided, that is, they are confined to the PhC slab and do not couple to any of the vertical radiating modes. The solid red lines in

Fig. 2.12 clearly indicate to the sole existence of a bandgap for TM-like modes only. In spite of this, the bandgap is not complete as frequencies in the light cone radiate modes at each value of ω. This is the reason behind the strong vertical radiation losses that occur when the translational symmetry is completely broken, by inserting a resonant cavity or a bend in a waveguide or a resonant cavity. Nevertheless, lossless guiding can be realised if the defect affects one direction only, e.g. line defect waveguide.

For such photonic crystal slabs, the bandgap critically depends on their thickness; if the slab is too thin, the guided modes are weakly guided. However, if the slab is too thick, the higher-order modes appear inside the bandgap. The optimum slab thickness is around half a wavelength, in Fig. 2.12 the thickness used is 0.5 a.

2.7 Photonic Crystal Defects

2.7.1 Introduction

Some of the most interesting phenomena occur when the crystal is broken by introducing defects. A defect is anything that interrupts the normal periodicity of the crystal, causing a localised state to resonate inside the bandgap, which by definition no frequency can propagate freely inside it.

Most typically, defects can be classified into one of two classes: point defects, which create resonant cavities, and line defects, which create waveguides. Both defects can be illustrated as in Fig. 2.13. The key point is that a defect has the capability of supporting modes that are within the bandgap range of the crystal, and that these modes are localised within the defect. Generally there are two ways to create states in the gap: either pulling a localised state down from the upper band by increasing the dielectric

constant or to push a localised state up from the lower band by decreasing the dielectric constant.

A point defect is simply a defect of finite extent in all directions, and supports a resonant cavity mode, or modes, with a discrete sequence of frequencies. A line defect is a defect that extends periodically with infinite extent in one axial direction and with finite extent in the lateral directions. Because of the periodicity in one-dimension, a line defect forms a waveguide, and introduces a guided mode band that has a one-dimension Bloch wavevector and which is localised in the lateral directions [19].

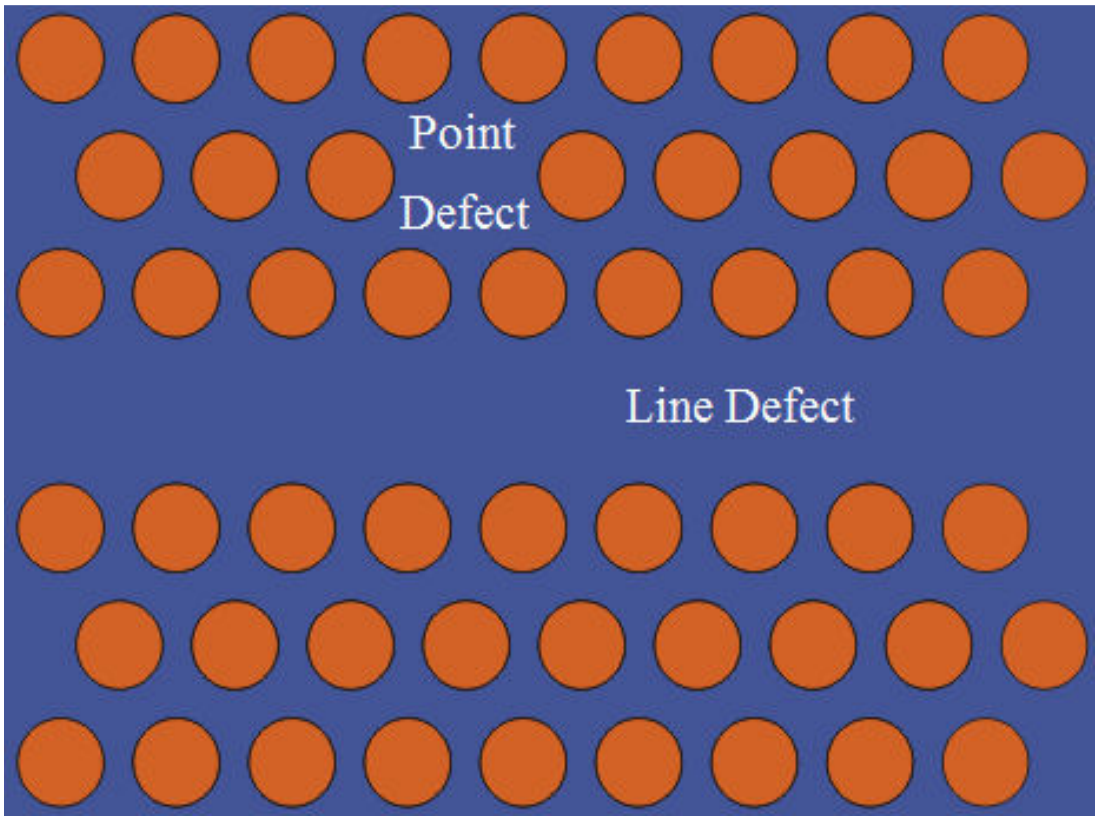

Figure 2.13 Schematic diagram of a 2D PhC structure with a point defect and line defect.

Such defects can be created by changing the radius or the dielectric constant of a hole/rod, thereby disturbing the periodicity of the structure and breaking the

translational symmetry of the lattice. This phenomenon enables localised modes to occur at certain frequencies within the gap.

2.7.2 Localised modes, defects, and breaking the periodicity

Once the translational symmetry of a photonic crystal structure is broken, by the presence of a defect, the modes cease to be categorised by an in-plane wavevector. This means that states, with frequencies in the range of the bandgap, may localise within the defect. Such localised states decay exponentially as they leave the defect and are known as evanescent states. Nevertheless, there may exist certain frequencies in which, even though the periodicity of a lattice is disrupted by the presence of a defect, it remains possible for such frequencies to support extended states inside the entire crystal [14 - 15], and [18]. Such frequencies can be determined through observing the band diagram of the crystal. Fig 2.14 illustrates both extended and evanescent states, the latter can be described by

$$H_k(x) = \left[e^{jkx} f_k(x)\right] e^{-kx} \tag{2.19}$$

where the decay factor can be approximated by

$$\omega(k) = \omega_0 + \alpha(k - k_0)^2 \tag{2.20}$$

where α is a positive number, k is considered to be limited to 1D, and frequencies near ω_0 are described by

$$k = k_0 \pm j\sqrt{\frac{\Delta\omega}{\alpha}} \tag{2.21}$$

where the imaginary component describes the exponential decay.

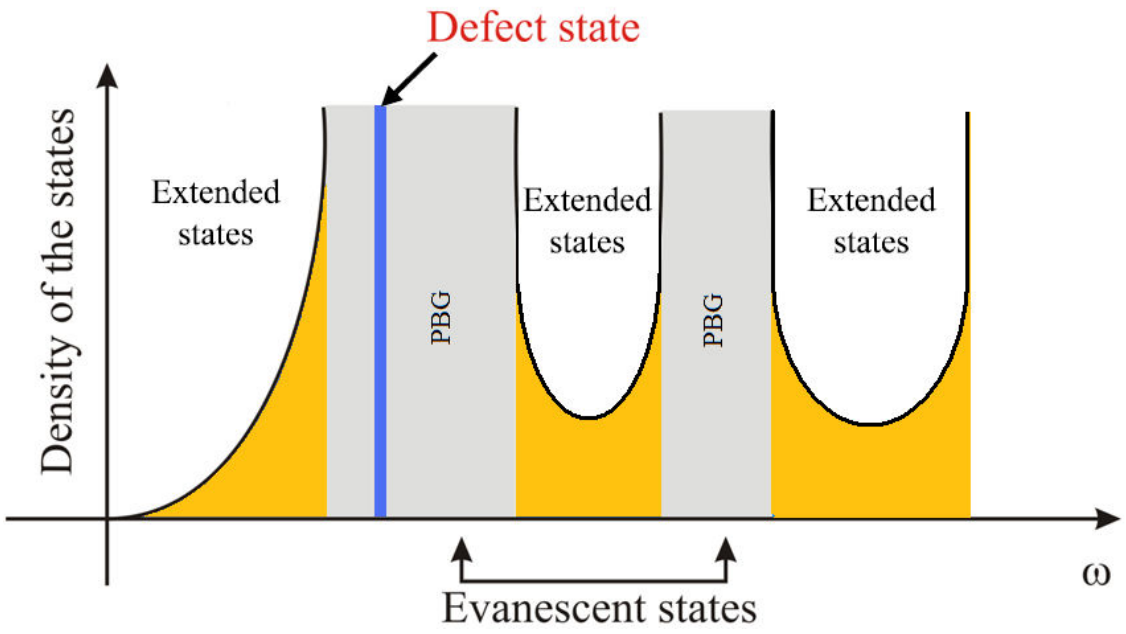

Figure 2.14 Frequency range divided into extended states, in yellow, and evanescent states, in grey. The blue line represents a localised mode that can exist within the bandgap region, where only evanescent modes are allowed, by a defect

The perturbation of the dielectric constant and the geometry of the defect are what determine the states that can be introduced in the forbidden gap. Increasing the refractive index of the defect or decreasing its size causes modes to be pushed up from the lower band into the gap. Similarly, decreasing the refractive index of the defect or increasing its size causes the modes to be pulled down from the upper band into the gap. This effectively causes states to localise at higher or lower frequencies, respectively. It should be noted here that the most eligible frequency to be confined with the defect is always the one at the centre of the bandgap, which is the strongest to be confined within the defect.

2.7.3 Point defects: cavities

As illustrated in Fig. 2.13, a microcavity, otherwise known as a point defect, can be introduced into a photonic crystal structure by removing a hole/rod from the periodic structure. This causes the microcavity to harness the light within it, creating a resonant mode, as displayed in Fig. 2.15, where the light is confined in the cavity and the mode resonates.

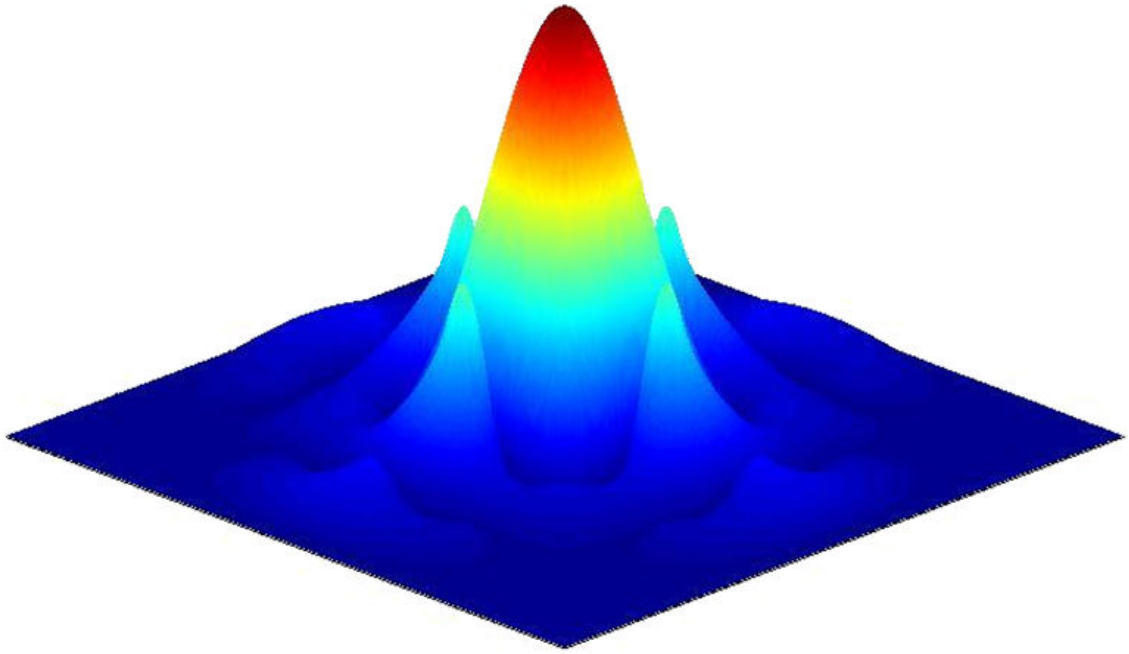

Figure 2.15 Field profile of a resonant mode in a point defect

Not only have such microcavities, in two dimensional photonic crystal structures, opened the doors to creating high quality devices at telecommunication frequencies, they have also prove to be suitable for implementing on the microchip, specifically with semiconductor materials of III-V group, e.g. Gallium Arsenide (GaAs), [20], and [21]. One of the key properties of cavities in a photonic crystal is the ability to tune a cavity to resonate at specific frequency within the bandgap and change the mode

symmetry by carefully modifying the defect [20], and [21]. Fig. 2.16 illustrates the four main types of point defect in a 2D PhC structure; this includes a point defect that is created by introducing a larger or smaller hole/rod into the otherwise periodic lattice, or by completely removing a hole/rod, or even introducing a hole/rod with a different dielectric constant than that used to construct the lattice.

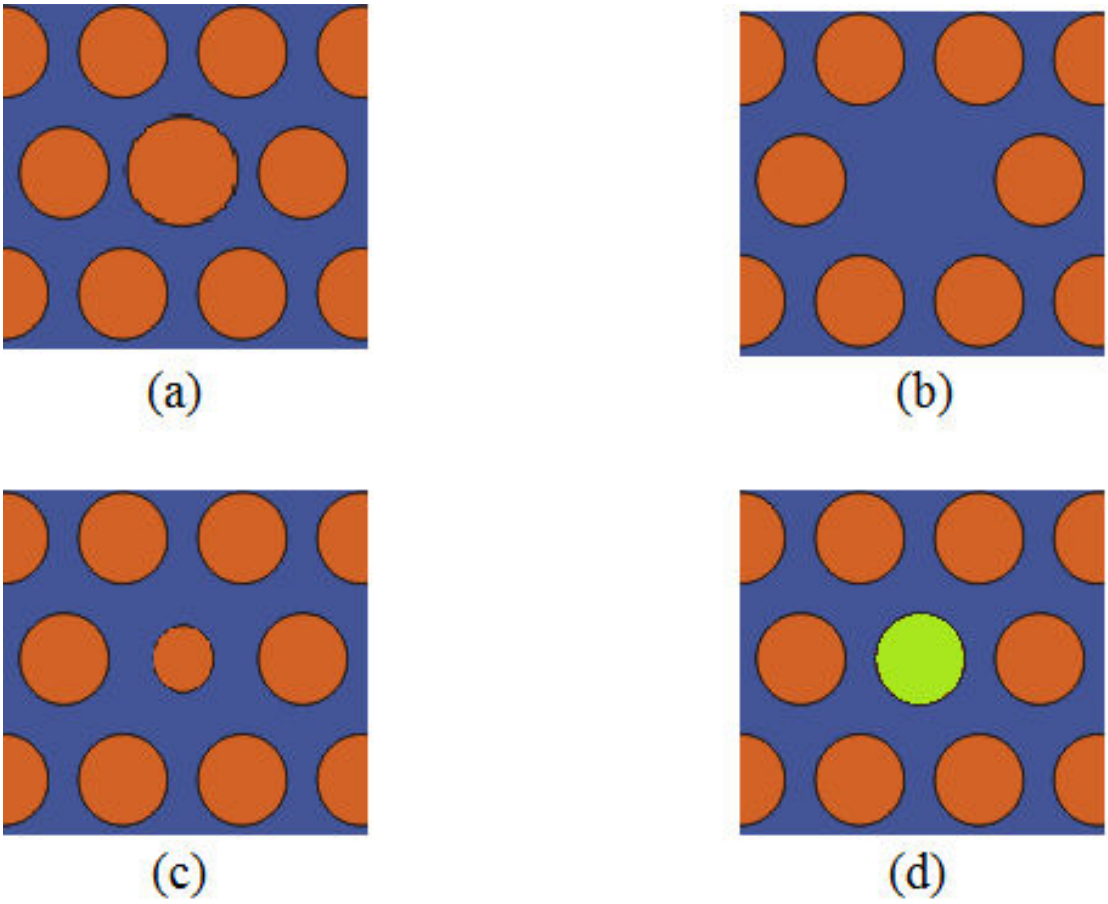

Figure 2.16 Schematics of 2D PhC structures with point defects, hole/rod: (a) defect where $r_{defect} > r$, where r is the radius of the hole/rod, (b) hole/rod removed, (c) defect where $r_{defect} < r$, (d) defect, hole/rod has different dielectric constant.

The effectiveness of a cavity is based on its characteristics, which are defined by two major parameter; quality factor Q, and the β factor. The β_m factor, where m is the

mode, corresponds to the amount of spontaneous emission in comparison to the other modes resonating in the cavity. The former, Q factor, can be described by

$$Q = \frac{\omega}{\gamma} \tag{2.22}$$

where ω is the mode frequency and γ is the number of photons lost by the mode per second [14].

2.7.4 Line defects: waveguides

As illustrated in Fig. 2.14, a line defect can be introduced into a photonic crystal structure by modifying a line of holes/rods the periodic structure. These photonic crystal waveguides managed to overcome the major issue of bends in waveguides, which proved to be the weak point of other waveguide techniques such as total internal reflection.

Total internal reflection depends on the high contrast between core and cladding indices to guide the beam, which suffers from high losses when the radius of the bend is comparable to the wavelength. Whereas, photonic crystal waveguides overcome this limit as they guide light in a different manner, this is important in integrated optical circuits [22 - 25]. The line defect inserted into the photonic crystal structure allows certain modes to resonate within the forbidden gap. These modes propagate within and along the direction of the defect without escaping into the periodic lattice, as illustrated in Fig. 2.17, where the lightwave propagates along the waveguide.

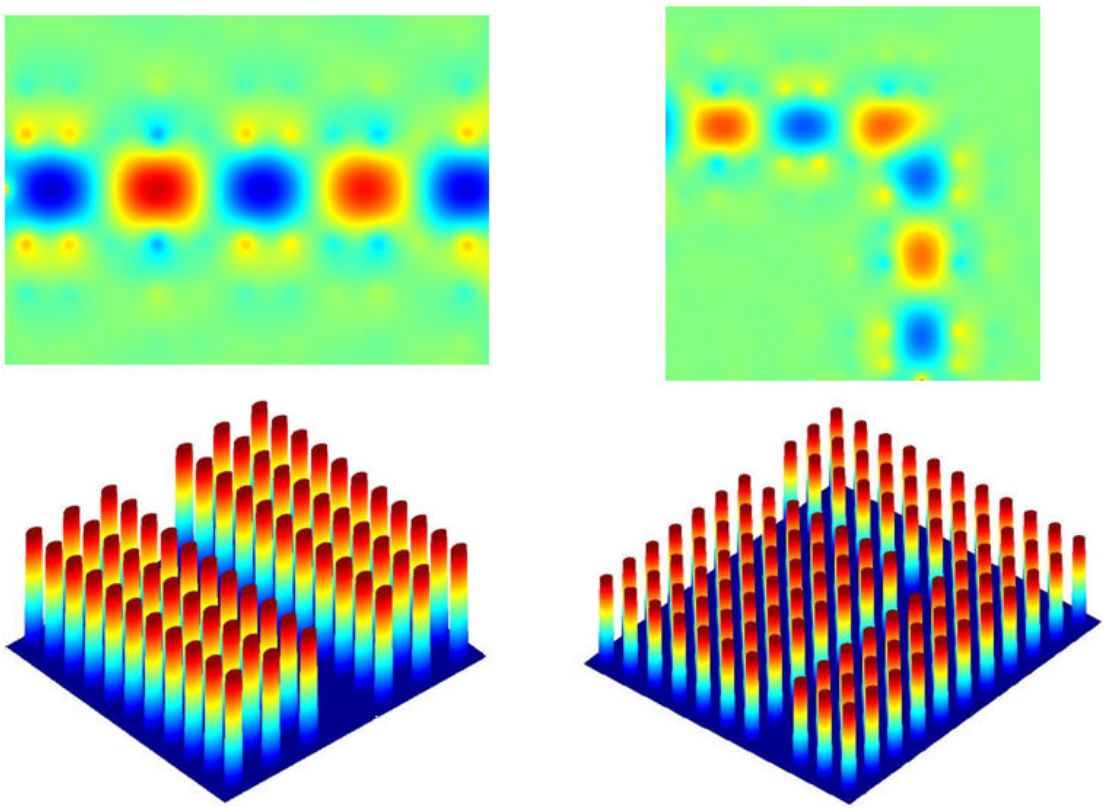

Fig. 2.17 Field profile of the propagating mode along a line defect

Line defects in photonic crystals are highly efficient in their transmission, up to almost 100% transmission for bends of 90 degrees [15], and [26]. Hence, photonic crystal waveguides alongside microcavities have become the building block of various optical devices, take for example, channel drop filters [27 - 28], and multiplexers/demultiplexers [29 - 30].

2.8 Summary

This chapter has covered the essential background theory of photonic crystals. This included highlighting their capability to manipulate the flow of light. The origin of the PBG was explained starting from Maxwell's equations, and then the 1D, 2D, and

slab PhCs were presented. The phenomena of capturing and controlling the flow of light through creating defects in the PhC structure were covered.

In order to successfully model and simulate these PhC structures the CE-ADI-FDTD numerical modelling method was used. This technique is presented in detail in chapter 3.

Chapter 3

Complex Envelope - Alternating Direction Implicit - Finite Difference Time Domain

3.1 Introduction

Since 2D PhCs have complicated structures and cannot be analysed using simple techniques, several numerical methods have been developed for such complicated electromagnetic structures. Therefore, this chapter aims at reviewing the techniques and methods behind the numerical analysis and modelling of Maxwell's partial differential

equations of electromagnetic systems, with a detailed emphasis on the method of interest, CE-ADI-FDTD.

3.2 Background

There are two main computational techniques by which Maxwell's equations in an electromagnetic system can be analysed; frequency-domain, and time-domain. The frequency-domain includes methods such as beam propagation, and finite element frequency domain methods. These techniques have showed significant progress [31], however even the most advanced frequency-domain techniques are exhausted by numerous volumetrically complex structures of interest. On the other hand, time-domain methods such as; finite element time-domain, multi-resolution time-domain, and finite difference time-domain [32], hold many advantages over their frequency-domain equivalent. One of the main advantages is that one simulation of a PhC in time-domain results in a big range of frequencies to study. Hence, this research is mainly concerned with the time-domain computational techniques and in particular the FDTD. This method is one of the most widely used numerical methods for the computation of the electromagnetic propagation.

The FDTD algorithm is used, as a computer code is developed and enhanced to analyse the propagation characteristics of PhC structures. The following section gives a detailed review of the FDTD. After that, a more sophisticated method that branches out from the FDTD will be presented, this is known as the CE-ADI-FDTD method [33].

3.3 Finite Difference Time Domain

3.3.1 Yee lattice

The FDTD method was introduced by Yee in 1966 [34] in which the basis of the FDTD technique for solving Maxwell's equations in the time-domain on a space grid was described. Steps in time are taken at regular intervals, where the time variation of the field components is calculated at each cell based on the discretised equations derived from Maxwell's equations for electromagnetic propagation theory, as expressed below

$$\frac{\partial E_x}{\partial t} = \frac{1}{\varepsilon}\left(\frac{\partial H_z}{\partial y} - \frac{\partial H_y}{\partial z} - \sigma E_x\right) \tag{3.1}$$

$$\frac{\partial E_y}{\partial t} = \frac{1}{\varepsilon}\left(\frac{\partial H_x}{\partial z} - \frac{\partial H_z}{\partial x} - \sigma E_y\right) \tag{3.2}$$

$$\frac{\partial E_z}{\partial t} = \frac{1}{\varepsilon}\left(\frac{\partial H_y}{\partial x} - \frac{\partial H_x}{\partial y} - \sigma E_z\right) \tag{3.3}$$

$$\frac{\partial H_x}{\partial t} = \frac{1}{\mu}\left(\frac{\partial E_y}{\partial z} - \frac{\partial E_z}{\partial y} - \sigma^* H_x\right) \tag{3.4}$$

$$\frac{\partial H_y}{\partial t} = \frac{1}{\mu}\left(\frac{\partial E_z}{\partial x} - \frac{\partial E_x}{\partial z} - \sigma^* H_y\right) \tag{3.5}$$

$$\frac{\partial H_z}{\partial t} = \frac{1}{\mu}\left(\frac{\partial E_x}{\partial y} - \frac{\partial E_y}{\partial x} - \sigma^* H_z\right) \tag{3.6}$$

The method progresses cell by cell and step by step, such that, each iteration is completed in both time and space for new values based on the field distribution calculated in the previous step. The iterations are applied until the simulation reaches steady state condition. This results in a set of findings that represent the field development inside the investigated structure obtained in time domain.

The FDTD method sets up the medium on a cubic grid cell with Cartesian coordinates as shown in Fig. 3.1. This simple, yet effective and robust technique has the FDTD lattice set up such that each electric field component is evaluated at the edges of the Yee lattice, and surrounded by four magnetic field components that are evaluated at the centre of the sides of the Yee lattice [32], and [34]. The electric field and magnetic field components are arranged in space in so that every *E* component is surrounded by four circulating *H* components and every *H* component is surrounded by four *E* components in the same way.

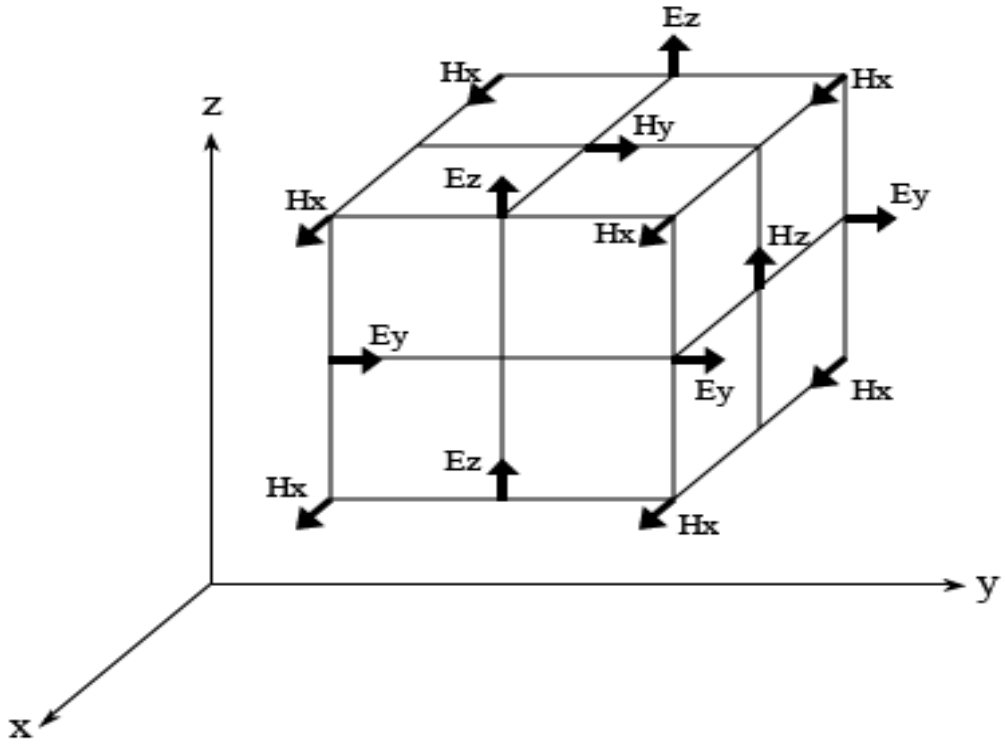

Figure 3.1 Yee Lattice [33]

In Fig. 3.1 the discretisation in space is performed on the Yee cell. This technique applies a finite-difference grid on a simulated electromagnetic field that

propagates inside a continuous space. The fields are sampled at discrete locations on each cell of this finite-difference grid.

3.3.2 Leapfrog

The leapfrog, illustrated in Fig. 3.2, defines how the adjacent field components are related to one another in order to generate other field components as time is marching on.

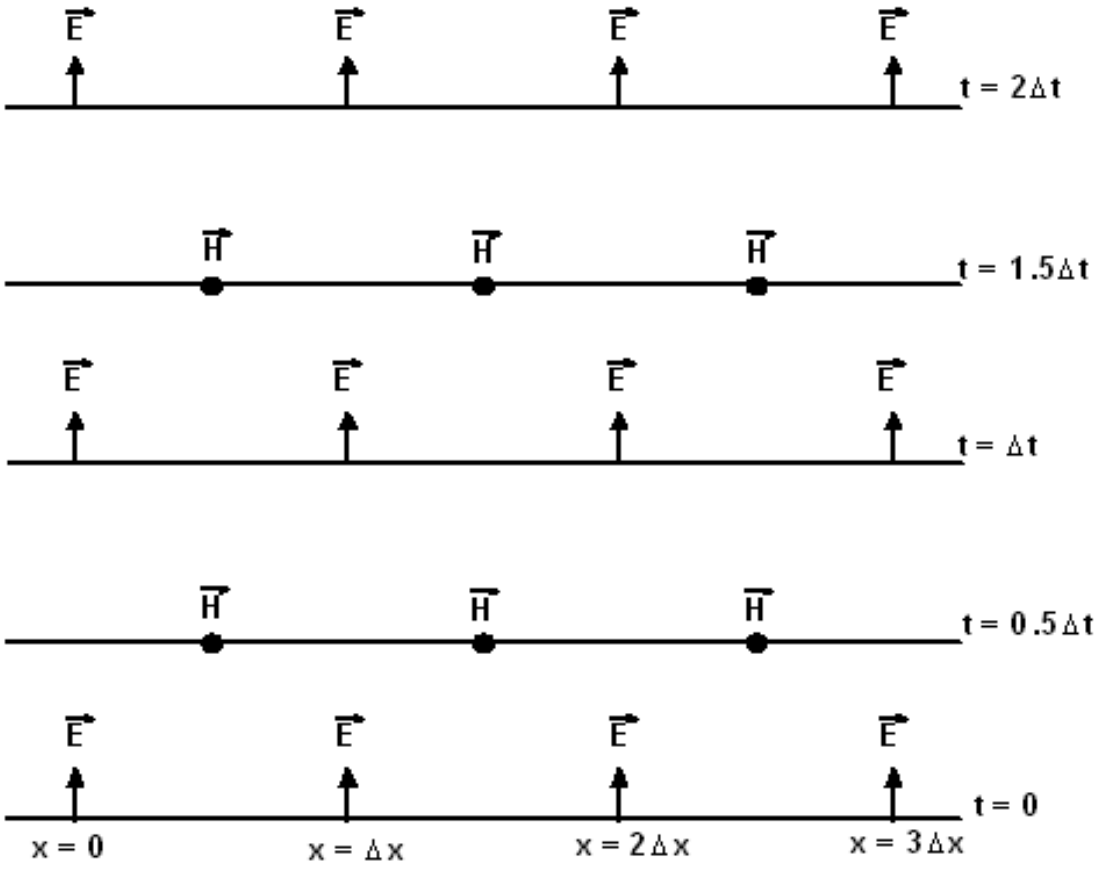

Figure 3.2 Leapfrog as time is marching [32]

In Fig. 3.2 the discretisation in time is obtained following the leapfrog arrangement where components are arranged in time such that all the *E* components at a particular point in time are calculated by using the *H* values computed from the previous

step, and all the new H components are similarly calculated by using the E values computed, and so on, until time-stepping is concluded at the end of the simulation. The geometry of the Yee lattice is set such that it has a dimension of Δx, Δy, and Δz of the grid size. Δt denotes the time step from one lattice point to the next lattice point.

There are several advantages of using the Yee algorithm as opposed to other methods; it solves for both electric and magnetic fields in time and space using the coupled Maxwell's curl equations, rather than the electric field alone as is the case when using the wave equation. This leads to an explicit scheme that is relatively easy to implement. As seen in Fig. 3.1, the Yee lattice sets up the grid such that there is an interlinked array of Faraday's law and Ampere's law contours. As illustrated in Fig. 3.2, Yee's lattice centres the electric and magnetic components in time in a fully explicit leapfrog time-stepping manner, hence avoiding the need to solve equations simultaneously or use matrix inversions.

3.3.3 Finite-difference notation of Maxwell's equations

The finite-difference-time-domain expressions for Maxwell's equations in 3-Dimensions (3D) are as follows [32]:

$$H_x\big|_{i-1/2,j+1,k+1}^{n+1} = \left(\frac{1-\dfrac{\sigma^*\big|_{i-1/2,j+1,k+1}\,\Delta t}{2\mu_0\mu_r\big|_{i-1/2,j+1,k+1}}}{1+\dfrac{\sigma^*\big|_{i-1/2,j+1,k+1}\,\Delta t}{2\mu_0\mu_r\big|_{i-1/2,j+1,k+1}}}\right) H_x\big|_{i-1/2,j+1,k+1}^{n} - \left(\frac{\dfrac{\Delta t}{\mu_0\mu_r\big|_{i-1/2,j+1,k+1}}}{1+\dfrac{\sigma^*\big|_{i-1/2,j+1,k+1}\,\Delta t}{2\mu_0\mu_r\big|_{i-1/2,j+1,k+1}}}\right) \tag{3.7}$$
$$\left(\frac{E_z\big|_{i-1/2,j+3/2,k+1}^{n+1/2} - E_z\big|_{i-1/2,j+1/2,k+1}^{n+1/2}}{\Delta y} - \frac{E_y\big|_{i-1/2,j+1,k+3/2}^{n+1/2} - E_y\big|_{i-1/2,j+1,k+1/2}^{n+1/2}}{\Delta z}\right)$$

$$H_y\,|^{n+1}_{i,j+1/2,k+1} = \left(\frac{1-\frac{\sigma^*\,|_{i,j+1/2,k+1}\,\Delta t}{2\mu_0\mu_r\,|_{i,j+1/2,k+1}}}{1+\frac{\sigma^*\,|_{i,j+1/2,k+1}\,\Delta t}{2\mu_0\mu_r\,|_{i,j+1/2,k+1}}}\right) H_y\,|^{n}_{i,j+1/2,k+1} - \left(\frac{\frac{\Delta t}{\mu_0\mu_r\,|_{i,j+1/2,k+1}}}{1+\frac{\sigma^*\,|_{i,j+1/2,k+1}\,\Delta t}{2\mu_0\mu_r\,|_{i,j+1/2,k+1}}}\right) \left(\frac{E_x\,|^{n+1/2}_{i,j+1/2,k+3/2} - E_x\,|^{n+1/2}_{i,j+1/2,k+1/2}}{\Delta z} - \frac{E_z\,|^{n+1/2}_{i+1/2,j+1/2,k+1} - E_z\,|^{n+1/2}_{i-1/2,j+1/2,k+1}}{\Delta x}\right) \tag{3.8}$$

$$H_z\,|^{n+1}_{i,j+1,k+1/2} = \left(\frac{1-\frac{\sigma^*\,|_{i,j+1,k+1/2}\,\Delta t}{2\mu_0\mu_r\,|_{i,j+1,k+1/2}}}{1+\frac{\sigma^*\,|_{i,j+1,k+1/2}\,\Delta t}{2\mu_0\mu_r\,|_{i,j+1,k+1/2}}}\right) H_z\,|^{n}_{i,j+1,k+1/2} - \left(\frac{\frac{\Delta t}{\mu_0\mu_r\,|_{i,j+1,k+1/2}}}{1+\frac{\sigma^*\,|_{i,j+1,k+1/2}\,\Delta t}{2\mu_0\mu_r\,|_{i,j+1,k+1/2}}}\right) \left(\frac{E_y\,|^{n+1/2}_{i+1/2,j+1,k+1/2} - E_y\,|^{n+1/2}_{i-1/2,j+1,k+1/2}}{\Delta x} - \frac{E_x\,|^{n+1/2}_{i,j+3/2,k+1/2} - E_x\,|^{n+1/2}_{i,j+1/2,k+1/2}}{\Delta y}\right) \tag{3.9}$$

$$E_x\,|^{n+1/2}_{i,j+1/2,k+1/2} = \left(\frac{1-\frac{\sigma\,|_{i,j+1/2,k+1/2}\,\Delta t}{2\varepsilon_0\varepsilon_r\,|_{i,j+1/2,k+1/2}}}{1+\frac{\sigma\,|_{i,j+1/2,k+1/2}\,\Delta t}{2\varepsilon_0\varepsilon_r\,|_{i,j+1/2,k+1/2}}}\right) E_x\,|^{n-1/2}_{i,j+1/2,k+1/2} - \left(\frac{\frac{\Delta t}{\varepsilon_0\varepsilon_r\,|_{i,j+1/2,k+1/2}}}{1+\frac{\sigma\,|_{i,j+1/2,k+1/2}\,\Delta t}{2\mu_0\mu_r\,|_{i,j+1/2,k+1/2}}}\right) \left(\frac{H_z\,|^{n}_{i,j+1,k+1/2} - H_z\,|^{n}_{i,j,k+1/2}}{\Delta y} - \frac{H_y\,|^{n}_{i,j+1/2,k+1} - H_y\,|^{n}_{i,j+1/2,k}}{\Delta z}\right) \tag{3.10}$$

$$E_y\,|^{n+1/2}_{i-1/2,j+1,k+1/2} = \left(\frac{1-\frac{\sigma\,|_{i-1/2,j+1,k+1/2}\,\Delta t}{2\varepsilon_0\varepsilon_r\,|_{i-1/2,j+1,k+1/2}}}{1+\frac{\sigma\,|_{i-1/2,j+1,k+1/2}\,\Delta t}{2\varepsilon_0\varepsilon_r\,|_{i-1/2,j+1,k+1/2}}}\right) E_y\,|^{n-1/2}_{i-1/2,j+1,k+1/2} - \left(\frac{\frac{\Delta t}{\varepsilon_0\varepsilon_r\,|_{i-1/2,j+1,k+1/2}}}{1+\frac{\sigma\,|_{i-1/2,j+1,k+1/2}\,\Delta t}{2\varepsilon_0\varepsilon_r\,|_{i-1/2,j+1,k+1/2}}}\right) \left(\frac{H_x\,|^{n}_{i-1/2,j+1,k+1} - H_x\,|^{n}_{i-1/2,j+1,k}}{\Delta z} - \frac{H_z\,|^{n}_{i,j+1,k+1/2} - H_z\,|^{n}_{i-1,j+1,k+1/2}}{\Delta x}\right) \tag{3.11}$$

$$E_z\,|_{i-1/2,j+1/2,k+1}^{n+1/2} = \left(\frac{1-\dfrac{\sigma\,|_{i-1/2,j+1/2,k+1}\,\Delta t}{2\varepsilon_0\varepsilon_r\,|_{i-1/2,j+1/2,k+1}}}{1+\dfrac{\sigma\,|_{i-1/2,j+1/2,k+1}\,\Delta t}{2\varepsilon_0\varepsilon_r\,|_{i-1/2,j+1/2,k+1}}}\right) E_z\,|_{i-1/2,j+1/2,k+1}^{n-1/2} - \left(\frac{\dfrac{\Delta t}{\varepsilon_0\varepsilon_r\,|_{i-1/2,j+1/2,k+1}}}{1+\dfrac{\sigma\,|_{i-1/2,j+1/2,k+1}\,\Delta t}{2\varepsilon_0\varepsilon_r\,|_{i-1/2,j+1/2,k+1}}}\right) \quad (3.12)$$
$$\left(\frac{H_y\,|_{i,j+1/2,k+1}^{n} - H_y\,|_{i,j+1/2,k+1}^{n}}{\Delta x} - \frac{H_x\,|_{i-1/2,j+1,k+1}^{n} - H_x\,|_{i-1/2,j,k+1}^{n}}{\Delta y}\right)$$

In the above equations (3.7 - 3.12), the symbols used are defined as follows:

E: electric field

H: magnetic field

ε_r: relative permittivity

μ_r: relative permeability

μ_o: free-space permeability

σ: electric conductivity

σ^*: equivalent magnetic loss

It should be noted here that equations (2.1 - 2.4) are Maxwell's Equations, in differential form, while the above equations (3.7 - 3.12) are the FDTD equations in discretised form.

3.3.4 Numerical dispersion and stability

The main concerns over the FDTD method are the constraints upon its space and time discretisation parameters. The constraints upon the space discretisation are set in place to overcome the unavoidable side effect of the nature of every numerical method that is based on a discretised mesh, in this case the FDTD. This is because the numerical medium in which the fields interact is an artificial medium with properties very close to, but not exactly the same as, those in vacuum. In other words, applying the FDTD algorithms on Maxwell's equations can cause nonphysical dispersion of the simulated

waves in a free-space computational lattice [35]. This means that the phase velocity of numerical wave modes can differ from the speed of light. This variation depends on the wavelength of the propagating wave, the direction of propagation in the grid, and the grid discretisation [35].

As for the constraints set upon the time discretisation, they are put in place so as to avoid numerical instability that can cause the computed results to increase without limit as time-marching continues. Thus, the FDTD algorithms for Maxwell's equations require that the time-step Δt has a specific bound relative to the lattice space increments Δx, Δy, and Δz [35].

This section focuses on laying out the method used in this work to avoid numerical instability and minimise the unavoidable numerical dispersion.

3.3.4.1 Numerical dispersion

Numerical dispersion has to be taken into account in order to avoid delays or phase errors propagating into the structure that may lead to non-physical results. This can be achieved by choosing proper dimensions for the cell grid. To analyse numerical dispersion in FDTD, the numerical dispersion equation for Yee's scheme in the three-dimensional case is considered. Then, it is compared to the ideal case which has grid resolution defined on the base of examples available in literature. Yee's algorithm brings to [35]

$$\left[\frac{1}{\Delta x}\sin\left(\frac{k_x\Delta x}{2}\right)\right]^2+\left[\frac{1}{\Delta y}\sin\left(\frac{k_y\Delta y}{2}\right)\right]^2+\left[\frac{1}{\Delta z}\sin\left(\frac{k_z\Delta z}{2}\right)\right]^2=\left[\frac{1}{c\cdot\Delta t}\sin\left(\frac{\omega\Delta t}{2}\right)\right]^2 \quad (3.13)$$

The dispersion relation for the ideal case of plane wave in lossless medium states

$$\frac{\omega^2}{c^2} = k_x^2 + k_y^2 + k_z^2 \tag{3.14}$$

Taking into account the following well known limit property

$$\lim_{x \to 0} \left(\frac{\sin x}{x} \right) = 1 \tag{3.15}$$

Comparing Eq. (3.13 - 3.14), for Δx, Δy, Δz, and Δt that simultaneously tend to zero, the two equations are found to be the same. This means that the increments in space and time need to be very small compared to the structure dimensions, in other words a very fine mesh helps in reducing the effects of numerical dispersion and thus ensures accuracy of the results. It can be noted that with a grid resolution of $\Delta = \lambda / 20$ the variation of the normalised phase velocity is reduced to 0.3% which can be considered as a lower bound in order to get accurate results [18].

3.3.4.2 Numerical stability

It has been shown in the above that careful selection of Δ and Δt can affect the wave propagation characteristics and substantially reduce numerical dispersion. Similarly, bounding Δt can ensure numerical stability. FDTD equations impose a specific limit on the choice of the time increment Δt that is related to the dimensions of the unit cell in the grid Δx, Δy, and Δz [35].

$$2\sqrt{\frac{1}{\Delta x^2} + \frac{1}{\Delta y^2} + \frac{1}{\Delta z^2}} \leq \frac{2}{\Delta t \cdot c} \tag{3.16}$$

From Eq (3.16), the criteria that bounds the choice of Δt is derived as

$$\Delta t \leq \frac{1}{c\sqrt{\frac{1}{(\Delta x)^2} + \frac{1}{(\Delta y)^2} + \frac{1}{(\Delta z)^2}}} \tag{3.17}$$

In the specific case of a cubic cell having $\Delta x = \Delta y = \Delta z = \Delta$, the criteria is written as

follows

$$\Delta t < \frac{1}{c\sqrt{\frac{1}{\Delta^2}+\frac{1}{\Delta^2}+\frac{1}{\Delta^2}}} = \frac{1}{c\sqrt{\frac{3}{\Delta^2}}} = \frac{\Delta}{c\sqrt{3}} \tag{3.18}$$

It can be easily seen that in the two-dimensional case, for a square cell, the relation becomes

$$\Delta t \leq \frac{\Delta}{c \cdot \sqrt{2}} \tag{3.19}$$

This means that as the space discretisation increases so does the Courant time limit, and thus sets an important constraint upon the stability of the method. The validity of Eq. (3.18) is adequate to warrant the stability of the numerical scheme for an indefinite numbers of time steps. However, the stability of the FDTD scheme is not only influenced by carefully applying Eq. (3.18). Other aspects can jeopardise the stability of the FDTD method, such as boundary conditions applied to the computational domain, the employment of non-uniform meshes for the discretisation of the computational domain, dispersive media, nonlinear media, and media with loss [18]. Nevertheless, having raised these concerns, an enormous amount of simulation results for these cases in literature has shown that the FDTD method can be successfully applied. The scheme shows numerical stability for at least the number of time steps necessary to extract all the essential information from the simulations, although not for an indefinite number of time steps [34].

In optical devices it is recommended in literature that $\Delta \approx \frac{\lambda}{15}$ [35]. This sets a tight constraint upon Δt, for example, in telecommunications, substituting $\lambda = 1.55\ \mu m$ into Eq. (3.19) where $\Delta \approx \frac{\lambda}{15}$ leads to $\Delta t \leq 0.243727\ fs$. This time constraint ensures the

numerical stability of the method, yet is very restrictive. In order to relax this constraint the alternating direction implicit technique is used.

3.4 Alternating Direction Implicit Finite Difference Time Domain

Although the FDTD method has the ability to simulate a wide range of devices for a large range of frequency, from microwave to optical, for certain problems, such as resonant cavities with very high quality factor Q and structures with geometrical features very small compared to the shortest wavelength involved, the requirement of computational resources of the FDTD method can be unreasonable, especially since the time step employed in FDTD simulation is bounded by Eq. (3.18).

The Alternating-Direction-Implicit (ADI) [36 - 40] is a technique when applied to the FDTD method it enables simulations to go beyond the Courant limit without incurring instability. This means that the time-step size in the ADI-FDTD method is not bounded by the Courant criterion expressed by Eq. (3.18). This feature greatly reduces the number of time-steps needed to complete a single simulation, which in turn reduces the demand on computational resources. Unfortunately, the time-step size affects the numerical accuracy of the ADI-FDTD method, setting a limit on the size of the larger time-steps [37 - 38].

The ADI-FDTD method is a semi implicit solving technique, where the field component, such as the electric field, is solved implicitly in the first half time step and explicitly in the second half time step [41]. This means that the EM field components are arranged in space according to the Yee lattice, as shown in Fig. 3.1. However, in time, the EM field components do not follow the leapfrog arrangement. In the ADI-

FDTD method a single time step is divided into two halves in which the EM field components are collocated and not staggered as in the conventional FDTD method. The following equations are obtained from equations (3.1 - 3.6) for the first half time step

$$E_x\Big|_{i+1/2,j,k}^{n+1/2} = E_x\Big|_{i+1/2,j,k}^{n} + \frac{\Delta t}{2\varepsilon\Delta y}\left(H_z\Big|_{i+1/2,j+1/2,k}^{n+1/2} - H_z\Big|_{i+1/2,j-1/2,k}^{n+1/2}\right) - \frac{\Delta t}{2\varepsilon\Delta z}\left(H_y\Big|_{i+1/2,j,k+1/2}^{n} - H_y\Big|_{i+1/2,j,k-1/2}^{n}\right) \tag{3.20}$$

$$E_y\Big|_{i,j+1/2,k}^{n+1/2} = E_y\Big|_{i,j+1/2,k}^{n} + \frac{\Delta t}{2\varepsilon\Delta z}\left(H_x\Big|_{i,j+1/2,k+1/2}^{n+1/2} - H_x\Big|_{i,j+1/2,k-1/2}^{n+1/2}\right) - \frac{\Delta t}{2\varepsilon\Delta x}\left(H_z\Big|_{i+1/2,j+1/2,k}^{n} - H_z\Big|_{i-1/2,j+1/2,k}^{n}\right) \tag{3.21}$$

$$E_z\Big|_{i,j,k+1/2}^{n+1/2} = E_z\Big|_{i,j,k+1/2}^{n} + \frac{\Delta t}{2\varepsilon\Delta x}\left(H_y\Big|_{i+1/2,j,k+1/2}^{n+1/2} - H_y\Big|_{i-1/2,j,k+1/2}^{n+1/2}\right) - \frac{\Delta t}{2\varepsilon\Delta y}\left(H_x\Big|_{i,j+1/2,k+1/2}^{n} - H_x\Big|_{i,j-1/2,k+1/2}^{n}\right) \tag{3.22}$$

$$H_x\Big|_{i,j+1/2,k+1/2}^{n+1/2} = H_x\Big|_{i,j+1/2,k+1/2}^{n} + \frac{\Delta t}{2\mu\Delta z}\left(E_y\Big|_{i,j+1/2,k+1}^{n+1/2} - E_y\Big|_{i,j+1/2,k}^{n+1/2}\right) - \frac{\Delta t}{2\varepsilon\Delta y}\left(E_z\Big|_{i,j+1,k+1/2}^{n} - E_z\Big|_{i,j,k+1/2}^{n}\right) \tag{3.23}$$

$$H_y\Big|_{i+1/2,j,k+1/2}^{n+1/2} = H_x\Big|_{i+1/2,j,k+1/2}^{n} + \frac{\Delta t}{2\mu\Delta x}\left(E_z\Big|_{i+1,j,k+1/2}^{n+1/2} - E_z\Big|_{i,j,k+1/2}^{n+1/2}\right) - \frac{\Delta t}{2\varepsilon\Delta z}\left(E_x\Big|_{i+1/2,j,k+1}^{n} - E_x\Big|_{i+1/2,j,k}^{n}\right) \tag{3.24}$$

$$H_z\Big|_{i+1/2,j+1/2,k}^{n+1/2} = H_x\Big|_{i+1/2,j+1/2,k}^{n} + \frac{\Delta t}{2\mu\Delta y}\left(E_x\Big|_{i+1/2,j+1,k}^{n+1/2} - E_x\Big|_{i+1/2,j,k}^{n+1/2}\right) - \frac{\Delta t}{2\varepsilon\Delta x}\left(E_y\Big|_{i+1,j+1/2,k}^{n} - E_y\Big|_{i,j+1/2,k}^{n}\right) \tag{3.25}$$

It should be noted here that in equations (3.20 - 3.25) some of the electric and magnetic field components are collocated in time and thus cannot be explicitly updated. Each electric, or magnetic, field component has a tri-diagonal system of equations that

can be solved. After the tri-diagonal system is solved, the remaining electric, or magnetic, field components are explicitly updated. As for the second half time-step, the equations to be solved are as follows

$$E_x\Big|_{i+1/2,j,k}^{n+1} = E_x\Big|_{i+1/2,j,k}^{n+1/2} + \frac{\Delta t}{2\varepsilon\Delta y}\left(H_z\Big|_{i+1/2,j+1/2,k}^{n+1/2} - H_z\Big|_{i+1/2,j-1/2,k}^{n+1/2}\right) - \frac{\Delta t}{2\varepsilon\Delta y}\left(H_y\Big|_{i+1/2,j,k+1/2}^{n+1} - H_y\Big|_{i+1/2,j,k-1/2}^{n+1}\right) \tag{3.26}$$

$$E_y\Big|_{i,j+1/2,k}^{n+1} = E_y\Big|_{i,j+1/2,k}^{n+1/2} + \frac{\Delta t}{2\varepsilon\Delta z}\left(H_x\Big|_{i,j+1/2,k+1/2}^{n+1/2} - H_x\Big|_{i,j+1/2,k-1/2}^{n+1/2}\right) - \frac{\Delta t}{2\varepsilon\Delta x}\left(H_z\Big|_{i+1/2,j+1/2,k}^{n+1} - H_z\Big|_{i-1/2,j+1/2,k}^{n+1}\right) \tag{3.27}$$

$$E_z\Big|_{i,j,k+1/2}^{n+1} = E_z\Big|_{i,j,k+1/2}^{n+1/2} + \frac{\Delta t}{2\varepsilon\Delta x}\left(H_y\Big|_{i+1/2,j,k+1/2}^{n+1/2} - H_y\Big|_{i-1/2,j,k+1/2}^{n+1/2}\right) - \frac{\Delta t}{2\varepsilon\Delta y}\left(H_x\Big|_{i,j+1/2,k+1/2}^{n+1} - H_x\Big|_{i,j-1/2,k+1/2}^{n+1}\right) \tag{3.28}$$

$$H_x\Big|_{i,j+1/2,k+1/2}^{n+1} = H_x\Big|_{i,j+1/2,k+1/2}^{n+1/2} + \frac{\Delta t}{2\mu\Delta z}\left(E_y\Big|_{i,j+1/2,k+1}^{n+1/2} - E_y\Big|_{i,j+1/2,k}^{n+1/2}\right) - \frac{\Delta t}{2\varepsilon\Delta y}\left(E_z\Big|_{i,j+1,k+1/2}^{n+1} - E_z\Big|_{i,j,k+1/2}^{n+1}\right) \tag{3.29}$$

$$H_y\Big|_{i+1/2,j,k+1/2}^{n+1} = H_x\Big|_{i+1/2,j,k+1/2}^{n+1/2} + \frac{\Delta t}{2\mu\Delta x}\left(E_z\Big|_{i+1,j,k+1/2}^{n+1/2} - E_z\Big|_{i,j,k+1/2}^{n+1/2}\right) - \frac{\Delta t}{2\varepsilon\Delta z}\left(E_x\Big|_{i+1/2,j,k+1}^{n+1} - E_x\Big|_{i+1/2,j,k}^{n+1}\right) \tag{3.30}$$

$$H_z\Big|_{i+1/2,j+1/2,k}^{n+1} = H_x\Big|_{i+1/2,j+1/2,k}^{n+1/2} + \frac{\Delta t}{2\mu\Delta y}\left(E_x\Big|_{i+1/2,j+1,k}^{n+1/2} - E_x\Big|_{i+1/2,j,k}^{n+1/2}\right) - \frac{\Delta t}{2\varepsilon\Delta x}\left(E_y\Big|_{i+1,j+1/2,k}^{n+1} - E_y\Big|_{i,j+1/2,k}^{n+1}\right) \tag{3.31}$$

Here, a similar procedure as applied on the first half time-step is applied on the second half time-step. Time stepping for the ADI-FDTD is by the repetition of the two previous procedures in time.

The unconditional stability of the ADI-FDTD method is due to the semi-explicit nature of the technique [36], [39 – 40]. This allows for time step sizes larger than the limit imposed by Eq. (3.17) in the conventional FDTD method. However, the downside to the ADI-FDTD method is that it suffers from high numerical dispersion when using a high Courant number [42]; the larger the time step size used the larger the numerical dispersion [37 - 38]. Nevertheless, the ADI-FDTD produces accurate results with highly reduced demands on the computational resources for time step sizes up to 8 times larger than the Courant criterion [37 - 38] and can be extended up to 400 times the Courant criterion for signals with narrow frequency bandwidths [43].

In order to reduce the numerical dispersion caused by the ADI-FDTD, the complex envelope technique can be used [44] where all electromagnetic field components are assumed to satisfy the Slowly-Varying Envelope Approximation (SVEA), as explained in detail in the following section.

3.5 Complex Envelope Alternating Direction Implicit Finite Difference Time Domain

As mentioned in the previous section of this chapter, FDTD has proven to be one of the most popular modelling techniques due to its high ability to deal with a wide range of photonic devices. Being such an explicit technique that depends heavily on field update at each step without the need of matrix inversions make it attractive to use when modelling extremely complicated structures on desktop computers. The main drawback of conventional FDTD is the high demand it has upon computational

resources due to the Courant criterion, which sets the bounds of the time-step size so as to avoid numerical instability [2]. In order to circumvent the Courant criterion limitation, several techniques have been proposed. Among these techniques is the method proposed by Rao *et al.* in [45], known as CE-ADI-FDTD. This method is quite popular for photonic simulations due to its low numerical dispersion, reduction of required computational resources, and highly accurate results in comparison with the conventional ADI-FDTD algorithm. Hence, CE-ADI-FDTD uses larger time steps, meaning, less computational burden, yet provides high accuracy. Using the formulated method in [2] eliminates the stability problem that arises in Rao's method because of the employment of perfectly matched layer. This method is based upon applying an alternating forward and backward difference to the calculation of the derivatives of the coefficient of the PML equations, allowing better performance in when considering the absorption of impinging waves on PML [2].

The following equations are discretised in space based on the unit cell of the Yee space lattice allowing the grid to be non-uniform. While discretisation in time is obtained by following the procedure in [31], the space cells are non-uniform so as to allow more accurate and flexible representation of the photonic device. In the CE-ADI-FDTD method all electromagnetic field components are assumed to satisfy the slowly-varying envelope approximation as illustrated in Fig. 3.3.

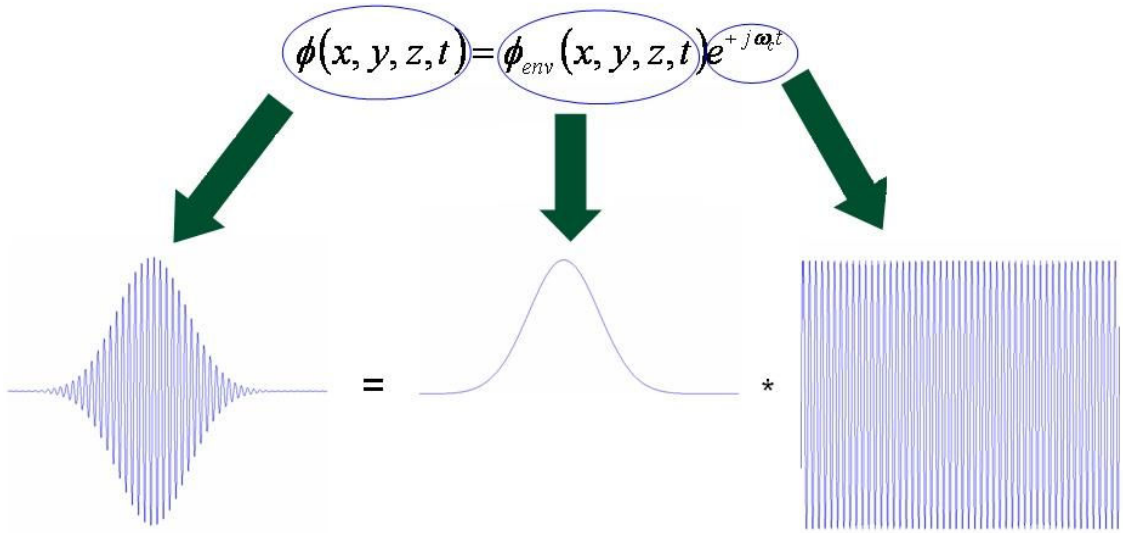

Figure 3.3 Slowly-varying envelope approximation [46]

where $\varphi(x,y,z,t)$ is the field component, $\varphi_{env}(x,y,z,t)$ is the slowly-varying amplitude, $e^{-j\omega_c t}$ is the fast varying carrier, and ω_c is the angular frequency of the carrier. The idea behind this alternating-direction mechanism is that the time step is split into two halves. One half time-step is selected to perform the explicit extraction of the magnetic field, while the other half step uses the technique of implicit extraction. The explicit method simply relies on obtaining the magnetic field of time step $n + 1$ from previous values of the electric field at time step n. While the implicit method involves solving a system of equations for the magnetic field at $n + 0.5$ by substituting the electric field value at time step $n + 0.5$ with the electric field at n and the magnetic field at $n + 0.5$ and thus solving the system implicitly.

The alternating-direction provides implicit solving of a system of equations, which in turn provides higher stability beyond the Courant limit.

The following set of equations for the 1st half time step are shown below [2]

$$H_{xa}\big|_{i,j+1/2}^{n+1/2} = \alpha_{xh}\big|_{i,j+1/2} H_{xa}\big|_{i,j+1/2}^{n} - \beta_{xh}\big|_{i,j+1/2} \left(E_{za}\big|_{i,j+1}^{n} - E_{za}\big|_{i,j}^{n}\right) \tag{3.32}$$

$$H_{ya}\big|_{i+1/2,j}^{n+1/2} = \alpha_{yh}\big|_{i+1/2,j}\, H_{ya}\big|_{i+1/2,j}^{n} + \beta_{yh}\big|_{i+1/2,j}\left(E_{za}\big|_{i+1,j}^{n+1/2} - E_{za}\big|_{i,j}^{n+1/2}\right) \tag{3.33}$$

$$\begin{aligned} E_{za}\big|_{i,j}^{n+1/2} &= \alpha_{e}\big|_{i,j}\, E_{za}\big|_{i,j}^{n} + \beta_{xe}\big|_{i,j}\left(H_{ya}\big|_{i+1/2,j}^{n+1/2} - H_{ya}\big|_{i-1/2,j}^{n+1/2}\right) + \\ &- \beta_{yh}\big|_{i,j}\left(H_{xa}\big|_{i,j+1/2}^{n} - H_{xa}\big|_{i,j-1/2}^{n}\right) \end{aligned} \tag{3.34}$$

while for the 2nd half time step, the following set of equations are obtained

$$H_{xa}\big|_{i,j+1/2}^{n+1} = \alpha_{xh}\big|_{i,j+1/2}\, H_{xa}\big|_{i,j+1/2}^{n+1/2} - \beta_{xh}\big|_{i,j+1/2}\left(E_{za}\big|_{i,j+1}^{n+1} - E_{za}\big|_{i,j}^{n+1}\right) \tag{3.35}$$

$$H_{ya}\big|_{i+1/2,j}^{n+1} = \alpha_{yh}\big|_{i+1/2,j}\, H_{ya}\big|_{i+1/2,j}^{n+1/2} + \beta_{yh}\big|_{i+1/2,j}\left(E_{za}\big|_{i+1,j}^{n+1/2} - E_{za}\big|_{i,j}^{n+1/2}\right) \tag{3.36}$$

$$\begin{aligned} E_{za}\big|_{i,j}^{n+1} &= \alpha_{e}\big|_{i,j}\, E_{za}\big|_{i,j}^{n+1/2} + \beta_{xe}\big|_{i,j}\left(H_{ya}\big|_{i+1/2,j}^{n+1/2} - H_{ya}\big|_{i-1/2,j}^{n+1/2}\right) + \\ &- \beta_{yh}\big|_{i,j}\left(H_{xa}\big|_{i,j+1/2}^{n+1} - H_{xa}\big|_{i,j-1/2}^{n+1}\right) \end{aligned} \tag{3.37}$$

where

$$\alpha_{xh}\big|_{i,j+1/2} = \alpha_{yh}\big|_{i+1/2,j} = \alpha_{e}\big|_{i,j} = \frac{4 - j\omega_c\Delta t}{4 + j\omega_c\Delta t} \tag{3.38}$$

$$\beta_{xh}\big|_{i,j+1/2} = \frac{2\Delta t}{(4 + j\omega_c\Delta t)\mu_r\mu_0\Delta y_j} \tag{3.39}$$

$$\beta_{yh}\big|_{i+1/2,j} = \frac{2\Delta t}{(4 + j\omega_c\Delta t)\mu_r\mu_0\Delta x_i} \tag{3.40}$$

$$\beta_{xe}\big|_{i,j} = \frac{2\Delta t}{(4 + j\omega_c\Delta t)\varepsilon_r\varepsilon_0 h_{xi}} \tag{3.41}$$

$$\beta_{ye}\big|_{i,j} = \frac{2\Delta t}{(4 + j\omega_c\Delta t)\varepsilon_r\varepsilon_0 h_{yj}} \tag{3.42}$$

where Δt is the time step, Δx_i and Δy_j are the discretised steps along x- and y-directions, respectively, and h_{xi} and h_{yj} are defined as

$$h_{xi} = \frac{\Delta x_i + \Delta x_{i-1}}{2} \qquad i = 2,3,\ldots,N_x \tag{3.43}$$

$$h_{yj} = \frac{\Delta y_j + \Delta y_{j-1}}{2} \qquad j = 2,3,...,N_y \tag{3.44}$$

where N_x and N_y are the total number of cells of the computational domain along x- and y- direction, respectively. The updating process of the 1st half time step starts with the explicit update of Eq. (3.32) in order to obtain the new values of the magnetic field component H_{xa}. As can be seen, Eq. (3.33) cannot be explicitly solved. Substituting (3.34) into (3.33) and solving the derived equation for H_{ya}, a system of equations can be derived in [2], whose coefficients form a tridiagonal matrix which can be efficiently solved in order to obtain the new values of the magnetic field component H_{ya} inside the computational domain. Once the magnetic field component H_{ya} has been calculated, E_{za} can be explicitly updated using Eq. (3.34). A similar procedure can be followed on 2nd half time step for equations (3.35 - 3.37) [2].

3.6 Excitation Methods

3.6.1 Hard source and soft source

Two types of internal sources can be used with FDTD to excite the electromagnetic propagation inside the simulated structure: *hard source* and *soft source*. Setting up a hard source means simply to assign the value of the *E*- or *H*- field at one or more FDTD grid points in space equal to a desired function of time. It becomes like the initial condition of an electromagnetic problem in which the *E*- or *H*- field is known at a point and the values of the radiated fields at the other grid points need to be calculated. Depending on how many points values are assigned in space, the source can be

pointwise or a plane wave. As example, in a 1D system, with propagation in *x*-direction, a pointwise hard source can be imposed as follows

$$E_z\big|_{i_{source}}^{n} = E_0 \sin\left(2\pi f_0 n\Delta t\right) \tag{3.45}$$

where a sinusoidal hard source (continuous wave, CW) E_z is assigned at the grid point i_{source} and it starts at the time step $n = 0$. As a result, the wave will propagate in both the directions back, $-x$, and forward, $+x$, from the starting point.

Another commonly used wave source is the low-pass Gaussian pulse that is centred in time at the step n_0 and has $1/e$ characteristic decay of a number n_{decay} of time steps

$$E_z\big|_{i_{source}}^{n} = E_0 e^{-\left(\frac{n-n_0}{n_{decay}}\right)^2} \sin\left(2\pi f_0 n\Delta t\right) \tag{3.46}$$

This function presents a finite direct current component and its Fast Fourier Transform (FFT) is centred at frequency f_0.

An important aspect of hard source condition is that for a source like the Gaussian, after a total simulation time greater than $(n_0 + n_{decay})$, the hard source acts as an electric mirror or Perfect Electric Conductor (PEC); the total tangential E-field is equal to zero. Therefore, it cannot take into account the movement of reflected waves through the input section i_{source}. Also, in the case of a CW, when the tangential E-field value at the excitation does not come to zero at a certain time, it is demonstrated that a spurious and nonphysical back-reflection of the waves toward the $+x$ direction of propagation is caused. This happens in any kind of imposed time function because at the source section a particular value of E-field is specified without considering in any way

the effect of an incident field eventually occurring at the same section. A way to avoid this effect can be to switch off the hard source after its time function has decayed to zero by replacing the equation at i_{source} with the standard FDTD update equations. However, this strategy can be adopted only in case of pulse wave forms that evolve in time only for a certain interval and not for continuous interacting sources such as a sinusoidal wave.

Alternatively, a soft source consists in the introduction of an electric current. It adds the value of the source time function at the FDTD current value of the field at the point i_{source}. As a result, the effect of the radiated propagating fields at the source interface will be considered and spurious reflections avoided. The soft source is imposed through the following

$$E_z\big|_{i_{source}}^{n} = E_z\big|_{i_{source}}^{n-1} + source\big|^{n}, \quad \text{for every } n, \tag{3.47}$$

An existing problem with soft source is that it generates a nonzero DC component in the solution. This variation on the amplitude of the fields has to be considered in order to achieve correct results. A solution of this problem has been proposed by Furse *et al*. in 2000, [47]. It consists in applying a modified source function as

$$r(t)\sin(\omega t) \tag{3.48}$$

where *r(t)* represents a turn-on function defined by

$$r(t)=\begin{cases}0 & \\ 0.5\left[1-\cos\left(\dfrac{\omega t}{2\alpha}\right)\right] & 0\le t\le \alpha T \\ 1 & t>\alpha T\end{cases} \tag{3.49}$$

where T representing the period of the time-harmonic source and α=1/2, 3/2, 5/2, …

3.7 Summary

This chapter has covered the essential numerical techniques with their derivations, starting from the Yee lattice, looking at the leapfrog, and the FDTD. Numerical dispersion and numerical stability constraints were discussed, and the appropriate method to overcome the Courant time constraint was presented in the form of the ADI-FDTD. Following that, the numerical dispersion caused by the ADI-FDTD was circumvented through implementing the complex envelope technique where all electromagnetic field components satisfy the slowly-varying envelope approximation. Finally, the source excitation methods were categorised as hard and soft sources, and these sources were discussed.

Since these numerical methods are applied to electromagnetic wave interaction in optical waveguides with infinitely extended computational domains, it is important to apply boundary conditions surrounding the computational domain to emulate free space in computer simulations. These boundary conditions are presented in detail in chapter 4.

Chapter 4

Absorbing Boundary Conditions and Perfectly Matched Layers

4.1 Introduction

This chapter discusses the boundary conditions applied around computational domains. First it covers perfectly matched layer boundary conditions, looking at the basic principles and representing these principles in the form of equations. Then, the uniaxial perfectly matched layer absorbing boundary conditions, and the perfectly matched layer parameters. Next, the chapter presents PML boundary conditions for CE-ADI-FDTD. Finally, the newly suggested PML formulation is presented.

4.2 Perfectly Matched Layer Boundary Conditions

Electromagnetic wave interaction problems in optical waveguides are usually defined in unbounded spatial domains of their computational fields in one or more coordinates otherwise known as open regions or infinitely extended regions. However, computers are limited in their storage capacity and they can only process computational domains that are limited in size. Therefore, much research effort has been put into finding a way to simulate an infinitely extended computational domain using computers.

4.2.1 Basic principles

Literature shows that the most sensible way to overcome this problem is by using a computational domain large enough to surround the structure of interest, and set appropriate boundary conditions (BCs) on the outer limits of the domain in order to simulate the structure's extension to infinity. Such boundary conditions can be set in two main categories; Analytical Boundary Conditions [48 − 53] and Absorbing Boundary Conditions [54]. Mur in [49] proposes an analytical boundary conditions method highly utilised for its accuracy on the simulation of the outgoing waves from the computational domain. While Berenger in [54] presents highly effective absorbing-material boundary conditions method known as the PML which is widely used [55 - 59].

Berenger terminates the outer boundary of the space lattice in a non-physical absorbing material medium. This non-physical layer is ideally a few lattice cells thick, and is reflectionless as it has the ability to absorb all impinging electromagnetic waves on the full frequency spectrum. This particular layer assured that plane waves with any polarisation and for all angles of incidence were matched at boundary.

Berenger's derivations for the PML are based on splitting the electromagnetic

field components of Maxwell's equations in such a way that each component is split in two orthogonal components. Maxwell's curl equations are also suitably split, and then appropriate loss parameters consistent with a dispersionless medium are set to each component [35]. To establish a foundation for the discussion of PML absorbers based on Berenger's technique, the derivation of the properties of this non-physical medium is shown in this section and can be found in full detail in [35]. In order to do so, a 2D space is considered as shown in Fig. 4.1.

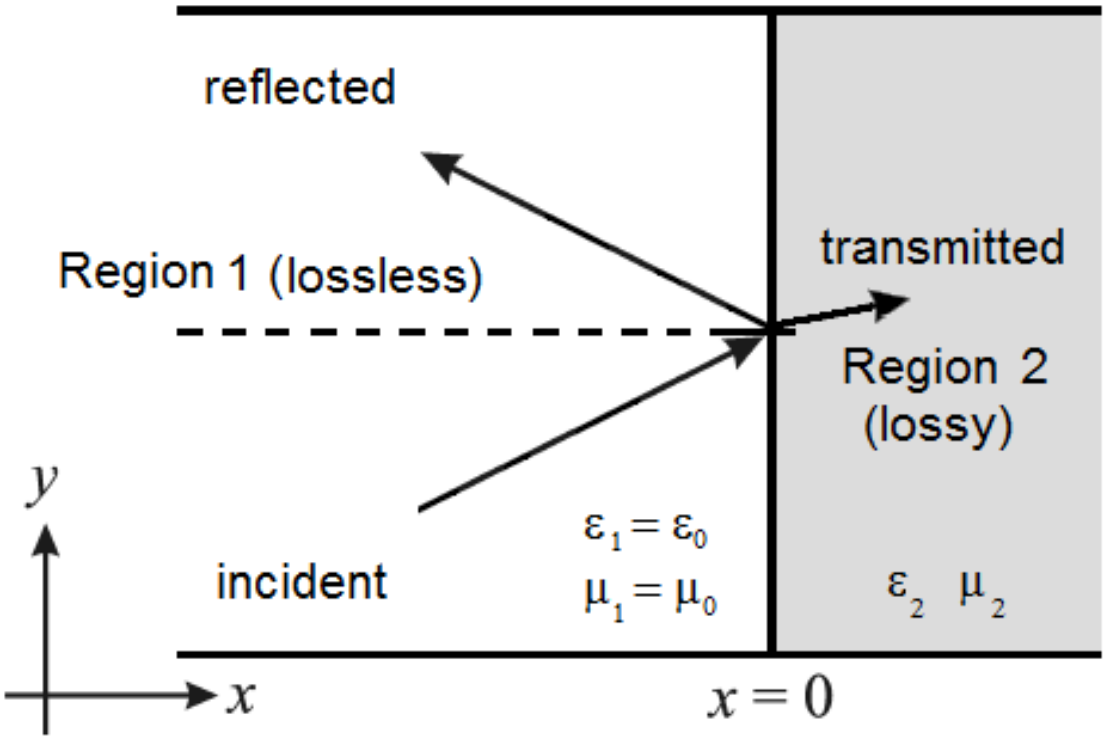

Figure 4.1 2D schematics of a plane wave with TE_z polarisation propagating between two media

Fig. 4.1 is an illustration of a 2D media that is split into two regions; region 1, where $x < 0$, is lossless, while region 2, where $x > 0$ is lossy. In region 1 the electric permittivity and the magnetic permeability are $\varepsilon_1 = \varepsilon_0$ and $\mu_1 = \mu_0$, respectively. Whereas, in medium 2 the electric permittivity, magnetic permeability, electric

conductivity, and magnetic loss are ε_2, μ_2, σ, and σ^*, respectively.

4.2.2 Basic equations

When an incident uniform plane wave with TE_z polarisation propagates from region 1 to region 2 the wave can be described as

$$\vec{H}_{inc} = H_0 e^{-(j\beta_x^i x + j\beta_y^i y)} \vec{u}_z \tag{4.1}$$

where H_{inc} is the incident magnetic field, H_0 is the amplitude of the magnetic field, β_x^i and β_y^i are the propagation constant components of the plane wave along x and y direction, respectively, and $\boldsymbol{u}_z$ is the unit normal vector of z axis. As the plane wave crosses from region 1 into region 2 it is partially reflected back into region 1 and the remainder of the plane wave is transmitted into region 2, the total fields in region 1 can be described as in equations (4.2 – 4.3)

$$\vec{H}_1 = H_0 \left(1 + \Gamma e^{j2\beta_x^i}\right) e^{-(j\beta_x^i x + j\beta_y^i y)} \vec{u}_z \tag{4.2}$$

$$\vec{E}_1 = \left[-\frac{\beta_y^i}{\omega\varepsilon_1} \left(1 + \Gamma e^{j2\beta_x^i}\right) \vec{u}_x + \frac{\beta_x^i}{\omega\varepsilon_1} \left(1 - \Gamma e^{j2\beta_x^i}\right) \vec{u}_y \right] H_0 e^{-(j\beta_x^i x + j\beta_y^i y)} \tag{4.3}$$

where E_1 is the electric field, ω is the frequency of the plane wave, Γ is the reflection coefficient, and $\boldsymbol{u}_x$ and $\boldsymbol{u}_y$ are the unit normal vectors of the x and y axes, respectively.

Considering the part of the TE_z plane wave that is transmitted into region 2 Maxwell's curl equations in time-harmonic form can be expressed as

$$j\omega\varepsilon_2 \left(1 + \frac{\sigma}{j\omega\varepsilon_0}\right) E_x = \frac{\partial H_z}{\partial y} \tag{4.4}$$

$$j\omega\varepsilon_2 \left(1 + \frac{\sigma}{j\omega\varepsilon_0}\right) E_y = -\frac{\partial H_z}{\partial x} \tag{4.5}$$

$$j\omega\mu_2\left(1+\frac{\sigma^*}{j\omega\mu_0}\right)H_z=\frac{\partial E_x}{\partial y}-\frac{\partial E_y}{\partial x} \tag{4.6}$$

where the electric conductivity σ and the magnetic loss σ^* are normalised with respect to the electric permittivity ε_0 and the magnetic permeability μ_0 , respectively. With some mathematical manipulation and knowing that

$$H_z=H_{zx}+H_{zy} \tag{4.7}$$

$$s_i=1+\frac{\sigma_i}{j\omega\varepsilon_0} \tag{4.8}$$

$$s_i^*=1+\frac{\sigma_i^*}{j\omega\mu_0} \tag{4.9}$$

equations (4.4 - 4.6) can be expressed as

$$j\omega\varepsilon_2 s_y E_x=\frac{\partial\left(H_{zx}+H_{zy}\right)}{\partial y} \tag{4.10}$$

$$j\omega\varepsilon_2 s_x E_y=-\frac{\partial\left(H_{zx}+H_{zy}\right)}{\partial x} \tag{4.11}$$

$$j\omega\mu_2 s_x^* H_{zx}=-\frac{\partial E_y}{\partial x} \tag{4.12}$$

$$j\omega\mu_2 s_y^* H_{zy}=\frac{\partial E_x}{\partial y} \tag{4.13}$$

Differentiating equations (4.10) and (4.11) by y and x, respectively, then substituting the expressions for $\frac{\partial E_y}{\partial x}$ and $\frac{\partial E_x}{\partial y}$ from equations (4.12) and (4.13), respectively, leads to

$$-\omega^2\mu_2\varepsilon_2 H_{zx}=-\frac{1}{s_x^*}\frac{\partial}{\partial x}\frac{1}{s_x}\frac{\partial}{\partial x}\left(H_{zx}+H_{zy}\right) \tag{4.14}$$

$$-\omega^2\mu_2\varepsilon_2 H_{zy} = -\frac{1}{s_y^*}\frac{\partial}{\partial y}\frac{1}{s_y}\frac{\partial}{\partial y}\left(H_{zx} + H_{zy}\right) \tag{4.15}$$

Adding equations (4.14) and (4.15) leads to the wave equation

$$\frac{1}{s_x^*}\frac{\partial}{\partial x}\frac{1}{s_x}\frac{\partial}{\partial x}H_z + \frac{1}{s_y^*}\frac{\partial}{\partial y}\frac{1}{s_y}\frac{\partial}{\partial y}H_z + \omega^2\mu_2\varepsilon_2 H_z = 0 \tag{4.16}$$

which supports the solution

$$H_z = H_0 T e^{-(j\sqrt{s_x s_x^*}\beta_x x + j\sqrt{s_y s_y^*}\beta_y y)} \tag{4.17}$$

with the dispersion relationship

$$(\beta_{2_x})^2 + (\beta_{2_y})^2 = (k_2)^2 \tag{4.18}$$

Substituting Eq. (4.17) into equations (4.10 - 4.11) leads to the following equations for the electric field components

$$E_x = H_0 T \frac{\beta_y}{\omega\varepsilon_2}\sqrt{\frac{s_y^*}{s_y}}e^{-(j\sqrt{s_x s_x^*}\beta_x x + j\sqrt{s_y s_y^*}\beta_y y)} \tag{4.19}$$

$$E_y = H_0 T \frac{\beta_x}{\omega\varepsilon_2}\sqrt{\frac{s_x^*}{s_x}}e^{-(j\sqrt{s_x s_x^*}\beta_x x + j\sqrt{s_y s_y^*}\beta_y y)} \tag{4.20}$$

Enforcing the continuity of the tangential electromagnetic fields at the interface ($x = 0$), where $s_y = s_y^* = 1$, or equivalently, $\sigma_y = 0 = \sigma_y^*$, this yields the phase-matching condition $\beta_{2_y} = \beta_{1_y} = k_1 sin\theta$. Further, the magnetic field reflection and transmission coefficients can be expressed as

$$\Gamma = \frac{\frac{\beta_x^i}{\omega\varepsilon_1} - \frac{\beta_x}{\omega\varepsilon_2}\sqrt{\frac{s_x^*}{s_x}}}{\frac{\beta_x^i}{\omega\varepsilon_1} + \frac{\beta_x}{\omega\varepsilon_2}\sqrt{\frac{s_x^*}{s_x}}} \tag{4.21}$$

From Eq. (4.21) it can be noted that if $\varepsilon_1 = \varepsilon_2$, and $s_x = s_x^*$, then $\beta_x = \beta_x^i$. This

means that the reflection coefficient is Γ = 0 and the transmission coefficient is T = 1, which is true for all incident angles θ. Since $s_x = s_x^*$, this implies that $\sigma_x / \varepsilon_0 = \sigma_x^* / \mu_0$. The transmitted field on region 2 is

$$H_z = H_0 e^{-\left(js_x\beta_x^i x + js\beta_{y,y}^i\right)} = H_0 e^{-\left(j\beta_x^i x + js\beta_y^i y\right)} e^{-\sigma\eta_1\varepsilon_1\cos(\theta_i)x} \tag{4.22}$$

$$E_x = H_0\eta_1 \sin(\theta_i) e^{-\left(j\beta_x^i x + js\beta_y^i y\right)} e^{-\sigma\eta_1\varepsilon_1\cos(\theta_i)x} \tag{4.23}$$

$$E_y = H_0\eta_1 \cos(\theta_i) e^{-\left(j\beta_x^i x + js\beta_y^i y\right)} e^{-\sigma\eta_1\varepsilon_1\cos(\theta_i)x} \tag{4.24}$$

Within the above matched region 2 medium, the transmitted wave propagates at the same speed and direction as the impinging wave from region 1. The wave also, simultaneously, experiences attenuation along the *x*-axis normal to the interface between regions 1 and 2. The attenuation factor $\sigma_x\eta_1 cos(\theta)$ is independent of frequency and these properties are valid for all angles of incidence.

The TM_z polarised plane waves can similarly be derived. However, the splitting of the electromagnetic field components is applied to the electric field $E_z = E_{zx} + E_{zy}$. In which Γ = 0 and T =1 as a result of $s_x = s_x^*$, and $\sigma_x / \varepsilon_0 = \sigma_x^* / \mu_0$. Again all these properties are valid for all angles of incidence.

From the above analysis the FDTD grid can use PMLs to greatly reduce outer-boundary reflections. These layers of non-physical and absorbing medium with absorbing properties are in turn backed by PEC walls to terminate the whole computational domain, as shown in Fig. 4.2 for a 2D case.

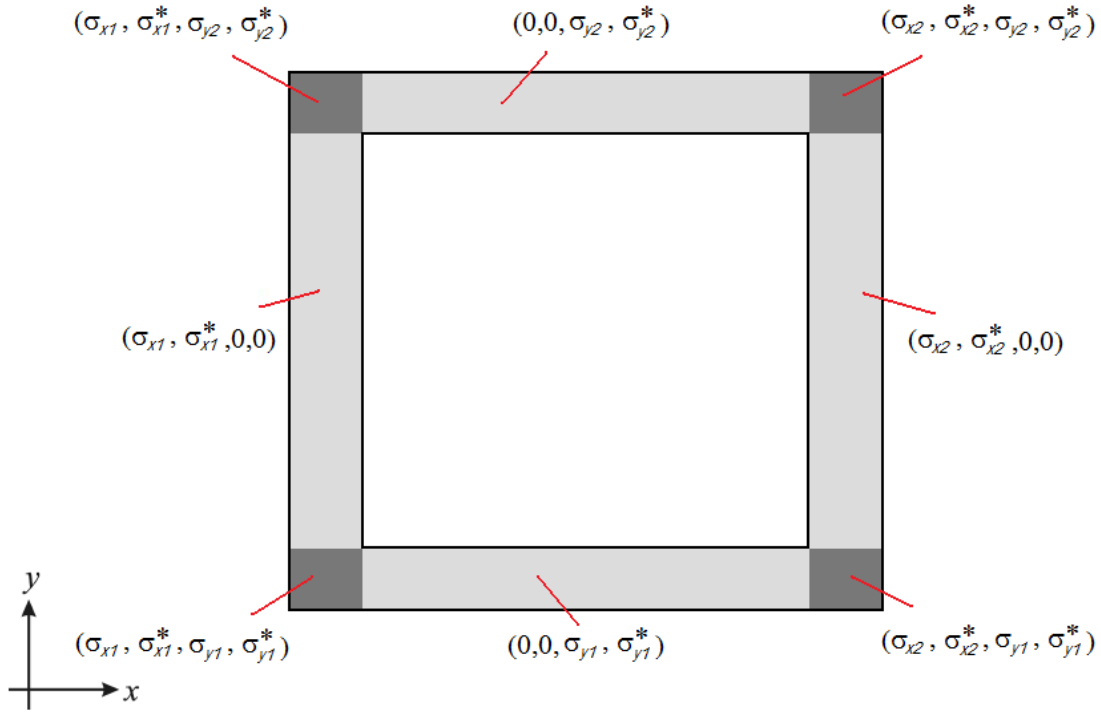

Figure 4.2 Schematics of a 2D computational domain surrounded by 4 layers of PML BCs.

4.3 Uniaxial Perfectly Matched Layer Absorbing Boundary Conditions

Berenger established the split-field PML technique as a theoretical non-physical medium that is based on a mathematical model. The nature of the loss terms of the impinging electromagnetic wave make this region anisotropic perfectly matched medium. For a single interface the anisotropic medium is uniaxial, having a composition of both electric and magnetic permittivity tensors. This new approach by Sacks *et al*. [60] leads to absorbing layers called uniaxial perfectly matched layers. This UPML material avoids the non-physical field splitting while maintaining performance as well as Berenger's PML [35].

In Fig. 4.1 above, if we consider a TE_z polarised plane wave propagates from a lossless region 1 into an uniaxial medium in region 2, where the two regions are separated by the interface at $x = 0$, whose electric and magnetic tensors are given by [35] $\overline{\overline{\varepsilon}} = \varepsilon_2 \overline{\overline{s}}$, $\overline{\overline{\mu}} = \mu_2 \overline{\overline{s}}$ where

$$\overline{\overline{\varepsilon}}_2 = \varepsilon_2 \begin{bmatrix} a & 0 & 0 \\ 0 & b & 0 \\ 0 & 0 & b \end{bmatrix}, \quad \overline{\overline{\mu}}_2 = \mu_2 \begin{bmatrix} c & 0 & 0 \\ 0 & d & 0 \\ 0 & 0 & d \end{bmatrix}, \quad \overline{\overline{s}} = \begin{bmatrix} s_x^{-1} & 0 & 0 \\ 0 & s_x & 0 \\ 0 & 0 & s_x \end{bmatrix} \tag{4.25}$$

here s_x is defined as in equations (4.8) and (4.9), ε_2 and μ_2 are the electric permittivity and the magnetic permeability of the uniaxial medium in region 2, respectively. No reflection is generated, and the plane wave is completely transmitted into the uniaxial region for all angles of incidence θ. Since the reflection coefficient is $\Gamma = 0$ and the transmission coefficient is $\mathrm{T} = 1$, the transmitted electromagnetic field components can be expressed as

$$H_z = H_0 e^{-\left(j s_x \beta_x^i x + j s \beta_y^i y\right)} = H_0 e^{-\left(j\beta_x^i x + j\beta_y^i y\right)} e^{-\sigma \eta_1 \varepsilon_1 \cos(\theta_i) x} \tag{4.26}$$

$$E_x = -H_0 s_x \eta_1 \sin\left(\theta_i\right) e^{-\left(j\beta_x^i x + j s \beta_y^i y\right)} e^{-\sigma \eta_1 \varepsilon_1 \cos(\theta_i) x} \tag{4.27}$$

$$E_y = H_0 \eta_1 \cos\left(\theta_i\right) e^{-\left(j\beta_x^i x + j s \beta_y^i y\right)} e^{-\sigma \eta_1 \varepsilon_1 \cos(\theta_i) x} \tag{4.28}$$

where θ_i in the angle of incidence relative to x axis. Equations (4.26 - 4.28) show that regions 1 and 2 are perfectly matched such that the transmitted wave in region 2 propagates at the same speed and direction as the impinging wave from region 1. The wave also, simultaneously, experiences attenuation along the x-axis normal to the interface between regions 1 and 2. The attenuation factor $\sigma\varepsilon_1 cos(\theta_i)$ is independent of

frequency and these properties are valid for all angles of incidence. Comparing equations (4.26 - 4.28) with (4.22 - 4.24), it is noted that Berenger's split-field PML and the UPML have identical propagation characteristics, since both result in the same wave equation. The tangential electric and magnetic field components, H_z and E_y, of the two methods are identical, while the normal component, E_x, differs by a factor s_x. The two methods also show that the normal components of the transmitted field differ. That is, for the PML formulation the E_x component is continuous at $x = 0$, whereas in the UPML formulation E_x is discontinuous with $D_x = \varepsilon s_x^{-1} E_x$ continuous. This difference in continuity of the normal component is because the two techniques use two different formulations of the divergence theorem. However, these two formulations still produce the same matching and absorbing properties for the transmitted waves.

From Fig. 4.2 it can be noticed that there are four corner regions that the UPML is not uniaxial in, because the corner regions are a superposition of different UPML layers. In this case, the expression of the tensor that multiplies the electric permittivity and magnetic permeability for this medium is given by

$$\overline{\overline{s}} = \begin{bmatrix} s_x^{-1} & 0 & 0 \\ 0 & s_x & 0 \\ 0 & 0 & s_x \end{bmatrix} \cdot \begin{bmatrix} s_y & 0 & 0 \\ 0 & s_y^{-1} & 0 \\ 0 & 0 & s_y \end{bmatrix} = \begin{bmatrix} s_x^{-1} s_y & 0 & 0 \\ 0 & s_x s_y^{-1} & 0 \\ 0 & 0 & s_x s_y \end{bmatrix} \tag{4.29}$$

with s_x and s_y defined as in equations (4.8) and (4.9).

4.4 Perfectly Matched Layer Parameters

The performance of the PML can be analysed by applying the transmission line concept upon the PML formulation [54]. The performance of the PML is affected primarily by the parameters that set the absorption rate of any impinging wave upon the PML, the electric and magnetic conductivity, σ and σ *, respectively. Each layer of PML is backed by a layer of PEC, the propagating wave is reflected of the PEC and back into the computational domain affecting the accuracy of the simulation. The reflection coefficient is

$$R(\theta) = e^{-2\sigma\eta\varepsilon_r d\cos(\theta)} \tag{4.30}$$

where θ is the angle of incidence, d is the width of the PML layer, η is the impedance, and σ is the electric conductivity of the PML layer. Eq. (4.30) shows that the reflection, R, from the PML exponentially decreases as the width and the conductivity increases. Increasing the width of the PML layer is not an option, as that would exhaust more computational resources. This means that the selection of the appropriate conductivity σ is of utmost importance to ensure low reflections in the PML. This leads to a trade-off between high values of electric and magnetic conductivities σ and σ^* inside the PML that provide good absorption, and between the accuracy of the results jeopardised by the high levels of discontinuity at the interface separating the computational domain and the PML layer that are caused by these high values of σ and σ *.

The work in [35] and [54] has overcome this problem by adopting a variation of the electric and magnetic conductivity profiles along the transverse direction. Such that, a geometrical scaling of the electric conductivity along the transverse direction x gives

$$\sigma(x) = \sigma_0 g^{x/\Delta x} \tag{4.31}$$

where σ_0 is the electric conductivity at the interface $x = 0$, g is the scaling factor, and Δx is the space discretisation. Applying this variation on Eq. (4.30) the reflection error becomes

$$R(\theta) = e^{-2\eta\sigma_0\Delta x\left(g^N-1\right)\cos(\theta)/\ln(g)} \tag{4.32}$$

where N is the number of cells of the PML layer. This leads to the value of the electric conductivity at $x = 0$

$$\sigma_0 = -\frac{\ln(R(0))\ln(g)}{2\eta\varepsilon_r\Delta x\left(g^N-1\right)} \tag{4.33}$$

Usually the maximum reflection error at normal incidence $R(0)$ and the scaling factor g are fixed and then the value σ_0 is computed. After that the scaling of the electric conductivity σ is performed inside the PML layer using Eq. (4.31).

4.5 PML Boundary Conditions for CE-ADI-FDTD

The work carried out in this thesis uses the CE-ADI-FDTD technique to simulate the photonic crystal devices. As such, the necessary mathematical derivations for the PML boundary conditions applied to the CE-ADI-FDTD method are shown here. These derivations are based on the work previously proposed in [2], [18], and [60] in the context of the ADI–FDTD algorithm. For TE_z polarisation, the 2D Maxwell's equations can be written as

$$\mu_0\mu_r \frac{\partial H_x}{\partial t} + \sigma^* H_x = -\frac{\partial E_z}{\partial y} \tag{4.34}$$

$$\mu_0\mu_r \frac{\partial H_y}{\partial t} + \sigma^* H_y = \frac{\partial E_z}{\partial x} \tag{4.35}$$

$$\varepsilon_0\varepsilon_r \frac{\partial E_z}{\partial t} + \sigma E_z = \frac{\partial H_y}{\partial x} - \frac{\partial H_x}{\partial y} \tag{4.36}$$

Applying the complex-envelope formulation on the above equations gives

$$\mu_0\mu_r \frac{\partial H_{xa}}{\partial t} + \left(\sigma^* + j\omega_c\mu_0\mu_r\right)H_{xa} = -\frac{\partial E_{za}}{\partial y} \tag{4.37}$$

$$\mu_0\mu_r \frac{\partial H_{ya}}{\partial t} + \left(\sigma^* + j\omega_c\mu_0\mu_r\right)H_{ya} = \frac{\partial E_{za}}{\partial x} \tag{4.38}$$

$$\varepsilon_0\varepsilon_r \frac{\partial E_{za}}{\partial t} + \left(\sigma + j\omega_c\varepsilon_0\varepsilon_r\right)E_{za} = \frac{\partial H_{ya}}{\partial x} - \frac{\partial H_{xa}}{\partial y} \tag{4.39}$$

After that, the PML formulation is applied on Eqs. (4.37 - 4.39) in which the envelope of the electric field E_{za} is split as follows

$$E_{za} = E_{zax} + E_{zay} \tag{4.40}$$

Substituting Eq. (4.40) in equations (4.37 - 4.39) gives

$$\mu_0\mu_r \frac{\partial H_{xa}}{\partial t} + \left(\sigma_y^* + j\omega_c\mu_0\mu_r\right)H_{xa} = -\frac{\partial E_{za}}{\partial y} \tag{4.41}$$

$$\mu_0\mu_r \frac{\partial H_{ya}}{\partial t} + \left(\sigma_x^* + j\omega_c\mu_0\mu_r\right)H_{ya} = \frac{\partial E_{za}}{\partial x} \tag{4.42}$$

$$\varepsilon_0\varepsilon_r \frac{\partial E_{zax}}{\partial t} + \left(\sigma_x + j\omega_c\varepsilon_0\varepsilon_r\right)E_{zax} = \frac{\partial H_{ya}}{\partial x} \tag{4.43}$$

$$\varepsilon_0\varepsilon_r \frac{\partial E_{zay}}{\partial t} + \left(\sigma_y + j\omega_c\varepsilon_0\varepsilon_r\right)E_{zay} = -\frac{\partial H_{xa}}{\partial y} \tag{4.44}$$

Then, the ADI-FDTD discretisation is applied to equations (4.41 - 4.44), and the 1st half time step reads as

$$H_{xa}\big|_{i,j+1/2}^{n+1/2} = \alpha_{xh}\big|_{i,j+1/2} H_{xa}\big|_{i,j+1/2}^{n} - \beta_{xh}\big|_{i,j+1/2}\left(E_{za}\big|_{i,j+1}^{n} - E_{za}\big|_{i,j}^{n}\right) \tag{4.45a}$$

$$H_{ya}\big|_{i+1/2,j}^{n+1/2} = \alpha_{yh}\big|_{i+1/2,j} H_{ya}\big|_{i+1/2,j}^{n} + \beta_{yh}\big|_{i+1/2,j}\left(E_{za}\big|_{i+1,j}^{n+1/2} - E_{za}\big|_{i,j}^{n+1/2}\right) \tag{4.45b}$$

$$E_{zxa}\big|_{i,j}^{n+1/2} = \alpha_{xe}\big|_{i,j} E_{zxa}\big|_{i,j}^{n} + \beta_{xe}\big|_{i,j}\left(H_{ya}\big|_{i+1/2,j}^{n+1/2} - H_{ya}\big|_{i-1/2,j}^{n+1/2}\right) \tag{4.45c}$$

$$E_{zya}\big|_{i,j}^{n+1/2} = \alpha_{ye}\big|_{i,j} E_{zya}\big|_{i,j}^{n} - \beta_{ye}\big|_{i,j}\left(H_{xa}\big|_{i,j+1/2}^{n} - H_{xa}\big|_{i,j-1/2}^{n}\right) \tag{4.45d}$$

Using forward or backward differencing approximation, as apposed to the conventional liner approximation, the coefficients of the PML equations can be found. This procedure means the field component on the left hand side of the equation and the field component on the right hand side of the equation can be collocated at the same time step. The coefficients for the 1st half time step become

$$\alpha_{xe}\big|_{i,j} = \frac{4 - j\omega_c\Delta t}{4 + \left(j\omega_c + 2\dfrac{\sigma_x}{\varepsilon_r\varepsilon_0}\right)\Delta t} \tag{4.46a}$$

$$\alpha_{xh}\big|_{i,j+1/2} = \frac{4 - \left(j\omega_c + 2\dfrac{\sigma_y^*}{\mu_r\mu_0}\right)\Delta t}{4 + j\omega_c\Delta t} \tag{4.46b}$$

$$\alpha_{ye}\big|_{i,j} = \frac{4 - \left(j\omega_c + 2\dfrac{\sigma_y}{\varepsilon_r\varepsilon_0}\right)\Delta t}{4 + j\omega_c\Delta t} \tag{4.46c}$$

$$\alpha_{yh}\big|_{i+1/2,j} = \frac{4 - j\omega_c\Delta t}{4 + \left(j\omega_c + 2\dfrac{\sigma_x^*}{\mu_r\mu_0}\right)\Delta t} \tag{4.46d}$$

$$\beta_{xe}\,|_{i,j} = \frac{2\Delta t}{\left(4 + \left(j\omega_c + 2\frac{\sigma_x}{\varepsilon_r\varepsilon_0}\right)\Delta t\right)\varepsilon_r\varepsilon_0 h_{xi}} \tag{4.46e}$$

$$\beta_{xh}\,|_{i,j+1/2} = \frac{2\Delta t}{(4 + j\omega_c\Delta t)\mu_r\mu_0\Delta y_j} \tag{4.46f}$$

$$\beta_{ye}\,|_{i,j} = \frac{2\Delta t}{(4 + j\omega_c\Delta t)\varepsilon_r\varepsilon_0 h_{yj}} \tag{4.46g}$$

$$\beta_{ye}\,|_{i,j} = \frac{2\Delta t}{(4 + j\omega_c\Delta t)\varepsilon_r\varepsilon_0 h_{yj}} \tag{4.46h}$$

Appling the same technique, the coefficients of the PML equations for the 2nd half time step become

$$\alpha_{xe}\,|_{i,j} = \frac{4 - \left(j\omega_c + 2\frac{\sigma_x}{\varepsilon_r\varepsilon_0}\right)\Delta t}{4 + j\omega_c\Delta t} \tag{4.47a}$$

$$\alpha_{xh}\,|_{i,j+1/2} = \frac{4 - j\omega\Delta t}{4 + \left(j\omega_c + 2\frac{\sigma_y^*}{\mu_r\mu_0}\right)_c\Delta t} \tag{4.47b}$$

$$\alpha_{ye}\,|_{i,j} = \frac{4 - j\omega_c\Delta t}{4 + \left(j\omega_c + 2\frac{\sigma_y}{\varepsilon_r\varepsilon_0}\right)\Delta t} \tag{4.47c}$$

$$\alpha_{yh}\,|_{i+1/2,j} = \frac{4 - \left(j\omega_c + 2\frac{\sigma_x^*}{\mu_r\mu_0}\right)\Delta t}{4 + j\omega_c\Delta t} \tag{4.47d}$$

$$\beta_{xe}\,|_{i,j} = \frac{2\Delta t}{(4 + j\omega_c\Delta t)\varepsilon_r\varepsilon_0 h_{xi}} \tag{4.47e}$$

$$\beta_{xh}\,|_{i,j+1/2} = \frac{2\Delta t}{\left(4 + \left(j\omega_c + 2\frac{\sigma_y^*}{\mu_r\mu_0}\right)\Delta t\right)\mu_r\mu_0\Delta y_j} \tag{4.47f}$$

$$\beta_{ye}\,|_{i,j} = \frac{2\Delta t}{\left(4 + \left(j\omega_c + 2\frac{\sigma_y}{\varepsilon_r\varepsilon_0}\right)\Delta t\right)\varepsilon_r\varepsilon_0 h_{yj}} \tag{4.47g}$$

$$\beta_{yh}\,|_{i+1/2,j} = \frac{2\Delta t}{(4 + j\omega_c\Delta t)\mu_r\mu_0\Delta x_i} \tag{4.47h}$$

The extensive work in [2] and [18] shows that this particular setup for the CE-ADI-FDTD equations with PML boundary condition has a stable algorithm for large Courant numbers, which is very beneficial for this work, as it substantially reduces the computer computational burden.

4.6 Newly Suggested PML Formulation

Lopez-Villegas and Vidal successfully presented in [61] an accurate physical model of discretisation error in one-dimensional PML using the FDTD method. The idea behind the model in [62] is based on the concept of the effective wave impedance of the PML. This concept implies that the wave impedance of the PML in the discretised space changes, with respect to the continuous value, when absorption takes place [61].

When considering normal losses in PML the absolute value of Direct Reflection Losses (DRL) is given by |DRL| = $e^{-2\alpha d}$, where d is the thickness and α is the attenuation per unit length, and can be expressed as $\alpha = (\sigma\sigma^*)^{0.5}$. Where σ is the electric conductivity (S/m) and σ^* (Ω/m) is the magnetic losses. When looking at this from an impedance matching point of view, then these parameters must satisfy the matching

condition $\sigma^*/\sigma = \eta_{PML}^2$ where η_{PML} is the PML wave impedance [61]. In the case of discretised FDTD space, the electric and magnetic fields are staggered by half the size of the unit cell (n) or discretisation step (Δx). Hence, the electric and magnetic field computational locations alternate every $\Delta x/2$ as illustrated in Fig. 4.3a. In a lossless medium the steady state values of the electric and magnetic field amplitudes do not change throughout the simulation domain as shown in Fig. 4.3b and the wave impedance is simply

$$\eta = \frac{|E_n|}{\left|H_{n+1/2}\right|} = \frac{|E_n|}{|H_n|} \tag{4.48}$$

where $|E_n|$ is the amplitude of the electric field at the electric node, while $|H_{n+1/2}|$ is the amplitude of the magnetic field at the magnetic node, and $|H_n|$ is the amplitude of the magnetic field at the electric node. Taking into account the exponential decay due to absorption in the PML medium, the magnetic field amplitude is underestimated in comparison to its electric counterpart as shown in Fig.4.3c and can be expressed as in Eq.4.49 [61].

$$|H_{n+1/2}| = |H_n| e^{-\alpha \Delta x/2} \tag{4.49}$$

Thus the concept of effective wave impedance of the PML, η^*_{PML} can be expressed as follows

$$\eta^*_{PML} = \frac{|E_n|}{\left|H_{n+1/2}\right|} = \frac{|E_n|}{|H_n|} e^{+\alpha \Delta x/2} = \eta_{PML} e^{+\alpha \Delta x/2} \tag{4.50}$$

Obviously in equations (4.49 - 4.50), when the wave propagates in the opposite direction, then the magnetic field amplitude becomes overestimated when comparing it with its electric counterpart, and thus the sign of the exponential changes.

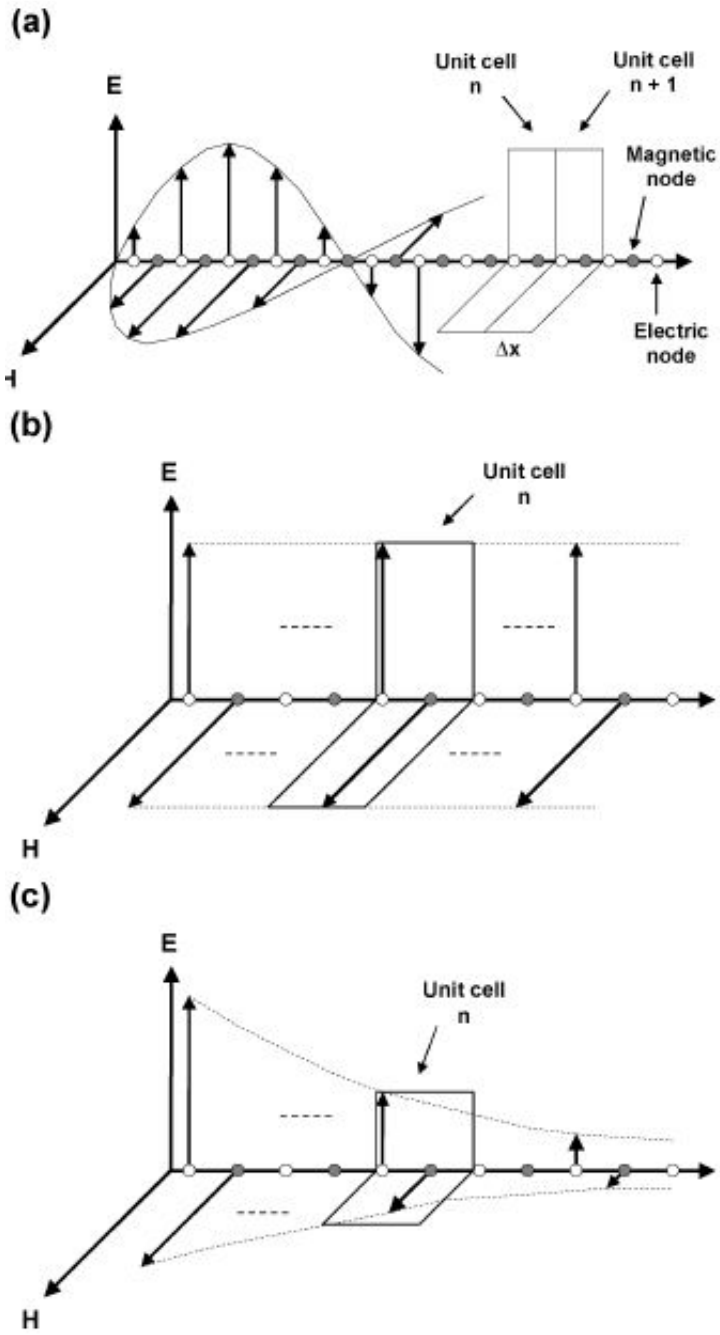

Figure 4.3 Spatial distribution of the electric and magnetic fields:

a) time dependent fields for a given time *t*.

b) steady state values of the field's amplitude in a lossless medium.

c) Steady state values of the field's amplitude in the 1D PML [61].

Hence from the above, the reflection coefficient of the PML resulting from impedance mismatching can accurately represent the Discretisation Error Losses (DEL)

$$DEL = \frac{\eta^*_{PML} - \eta}{\eta^*_{PML} + \eta} = \frac{e^{\pm\alpha\Delta x/2} - 1}{e^{\pm\alpha\Delta x/2} + 1} = \pm\tanh\left(\alpha\frac{\Delta x}{4}\right) \tag{4.51}$$

Eq. 4.51 successfully relates DEL with PML parameters and simulation conditions, α and Δx respectively. This brings us to the following relationship

$$\eta_{PML} = \eta e^{\mp\alpha\Delta x/2} \tag{4.52}$$

Thus from Eq. 4.50 effective impedance $\eta^*_{\mathrm{PML}}=\eta$ and using 4.51 DEL = 0 meaning a PML that is discretisation error free. The impedance shaping of 4.52 can be changed as follows

$$\eta_{PML} = \sqrt{\frac{\mu_{PML}}{\varepsilon_{PML}}};\begin{cases}\mu_{PML} = K\mu e^{\mp\alpha\Delta x/2}\\ \varepsilon_{PML} = K\varepsilon e^{\pm\alpha\Delta x/2}\end{cases} \tag{4.53}$$

where ε and μ are the electric permittivity and the magnetic permeability in the computational domain, while where $\varepsilon_{\mathrm{PML}}$and μ_{PML} are the electric permittivity and the magnetic permeability in the computational domain but change (are not constant) throughout the PML region. K is the scale factor, for K = 1 the propagation velocities in the computational domain and in the PML region are equal [61].

From the above derivations, it can be noticed that $\varepsilon_{\mathrm{PML}}$ and μ_{PML} are not constant throughout the PML, but change by a factor of exponential attenuation.

4.7 Summary

This chapter has presented an overview of the absorbing boundary conditions and PML, with a detailed look at PML boundary conditions, UPML absorbing boundary

conditions, and PML parameters. After that, the chapter explained the specific case of how to implement PML boundary conditions for CE-ADI-FDTD. Finally, the newly suggested PML formulation based on minimising discretisation error was presented.

In order to assess the performance of the suggested PML technique, an optical slab waveguide is presented in chapter 5 as an example for numerical assessment of the technique.

Chapter 5

Numerical Assessment of Newly Suggested Perfectly Matched Layer

5.1 Introduction

This chapter makes extensive use of the literature review covered in the previous chapters, by applying this review and suggested techniques in new designs and simulating these designs. The chapter presents the work accomplished in modelling and minimising the discretisation error of PML in optical slab waveguides using CE-ADI-FDTD. Also, the results of the simulations that study this design with the newly implemented techniques are presented.

5.2 Slab-Optical Waveguide: Example for Numerical Assessment

The idea behind this experiment was to implement the impedance matching theory used in microwaves and shown in chapter four on optical waveguides. The inset in Fig. 5.1 is a schematic representation of the slab or planar waveguide used for these simulations.

All numerical simulations have been carried out using self built MATLAB code and Microsoft Visual Studio C++. The geometry of the 2D planar waveguide in hand is as shown in Fig. 5.1 while the simulation parameters had a fixed discretisation in space of 0.1 μm and ten cells of PML layer are used to truncate the computational domain on all sides of the planar waveguide, providing the necessary environment of PML to study the discretisation error using the new model. The permittivity in vacuum $\varepsilon_o = 8.854 \times 10^{-12}$ F/m, and the permeability $\mu_o = 4\pi \times 10^{-7}$ H/m, while the effective index in the core $n_{core} = 2.5$ and in the cladding $n_{cladding} = 1.0$. Using the Courant criterion formula and the discretisation steps for x-direction and y-direction utilised for this simulation, the maximum time step that is possible to use $\Delta t_{CL} = 0.2358\ fs$. The source used to excite the domain is the mode profile, and the angular frequency ω_c of the source was fixed to 1.256 x 10^{15} rad/s ($\lambda = 1.5\ \mu m$). The electric permittivity ε_{PML} and the magnetic permeability μ_{PML} used in this system are as displayed in Fig. 5.1 and Fig. 5.2 below.

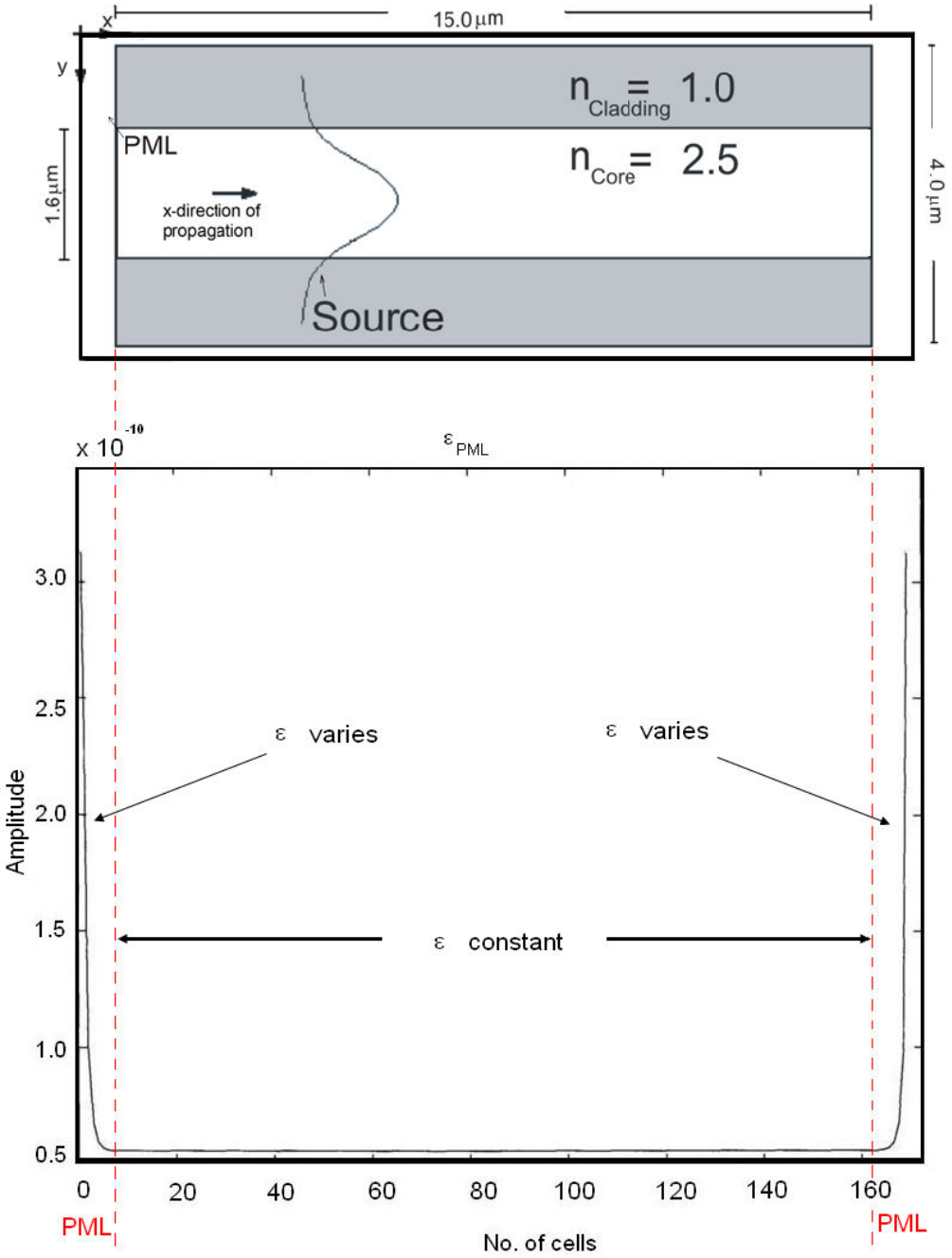

Figure 5.1 Permittivity in the computational region and PML region. Inset is the schematic diagram of the slab waveguide

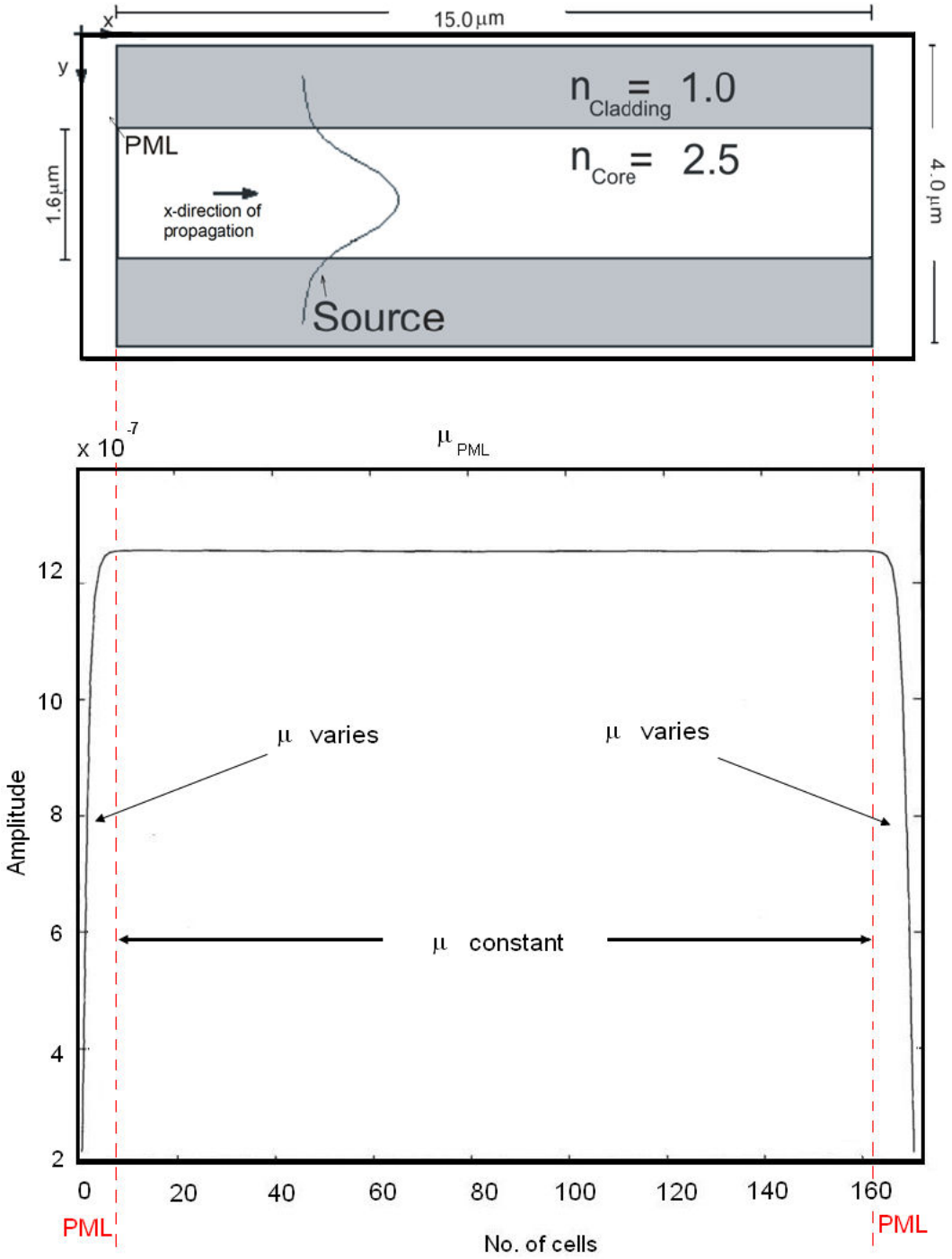

Figure 5.2 Permeability in the computational region and the PML region. Inset is the schematic diagram of the slab waveguide

The affect upon the electrical conductivity (in S/*m*) is as illustrated in Fig. 5.3

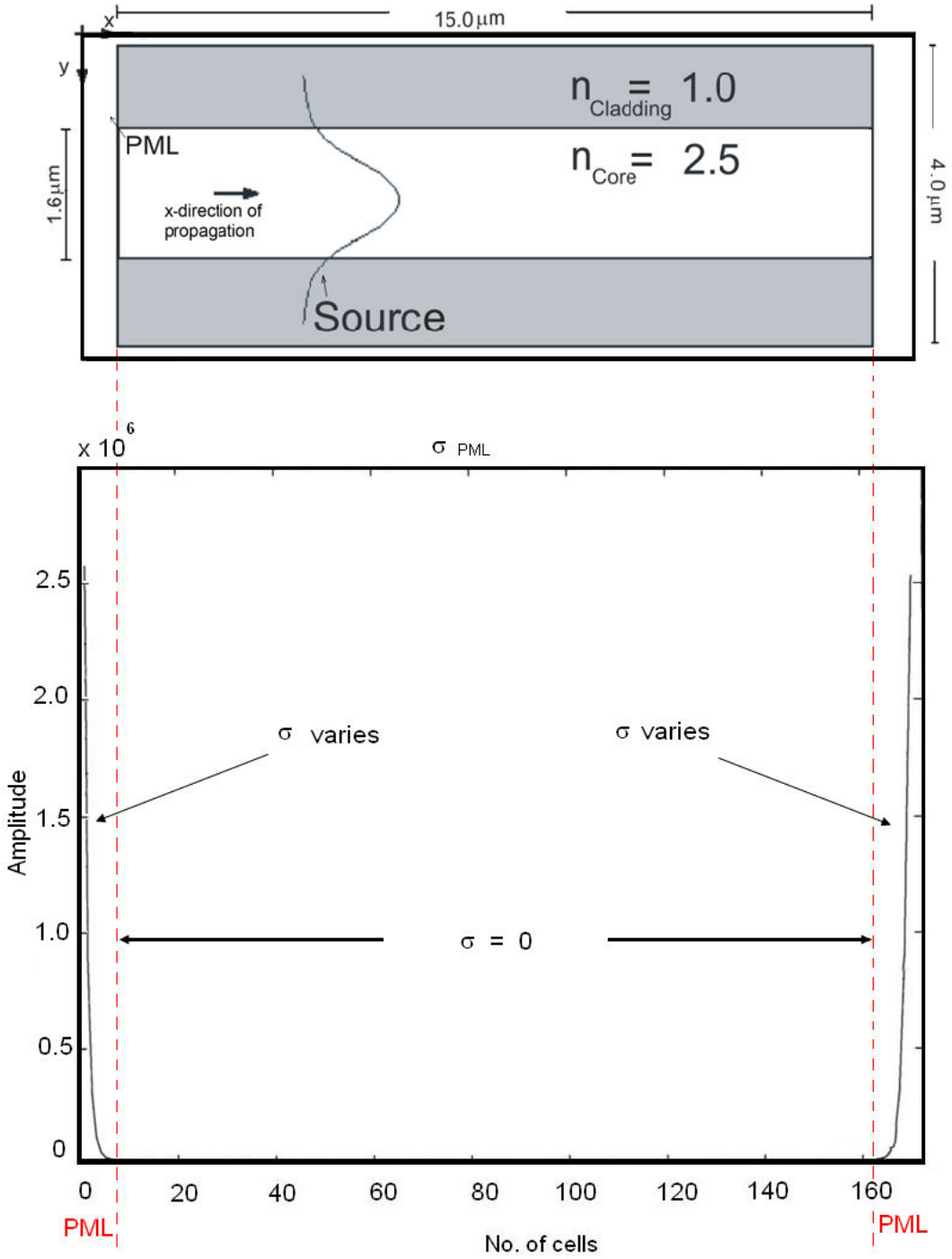

Figure 5.3 Electrical conductivity in the computational region and the PML region. Inset is the schematic diagram of the slab waveguide

The soft-source technique has been used to deploy the source in the

computational domain [2], [35], and [44]. The soft-source technique depends on adding the value of the source at each computational domain point to the value of the electric field at the same point; this is repeated for every time step. The effective index method was used to obtain the mode profile of this particular planar waveguide. In the TE modes for guided modes the formulae are

$$E_y = E_c \exp\left[-\gamma_c (x-h)\right], h < x \qquad \text{(cover)} \qquad (5.1)$$

$$E_y = E_f \cos\left(k_{fx} - \phi_s\right), 0 < x < h \qquad \text{(film)} \qquad (5.2)$$

$$E_y = E_s \exp\left(\gamma_s x\right), x < 0 \qquad \text{(substrate)} \qquad (5.3)$$

where h is the thickness of the core [62].

The results from the model based on the concept of effective wave impedance of the PML are presented. PML is affected mainly by the cell size and the absorption properties that potentially would considerably improve the reflection characteristics of the PML within optical range. In order to test the effectiveness of the newly implemented PML boundary conditions, a 15 × 4 μm planar waveguide structure, in the x- and y-directions, respectively, is simulated. The structure consists of dielectric core with refractive index $n_{\text{core}} = 2.5$ and air cladding. Ten cells of PML layer have been used to truncate the computational domain on all sides of the planar waveguide [35], as previously shown in the inset of Fig.5.1. First, the geometric grading parameters that affect the PML and matching impedance were varied and tested on the newly implemented PML. This was in order to investigate the effect these parameters — which include scaling factor g [35], scaling factor K [61], and the theoretical reflection error R_0 [53]— have on the overall performance of the newly modelled PML. Before looking at the effect of these parameters it should be noted here that the discretisation step was

fixed to 0.1 μm and the source was fixed to $1.256 \times 10^{15} rad/sec$ ($\lambda = 1.5\ \mu m$). The fundamental mode profile has been used to excite the waveguide. The time-step size was fixed to 3 times the Courant Limit. The time domain variation of the E-field was recorded using a line detector set at the centre of the core in the *y*-direction running along the direction of propagation, that is, the *x*-direction. The first parameter to be investigated is the theoretical reflection error R_0.

5.2.1 Investigating the theoretical reflection error R_0

The theoretical reflection error is varied for the purpose of investigating its effect upon the newly modelled PML, while fixing the scale factors $K = 1.00$ and $g = 2.00$. Fig.5.4 illustrates the investigated results.

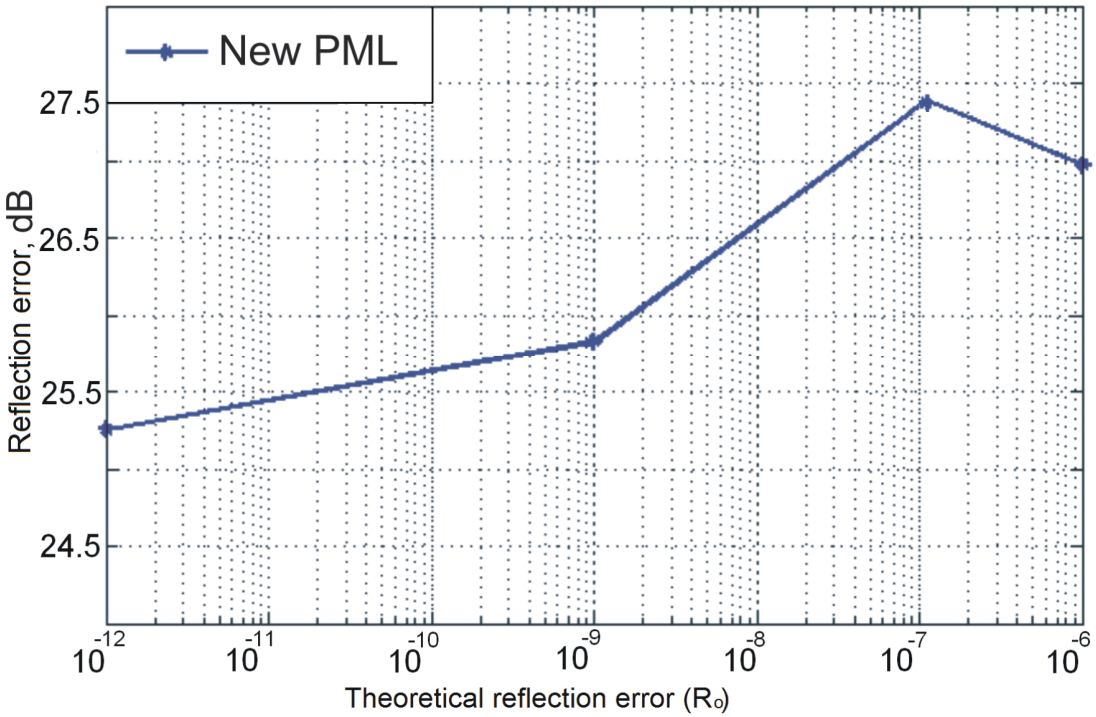

Figure 5.4 Effect of R_o theoretical reflection error on the newly modelled PML for $K = 1.0$, and $g = 2.0$

Fig. 5.4 shows that as the theoretical reflection error increases, the actual reflection error decreases. However, at $R_0 = e^{-16}$ the system reaches a peak, and then as the theoretical reflection error continues to increase beyond $R_0 = e^{-16}$ the actual reflection error in the system increases. Therefore, $R_0 = e^{-16}$ is found to be the optimum value for the newly implemented PML.

5.2.2 Investigating the metric scale factor g

The metric scale factor *g* parameter must be small to minimise the discretisation error by governing the rate of increase of the conductivity within the PML [35]. Again, the other parameters are all fixed at set values $R_0 = e^{-16}$, and $K = 1.00$ while *g* is varied to obtain the optimum effect on the PML. Fig.5.5 shows the results obtained when varying the scale factor *g* in the newly modelled PML.

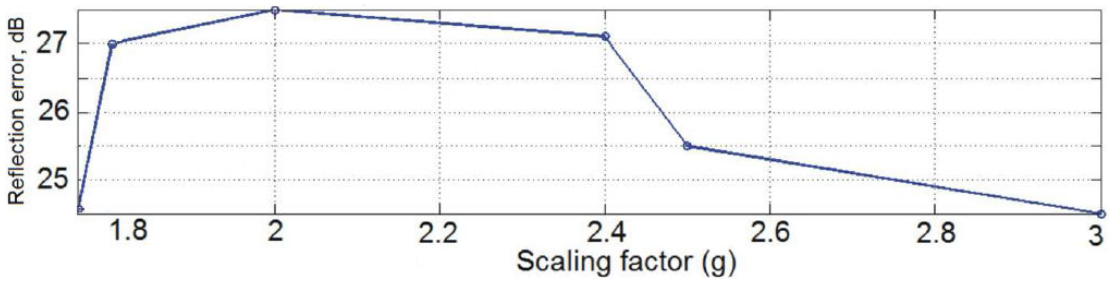

Figure 5.5 Effect of scale factor *g* on the New PML

Fig. 5.5 shows that as the scaling factor *g* increases, the actual reflection error decreases, however, at $g = 2.0$ the system reaches a peak, and then as the scaling factor *g* increases, the reflection error increases and thus the optimum performance is for $g = 2.00$.

5.2.3 Investigating the scale factor K

The scaling factor K represents the propagation velocity in the simulation space and in the PML. This investigation is done by fixing the theoretical reflection error to a set value of $R_0 = e^{-16}$, the scaling factor g = 2.00, and varying the scale factor K from its suggested value K = 1.00 [61].

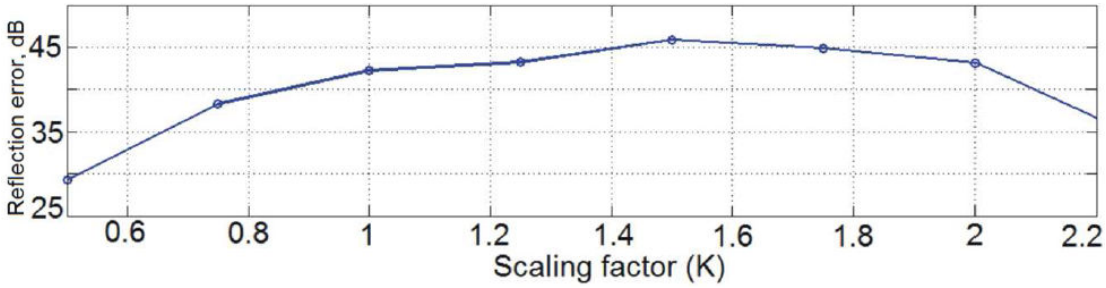

Figure 5.6 Effect of scale factor K on the New PML.

Fig. 5.6 shows that as the scaling factor K increases, the reflection error decreases, however, at K = 1.5 the system reaches a peak, and then as the scaling factor K increases, the reflection error increases and thus the optimum performance is for K = 1.5.

From observing figures 5.4 – 5.6 it is found that for $R_0 = e^{-16}$, g = 2.00, and K = 1.5 respectively, the newly modelled PML exhibits overall optimum performance.

5.2.4 Investigating the optimum number of PML cells

A study was carried out on the effect of increasing the number of PML cells. By using the optimum results obtained above, keeping all the parameters fixed and only varying the number of PML cells. The mode profile was used as the source of

excitation. The reflection coefficient was then measured for each case of varied number of PML cells. The study was performed by surrounding the computational domain with three different numbers of total PML cells, 10, 20 and 30. For each setting, a simulation was carried out which consisted in sending an electromagnetic pulse, centred at wavelength 1.5μm and with the fundamental mode profile of the slab waveguide, at the input section of the waveguide. A detector was inserted at the output section of the waveguide in order to store the time domain variation of the incident and reflected electric field. Using the FFT of both incident and reflected field, for each case the reflection coefficient was calculated and the results were recorder in Table 5.1 for the wavelength 1.5μm

Table 5.1 Effect of no. of PML cells on the reflection coefficient

No. Of Cells in PML	10	20	30
Reflection Coefficient	0.0005907	0.0003178	0.0002245

From Table 5.1, it can be clearly observed the excellent performance of the proposed PML formulation. For all three simulations the reflected field was always less than 0.06% of the incident field with a minimum of about 0.02% obtained using 30 PML cells. However, it has to be mentioned that the computational burden increases as the number of PML cells increases. Therefore, using 10 cells of PML is considered to be the best choice in terms of high absorption performance and low computational burden.

5.2.5 Comparing conventional PML and the newly suggested PML

Comparing the performance of the conventional PML and the newly implemented PML in terms of reflection coefficient Γ. The standing wave ratio results

were obtained using a continuous wave centered at a frequency $f_0 = 200 \times 10^{12}$ Hz, and the reflection coefficient from the incident waves reflected by the PML was extracted using the reflection coefficient formula as in Eq.5.4. The obtained reflection coefficient is illustrated in Fig. 5.7.

$$|\Gamma| = \frac{E_z^{\max} - E_z^{\min}}{E_z^{\max} + E_z^{\min}} \tag{5.4}$$

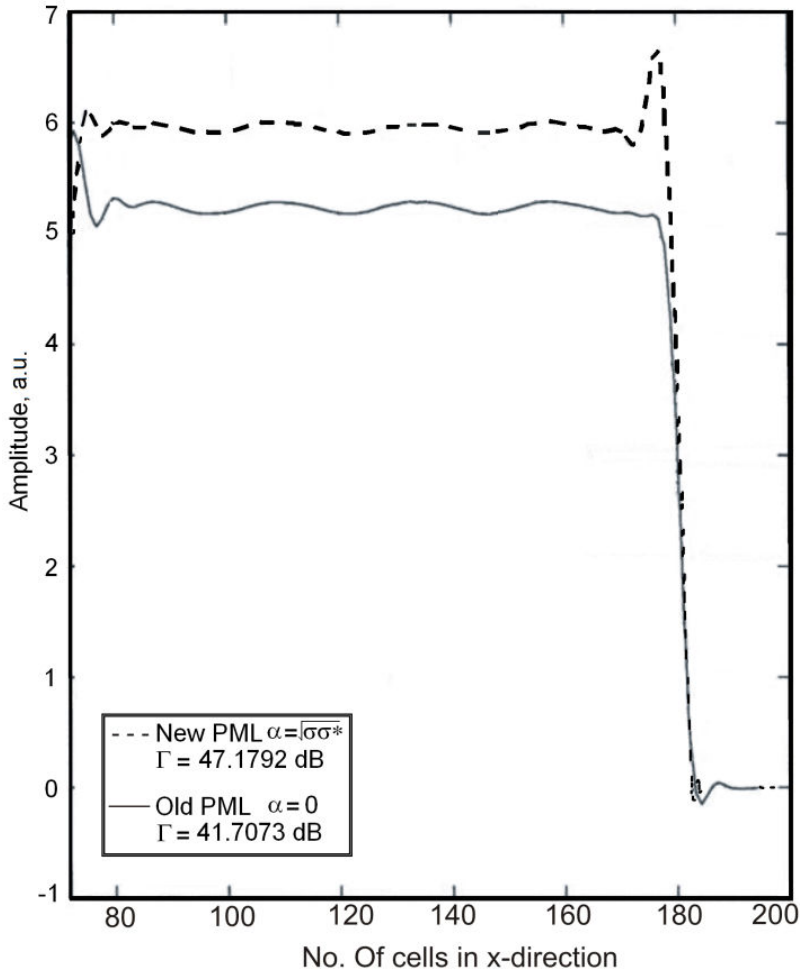

Figure 5.7 Standing wave of newly modelled PML vs. conventional PML

The standing wave pattern in Fig. 5.7 shows a considerable improvement of almost 6 dB in the value of E-field in favour of the newly implemented PML over the conventional PML. It should be noted here that from Eq. 4.53 it is clear with simple substitution of the value of α that the geometric grading of the PML loss parameters are reset to default for $\alpha = 0$.

5.3 Summary

This chapter has presented a detailed numerical assessment of the newly suggested PML that minimises discretisation error. The assessment was carried out on a slab-optical waveguide with emphasis on investigating the key factors affecting PML, theoretical reflection error, scaling factors, and the number of cells used for the PML structure. After that, a comparison was made between conventional PML and the newly suggested PML in terms of reflection coefficient. It was found that the newly suggested PML outperforms the conventional PML by several dB.

Since the newly suggested PML has been assessed on optical waveguides, it will be used in the design and analysis of the photonic crystal switches in the following chapters, where in chapter 6 MUX/DEMUX photonic crystals devices are presented, and in chapter 7 THz photonic crystal ring resonators are investigated.

Chapter 6

Photonic Crystal Based Multiplexer - Demultiplexer

6.1 Introduction

Having established the effectiveness in terms of absorptions of the proposed PML scheme, this PML scheme is then used in conjunction with the CE-ADI-FDTD method for the analysis of a new design of PhC based MUX/DEMUX. This chapter presents the main principles of MUX/DEMUX design, then three MUX/DEMUX optical switches are presented and their performance is investigated.

6.2 Multiplexer / Demultiplexer: Implementation and Design Principles

In optical communications, the optical fibre has huge bandwidth, which, unless utilised correctly, would be wasted on a single channel being sent across the fibre. This is where multiplexers and demultiplexers are useful. The technology is based on separating the light in the optical fibre into distinctive channels according to the colour of light, in other words, distinctive wavelength channels. The idea is that every channel transmits the same amount of data as a single fibre that has not been multiplexed.

The basic idea of the MUX/DEMUX can be illustrated by Fig.6.1. The innovation of this PhC based MUX/DEMUX design resides in the exploitation of the coupling length concept which is used for the separation of different signals in different channels.

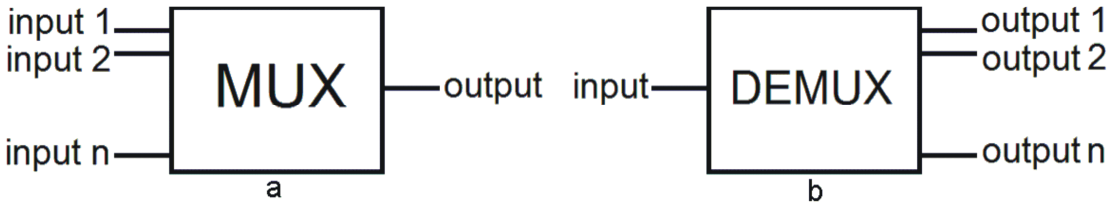

Figure 6.1 a) schematic of a multiplexer with several input signals and one output signal, b) schematic of a demultiplexer with a single input carrying several channels, and several output lines.

Within an optical communication system there is a transmitter and receiver, multiplexer and demultiplexer, respectively. The transmitter takes several signals and sends them across a single channel, while the receiver separates these signals into distinctive channels. Ideally, such a system would have a switching device that

simultaneously transmits and receives signals.

The main advantage of the multiplexing technique in telecommunication is that it allows the capacity of the network to be increased without the need of changing the backbone of the fibre network. This is made possible through implementing switching devices and deploying optical amplifiers throughout the optical network. This capacity increase is achieved by upgrading the transmitters and receivers of the network, thereby allowing for many generations of technological advancement in the optical infrastructure without laying more fibre.

The optical spectrum is divided into several distinct wavelengths that do not overlap, and each wavelength corresponds to a single communication channel. Thus, providing several multiplexing channels on the same fibre, and greatly utilising the fibre's huge bandwidth.

6.3 2 × 1 MUX/DEMUX: Design Principles

6.3.1 Setup

The idea here is to design a 2 × 1 MUXDEMUX that operates according to the coupling length of the wave travelling across the photonic crystal waveguide. Therefore, an investigation is carried out on the coupling length of a particular wave in a specific PhC device. In order to achieve this, a PhC structure is designed based on the PhC lattice geometry used in [30].

The structure is selected to enable direct comparison between the design results in this paper and those in [30]. Also the PBG range includes wavelengths of particular interest such as $\lambda = 1.55\ \mu m$. Thus, the PhC structure consists of dielectric rods arranged

in a triangular lattice with lattice constant a = 0.601 μm, radius r = 0.2a, and with refractive index n = 3.464 in air (n = 1) is considered. In the proposed structure the length of the rods is considered to be long enough that the light will be reasonably confined to the transversal plane and losses will be minimal.

In this structure two adjacent waveguides have been created removing two rows of rods separated by a single row of rods, as shown in the inset of Fig.6.2.

6.3.2 Coupling length and cavity length

If a signal is inserted in one of the two waveguides it couples with the other one after propagating for a fixed distance. The length the wave travels within the waveguide before coupling is known as the coupling length L, measured here per number of rods.

A series of simulations were carried out on the range of normalised frequency $0.290 < a / \lambda < 0.479$ and the corresponding coupling length of each wavelength was determined, with the range of interest plotted in Fig. 6.2.

In order to do so, a source with Gaussian profile in space expressed below, was used such that each simulation was fixed to a particular wavelength.

$$E_{za}(x, y) = e^{-(\frac{x-x_o}{X_0})^2} e^{-(\frac{y-y_o}{Y_0})^2} \tag{6.1}$$

where x_0 and X_0 are the displacement and the width of the Gaussian pulse along x-direction, respectively, and y_0 and Y_0 are the displacement and the width of the Gaussian pulse along y-direction, respectively. For all simulations, x_0 was set at the input port of the input waveguide, while y_0 was set to the coordinates of the centre of the input waveguide, X_0 and Y_0 were fixed to a / 6.

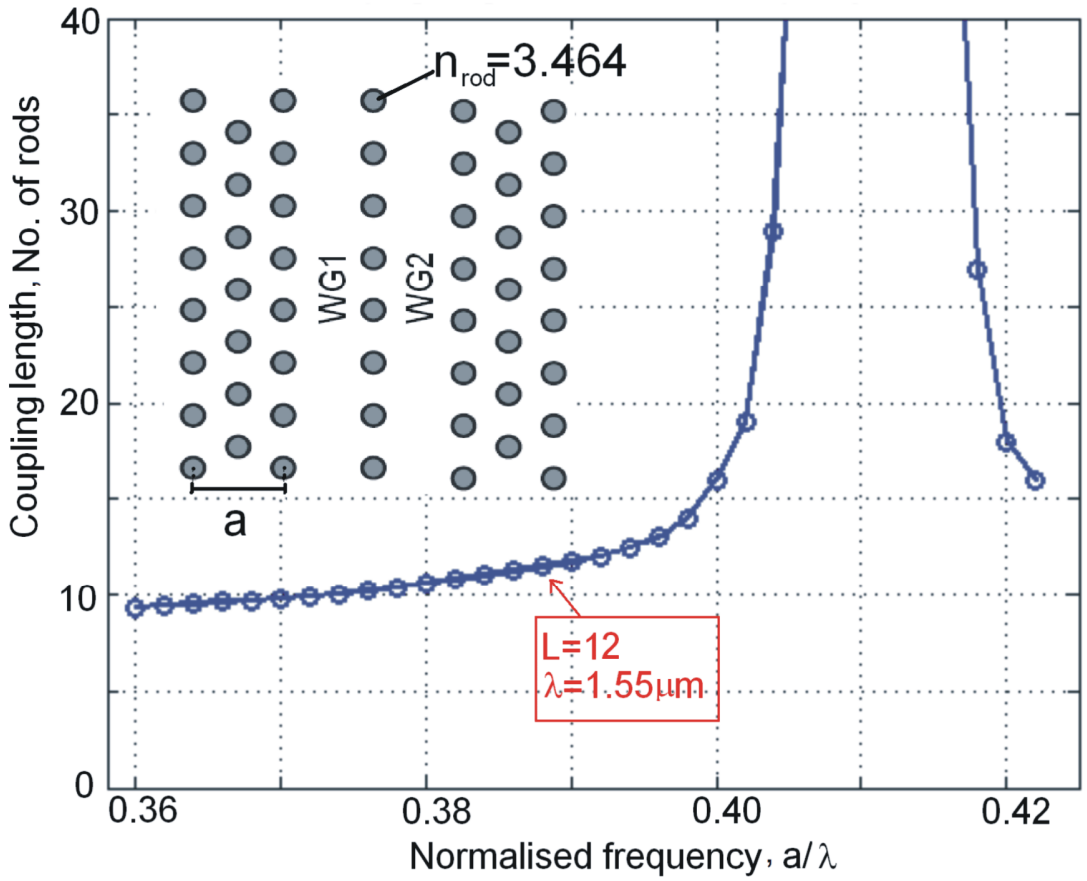

Figure 6.2 Coupling length vs. normalised frequency.

It can be observed from Fig.6.2 that the value of the coupling length L increases to infinity at the normalised frequency $f_{norm} = 0.41 = a / \lambda$, which implies that the optical wave at this frequency propagates without crossing into the adjacent waveguide. In order to filter or control the frequencies at the output of WG2 a cavity is inserted. Exploiting the concept of the coupling length when designing the MUX/DEMUX, the wave propagation and coupling between waveguides can be engineered and specific frequencies can be selected to couple to the output waveguide. This is achieved by inserting a total of three rows of separating rods between WG1 and WG2, with a cavity embedded in the middle row of separating rods. It should be noted that the cavity is

carefully geometrically designed such that the length of the cavity along the direction of propagation is equal to the coupling length for the selected wavelength (λ = 1.55 μm). The schematics of the PhC 2 × 1 MUX/DEMUX with a single cavity is illustrated in Fig.6.3.

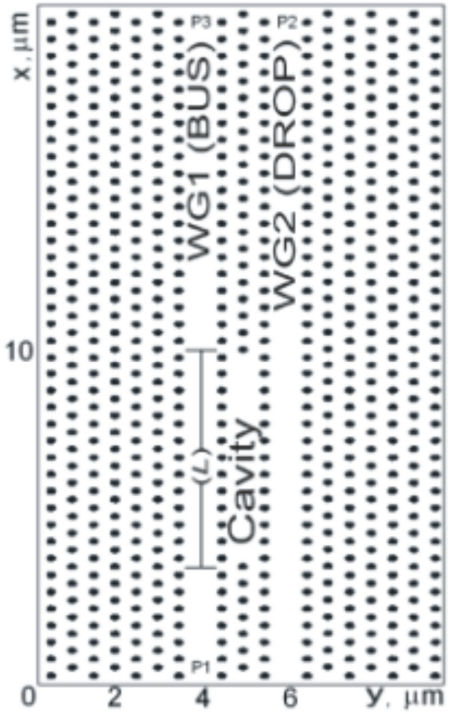

Figure 6.3 Schematic diagram of the MUX/DEMUX with a rectangular cavity embedded within three rows of rods separating the two waveguides.

6.3.3 Cavity study

In order to investigate the operation of the cavity and its selectivity for L = 12, the cavity was individually isolated, and a Gaussian shape profile was placed in the center of the cavity and modulated by a Gaussian pulse in time. This Gaussian pulse in time covered the entire range of frequencies in the device's PBG. Line detectors were used in order to record the time domain variation of the EM field. The FFT was used to

monitor the modes propagating in the simulated structure. The Gaussian pulse was centered at $\lambda = 1.55\ \mu m$ for the large cavity. Fig. 6.4 shows the spectrum of the resonant modes in the cavity.

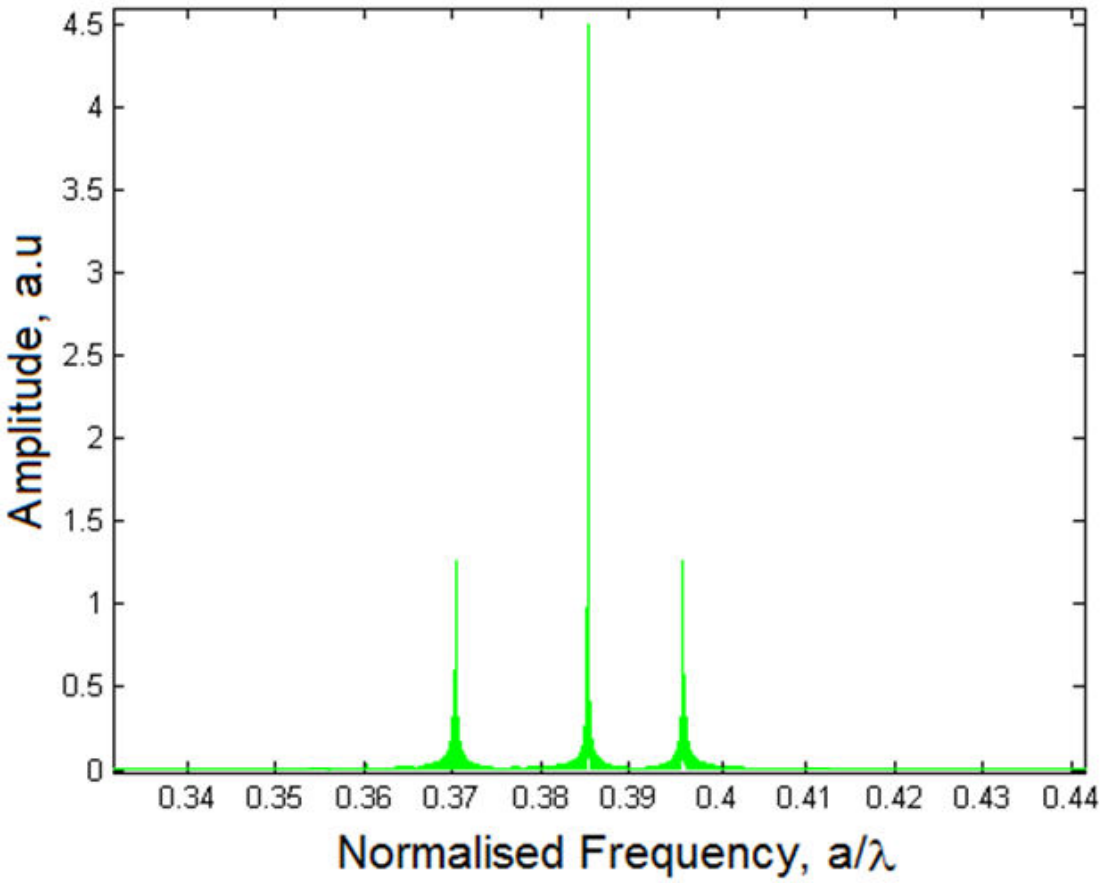

Figure 6.4 Light spectrum in cavity with the length $L = 12$, for a pulse centered at $\lambda = 1.55\ \mu m$

The results illustrated in Fig. 6.4 show the robustness and reliability of the design at $\lambda_1 = 1.55\ \mu m$ for $L = 12$, as well as the strong feature of wavelength selectivity, as the modes are distinctive and can be easily isolated. Compared to point defect cavities, cavities tailored to the coupling length offer optimum performance at required frequencies, and flexibility in mode design due to their multi mode nature.

6.3.4 Cavity effect in switching devices

To demonstrate the effect of the cavity upon the PhC structure three tests were carried out with different conditions and bearing different results. All simulations were set to a total of 7000 time steps, with the time step size fixed to 3 time the Courant limit for a total of t = 2476.586 *fs* time simulated. Also, all simulations had line detectors strategically inserted on the waveguides in order to store the time domain variation of the electromagnetic field.

In the first of the three tests a Gaussian shaped profile in space modulated by continuous wave source in time with wavelength fixed to λ = 1.55 μm as described in (6.1) above, was used to excite the structure in the inset of Fig.6.2. The signal propagated in the structure such that the wave coupled back and forth between the two waveguides, WG1 and WG2 as illustrated in the snapshot of Fig.6.5.a. Next, the same source was used a second time to excite the PhC structure in Fig.6.3, which contains the embedded cavity, with cavity length L = 12, designed to select that particular wavelength, λ = 1.55 μm. The signal propagated in the structure such that the wave coupled into the adjacent output waveguide, WG2 as illustrated in the snapshot of Fig.6.5.b. Then, a Gaussian shaped profile placed at the input of WG1 modulated by a continuous wave source in time with wavelength fixed to λ = 1.48 μm as described in (6.1) above, was used to excite the PhC structure in Fig.6.3, which contains the embedded cavity, L = 12 designed to select a wavelength λ = 1.55 μm. As expected, the signal propagated in the structure such that the wave did not couple into the adjacent output waveguide, but in fact propagated only along the input waveguide WG1 as illustrated in the snapshot of Fig.6.5.c.

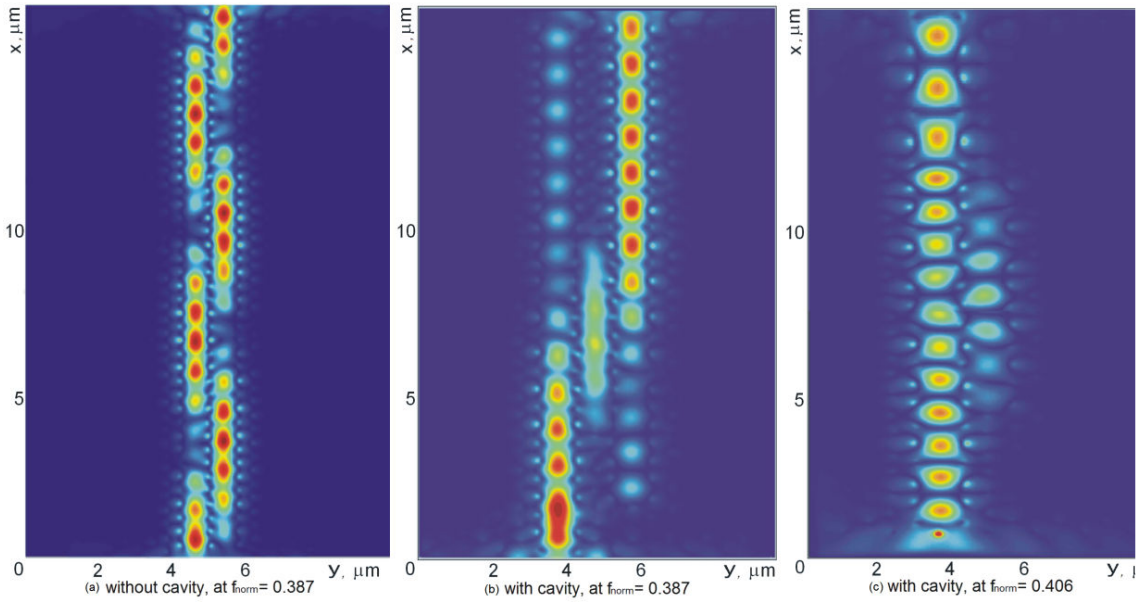

Figure 6.5 a) Selected frequency (f_{norm} = 0.387) propagates in both waveguides WG1 and WG2, b) selected frequency (f_{norm} = 0.387) propagates in only in waveguide 2, c) other frequencies, (f_{norm} = 0.406) only propagate in waveguide 1.

6.3.5 2 × 1 MUX/DEMUX performance: single cavity

The Cavity Length (CL), as mentioned above, was carefully selected to be equal to the coupling length, L = 12 rods. In order to verify the setting CL = L as optimum, simulations similar to that used to extract the propagating wavelengths with the inserted cavity were carried out varying only the number of rods removed inside the cavity. Fig.6.6 shows the transmission of the signal at the output port in WG2 with respect to varying the number of rods in the embedded cavity

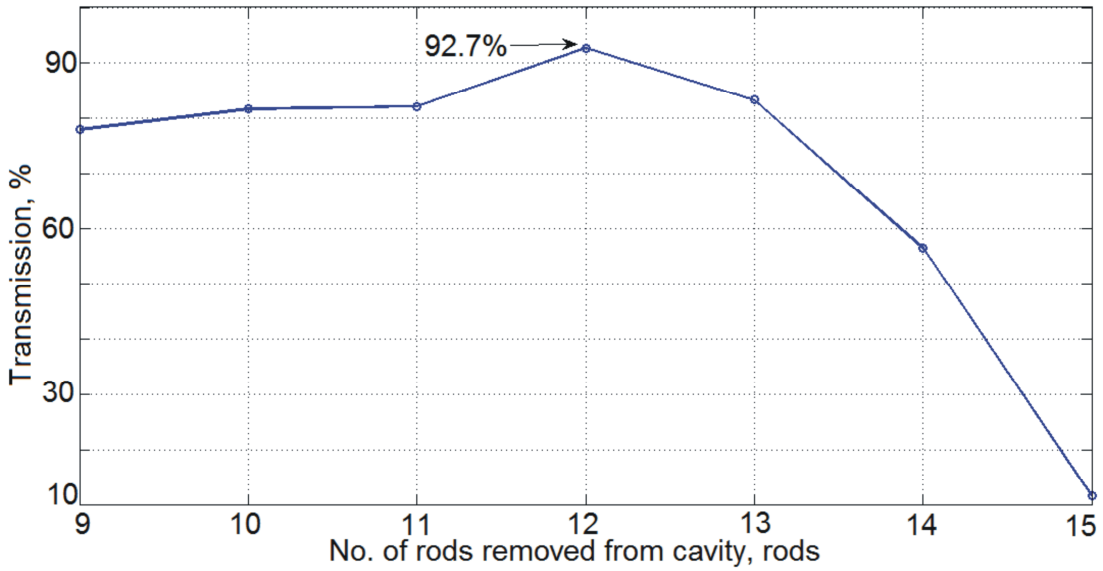

Figure 6.6 Cavity length selection

In order to achieve this, the time domain data, through the use of FFT, were used for the calculation of the transmission rates of the simulated structures which were computed as the power ratio between the input power P1 inserted in waveguide 1 and output power P2 extracted from waveguide 2. The results of this procedure are measured by the transmission of the signal at the output port. The transmission from Fig.6.3 can be expressed as

$$Transmission = \frac{P2}{P1} \tag{6.2}$$

where P2 is the output in WG2, and P1 is the input in WG1. The crosstalk, which is the power ratio between output ports WG2 : WG1, can be expressed as

$$crosstalk = \frac{P2}{P3} \tag{6.3}$$

where P1 is the input in WG1. The high performance in terms of crosstalk

(crosstalk = 22.07dB) is seen also in the transmission rate which is calculated to be 92.7%. The excellent performance in terms of crosstalk and transmission rate of the proposed structure shows to be very competitive when compared with other designs suggested in literature [30] where a MUX/DEMUX structure is designed as shown in Fig.6.7.

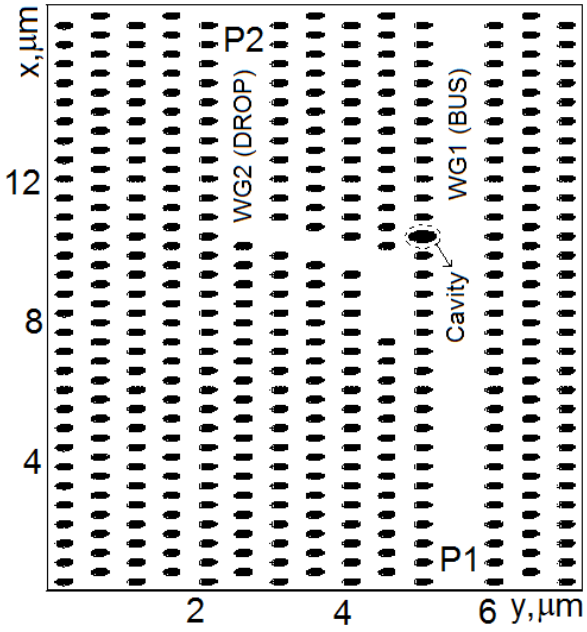

Figure 6.7 Schematic structure in [30]

The main drawback of the proposed design is that there are only three rows of rods separating WG1 and WG2 which means that there is still the potential for direct coupling to exist between the two waveguides.

6.3.6 Dual cavity

To overcome this shortcoming an additional two rows of rods of radius *r* are added to separate waveguide 1 and waveguide 2, bringing the total amount of separation to a total of five rows of rods while the embedded cavity is still at the same place as the

previous design. However, with the extra rows of rods added between the cavity and waveguide 2 the percentage of transmission is easily predicted to fall rapidly. In order to circumvent this drawback, another identical cavity is carefully placed adjacent to the first one with a single row of rods separating them. The addition of a second cavity, C2, is believed to improve the coupling between the two waveguides increasing the overall performance of the designed structure. Nevertheless, an additional study on the position of this second cavity with respect to the first has been conducted in order to investigate the effect of the second cavity position on the performance of the structure in terms of crosstalk. Simulations have been done for different positions of the second cavity. The results demonstrate that the configuration illustrated in Fig.6.8 presents the best performance with a crosstalk calculated to be equal to 15.75 dB.

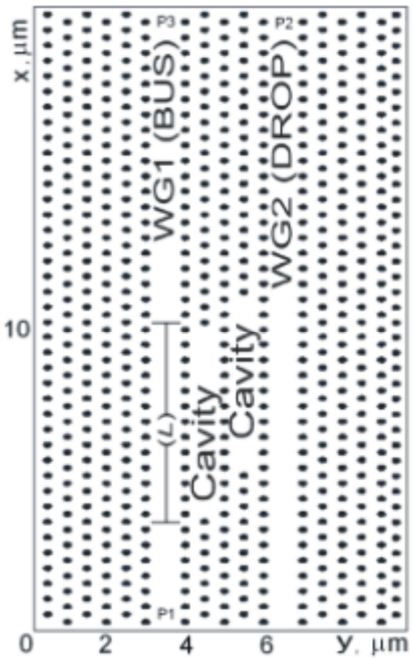

Figure 6.8 Schematic design of the two rectangular cavity PhC MUX/DEMUX.

In Fig.6.9, a snapshot of the propagating electromagnetic field in steady state

regime is shown from which the coupling between waveguide 1 and waveguide 2 can be clearly seen. Although this design ensures minimum direct coupling between the two waveguides, which implies a more reliable and far more robust design, its performance in terms of a transmission of 85.97% between waveguide 1 and waveguide 2 is not as impressive as its single cavity counterpart.

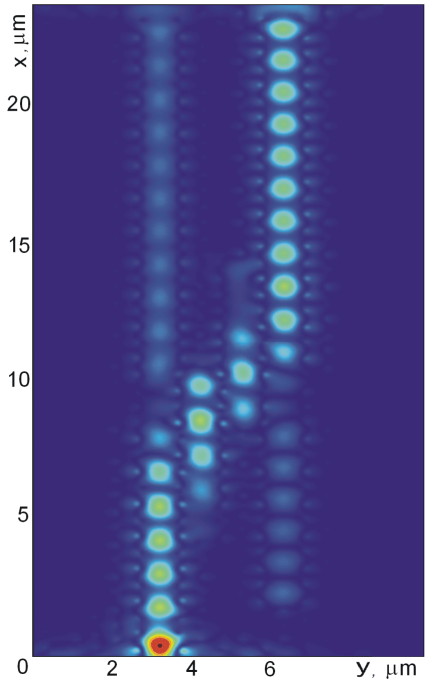

Figure 6.9 PhC MUX/DEMUX electric field propagation with two rectangular cavities.

6.3.7 Improving the cavity coupling

Different solutions can be implemented in order to improve the coupling between the two waveguides. In [30] and [64] dielectric rods with different refractive index have been used in order to improve trapping photons and controlling the lightwave. However, this solution requires the use of a different dielectric material which can be quite difficult to realise practically.

A different approach for increasing the coupling between the two waveguides is

proposed here. For the optimisation of the structure, all the rods adjacent to the first cavity were replaced by rods with larger radii with respect to the rods of the unperturbed PhC structure, ranging from r_d = 0.202a to 0.230a. This range of radii has been considered in order to not significantly modify the band structure of the PhC. The results of this investigation are summarised in Fig.6.10. Changing the radius of the rods around the cavity enhances the tuning capabilities of the PhC structure.

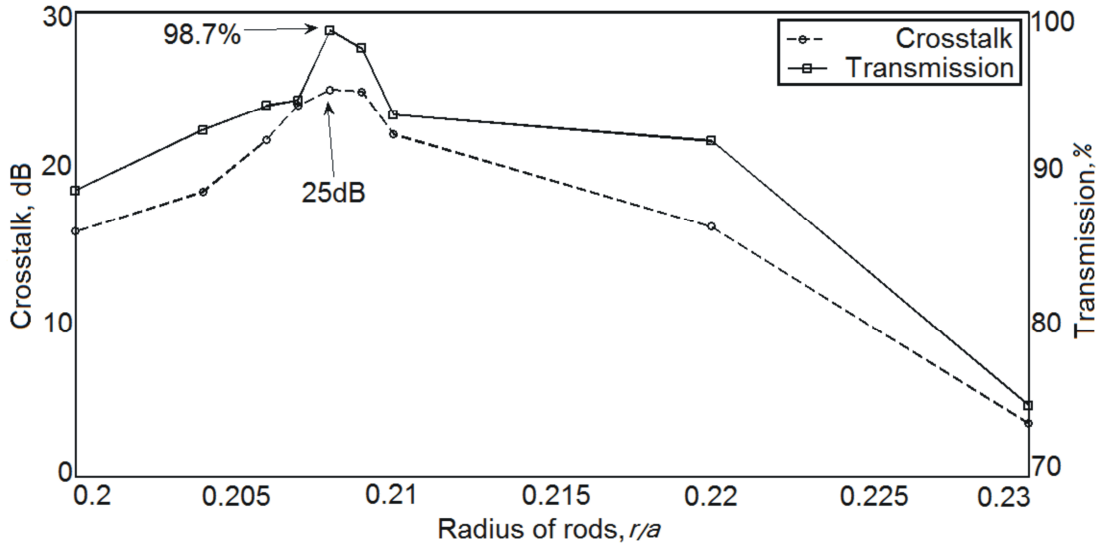

Figure 6.10 Crosstalk and transmission vs. radius of rods ($r = a$)

The results of this case study presented in Fig. 6.10 clearly indicate that there is a peak at which the PhC structure reaches its optimum levels of crosstalk and transmission rate. The peak occurs at r_d = 0.208a with crosstalk calculated to be 25dB, and a transmission of 98.7%.

6.3.8 Second cavity optimisation

In order to show that the new size of the rods does not impact the performances obtained from the optimisation process of the position of second the cavity, a similar

case study is performed with the new cavity. It should be noted here that the placement cases of the adjacent cavity ranged from placement 0 to placement 9, where placement 0 represents Cavity 1 (C1) and Cavity 2 (C2) in perfect alignment, while placement 1 has C2 shifted by one rod in the direction of propagation (*x*-direction), and so forth until placement 9, as schematically shown in the inset of Fig.6.11.

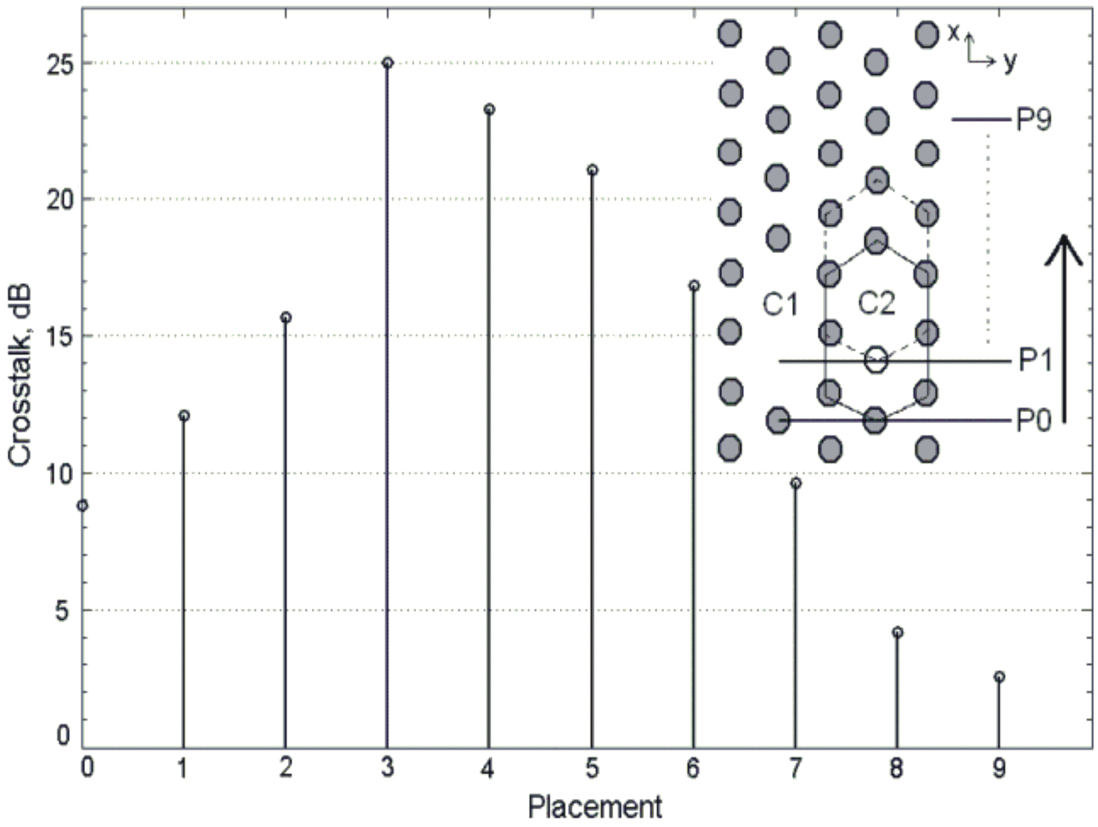

Figure 6.11 Crosstalk vs. Placement of cavity 2, inset, schematic structure of placing cavity 2

The results summarised in Fig.6.11 clearly show that the position of the second cavity obtained from the previous optimisation process is the optimum one and any other setup results in the degradation of the overall performances of the proposed structure in term of crosstalk and transmission rate.

The results of this design compare favourably with the results obtained using other designs, such as the MUX/DEMUX in [30] as shown in Fig.6.7. At $\lambda = 1.55\ \mu m$, transmission = 97.4% in [30], while as shown above, the transmission using this new design is 98.7%.

6.4 3 × 1 MUX/DEMUX: Principle of Design

In this section, a 3 × 1 MUX/DEMUX PhC based structure is presented. This is achieved by carefully following the design method described in the sections above. This is by carefully considering the coupling length of the propagating wave and accurately engineering the geometrical design of the microcavities. The design is highly selective, such that, a microcavity embedded between two waveguides selects a particular wavelength to couple from one waveguide into an adjacent waveguide. The difference between this design and the designs mentioned in the previous sections of this chapter is the fact that this design enables more than one wavelength to be coupled to its appropriate output port. The numerical technique used for the designs throughout this design is again the CE-ADI-FDTD.

The suggested 3 × 1 PhC MUX/DEMUX design with the appropriate coupling length and embedded microcavities have been simulated in order to assess the effectiveness of the wavelength selectivity of the device. This simulated design uses the concept of the coupling length [65]. Coupling, which is the mutual interaction of the propagating light wave between two or more defects, occurs here between the central waveguide and the adjacent waveguides via the imbedded cavities. These embedded cavities have been carefully placed with respect to the coupling length of the particular wavelength of interest. This coupling length is the length at which the propagating light

wave moves from one waveguide to the adjacent waveguide.

The MUX/DEMUX is based on a PhC structure consisting of dielectric rods arranged by a triangular lattice with lattice constant a = 0.601 μm, radius r = 0.2 a, with refractive index n = 3.464, in air (n = 1). The PBG ranges from the normalised frequency units 0.290 to 0.479 [30].

In this structure three adjacent waveguides have been created by removing three rows of rods. Each waveguide is separated from the adjacent waveguide(s) by five rows of rods. Four cavities are placed such that two cavities are within each block of five rows of rods separating any two adjacent waveguides as in Fig.6.12

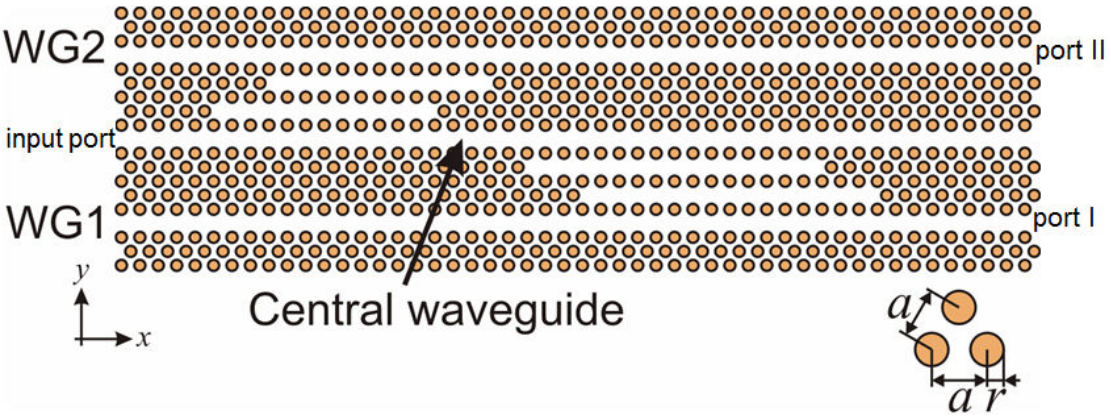

Figure 6.12 Schematic design of 3 × 1 PhC MUX/DEMUX

As illustrated in Fig.6.12, there is a central waveguide with two adjacent waveguides, one on each side of the central waveguide. On the bottom there is WG1 and on the top there is WG2. The selectivity of each waveguide depends on the cavities placed between any two waveguides. The cavities are carefully designed such that the cavities adjacent to WG1 are optimised for a particular frequency to couple from the input of the central waveguide to the output of WG1. These cavities are tuned to a

coupling length L = 16 rods, which is optimum for a wavelength of λ = 1.417 μm. The second block of cavities placed adjacent to WG2 are particularly tuned to a coupling length L = 12 rods, which corresponds to a wavelength λ = 1.55 μm.

6.4.1 Large cavity characteristics

In order to investigate the operation of the cavity and its selectivity, the large cavity, L = 16 was individually isolated, and a Gaussian shape profile was placed in the center of the cavity and modulated by a Gaussian pulse in time. This Gaussian pulse in time covered the entire range of frequencies in the device's PBG. Line detectors were used in order to record the time domain variation of the EM field. The FFT was used to monitor the modes propagating in the simulated structure. The Gaussian pulse was centered at λ_1 = 1.417 μm for the large cavity. The second cavity, L = 12 has the same characteristics as mentioned in the 2 × 1 MUX/DEMUX. Fig. 6.13 shows the spectrum of the resonant modes in the large cavity. That is, the results illustrated in Fig.6.13 show the robustness and reliability of the design at λ_1 = 1.417 μm for the large cavity, as well as the strong feature of wavelength selectivity, as the modes are distinctive and can be easily isolated.

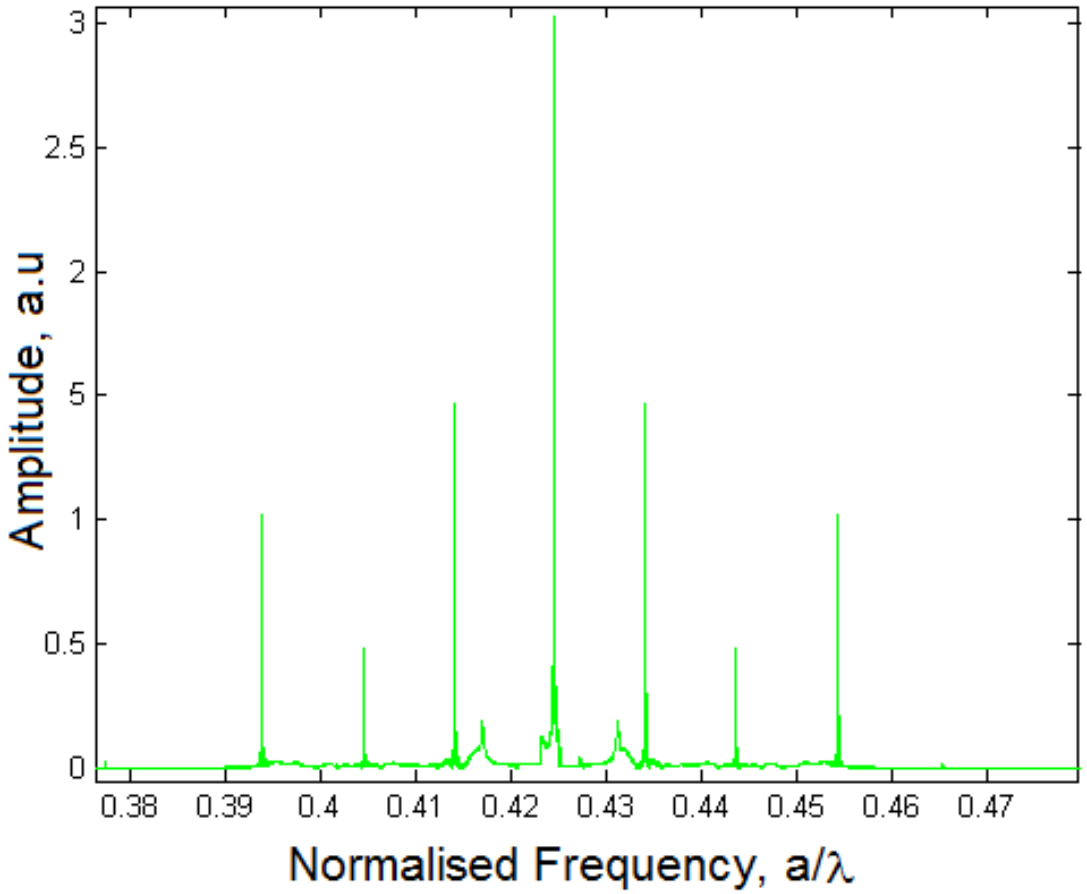

Figure 6.13 Light spectrum in cavity with the length L = 16, for a pulse centered at λ_1 = 1.417 μm

6.4.2 Transmission characteristics

After studying the cavities in isolation, the entire 3 × 1 MUX/DEMUX structure was further investigated. The source used to excite the structure was a Gaussian shaped profile placed at the input of the central waveguide modulated by a continuous wave source in time with wavelength fixed to λ_1 = 1.417 μm for the first simulation and λ_2 = 1.550 μm for the second simulation. Each simulation used a total of 7000 time steps with a time step size fixed to 3 times the Courant Limit. Line detectors were inserted on all waveguides in order to record the time domain variation of the EM field. The FFT was

used to extract the necessary information from the time domain data in order to calculate the crosstalk and selectivity of the simulated structure. As a result of this procedure, the performance of this 3 × 1 MUX/DEMUX exhibits an excellent crosstalk of 14 dB difference between the output at WG1 and the output at WG2.

In Fig.6.14 and Fig.6.15 a snapshot of the propagating EM field in steady state region is shown for wavelength λ_1 = 1.417 μm and λ_2 = 1.55 μm, respectively. From the figures, the very good performance of the proposed device is clearly shown as most of the signal inserted in the central waveguide is completely coupled to its associated output waveguide; λ_1 = 1.417 μm couples to WG1, and λ_2 = 1.55 μm couples to WG2.

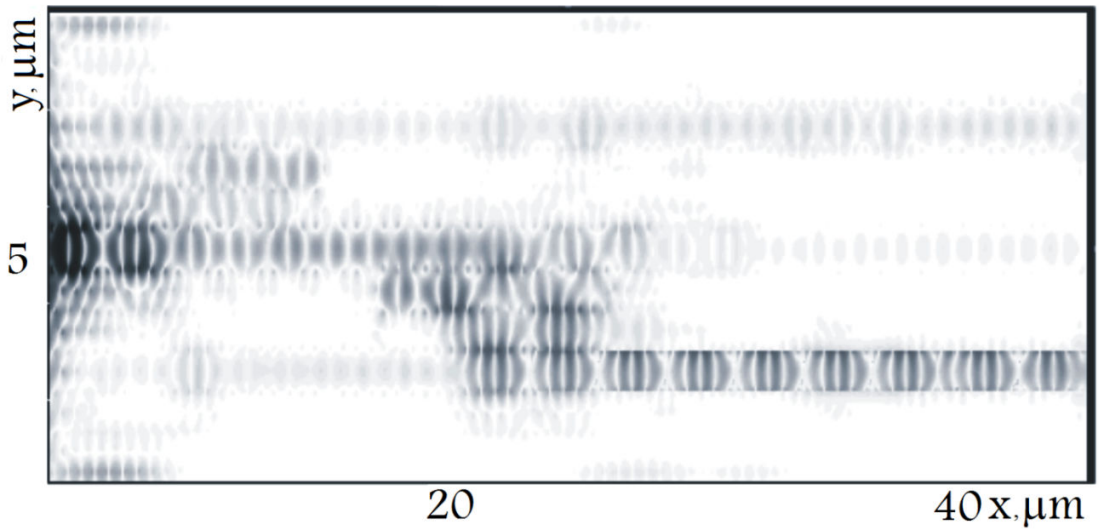

Figure 6.14 EM-field propagation of a continuous wave at λ_1 = 1.417 μm in a 3 × 1 MUX/DEMUX

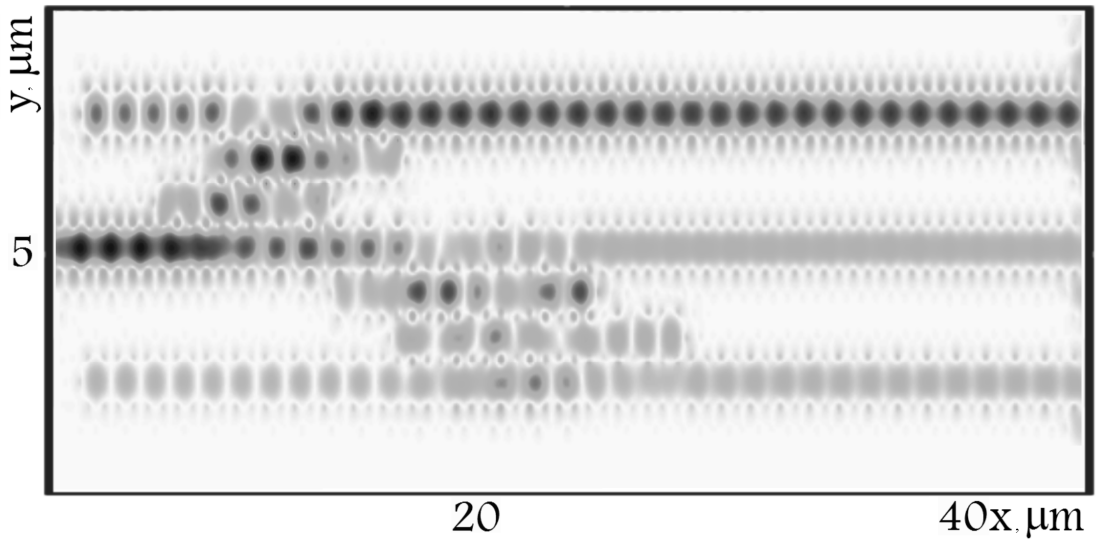

Figure 6.15 EM-field propagation of a continuous wave at λ_2 = 1.55 μm in a 3 × 1 MUX/DEMUX

Next, the study of transmission at the output ports of WG1 and WG2 was carried out. Variation of the transmission with normalised frequency, when the central waveguide and WG2 are separated by five rows of rods to prevent unwanted back and forth coupling between the adjacent waveguides, with two embedded microcavities, is shown in Fig.6.16. Transmission in the output ports of WG1 (P1), and WG2 (P2) are shown with dotted, and solid curves, respectively.

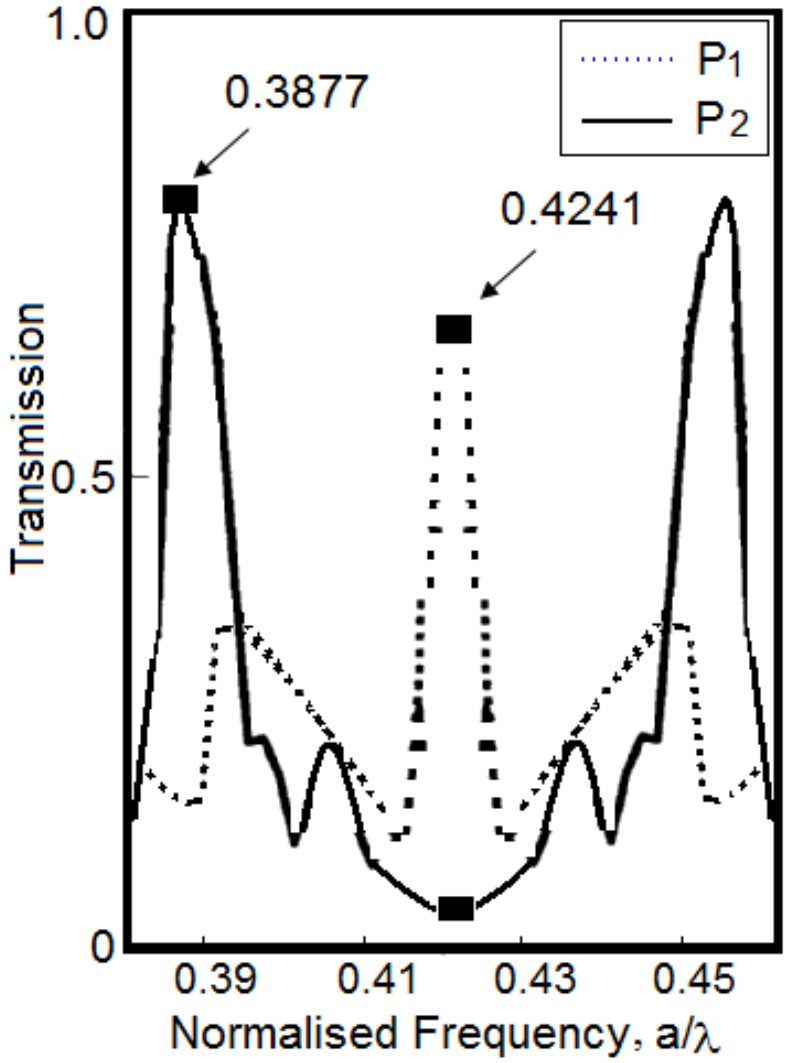

Figure 6.16 Transmission coefficient variation in output ports against normalised frequency

It can be observed that in port I transmission is very low when the normalised frequency is around 0.3877 a / λ and the optical power is transferred to WG2. However, when the normalised frequency is increased to 0.4241 a / λ complete power is transferred to port I. Similar behaviour is observed in port II, transmission is very high when the normalised frequency is at 0.3877 a / λ, while it is very low when the normalised frequency is increased to 0.4241 a / λ and the optical power is transferred to

WG1. For the normalised frequency of 0.3877 a / λ the transmission in port II increases to its maximum of 82.3%, shown with a solid curve.

This phenomenon can be explained by the strong coupling between the microcavities and the selected wavelength. Transmission in port I increases substantially as the normalised frequency is increased to 0.4241 a / λ up to its maximum of 70.6%, shown with a dotted curve. The output power rations at $f_1 = 0.3877\ a / \lambda$ and $f_2 = 0.4241\ a / \lambda$ are 14 and 8 dB, respectively. The output power ration of this newly designed 3 × 1 MUX/DEMUX is much higher than other multiple output ports devices reported in literature [30], and [65], and [66]. The optical efficiency and wavelength directionality of the 3 × 1 MUX/DEMUX is strongly dependant on the geometric parameters of the microcavities, and the position they are placed in with respect to the adjacent waveguides and the wavelength of particular interest.

6.5 Summary

In this chapter the successful novel designs of MUX/DEMUX photonic crystal structures that utilise the coupling length of the waveguide to enhance performance and increases selectively of the device have been presented. The MUX/DEMUX PhC design can be used as a basic building block for more complicated structures. This building block was extensively investigated in isolation, 2 × 1 MUX/DEMUX, and a more complex design, 3 × 1 MUX/DEMUX, and has proven to be extremely competitive with other work in literature [30], such that certain wavelengths can be selected from an input signal using the concept of coupling length and taking it into account when designing the appropriate imbedded microcavities.

Photonic crystal switching devices have proven to live up to their high potential, especially in optical wavelengths. Here, they have been used to design and implement MUX/DEMUX devices, however, they have rarely been explored in the THz range, the following chapter looks at investigating THz ring resonators based on photonic crystals.

Chapter 7

Photonic Crystal Terahertz Ring Resonator

7.1 Introduction

This chapter describes terahertz waves and the use of PhCs in the THz region. Some applications of PhC THz wave devices will be introduced and discussed in detail in this chapter. These devices include cavities, and ring resonators separating two waveguides such that input signals propagate along the input waveguide, couple into the ring resonator and then through to the output waveguide, for a selected wavelength, at the selected output port. The numerical technique used for the design is the CE-ADI-

FDTD with PML boundary conditions.

7.2 THz Background

Terahertz waves are electromagnetic waves with frequency between the microwave and infrared regions of the spectrum. It is not visible, yet, THz warmth can be felt as it is adjacent to the far-infrared radiation on the spectrum. Although THz waves are naturally available, their electromagnetic spectrum has not been investigated as heavily as adjacent regions on the spectrum, microwave and infrared [67]. This is largely because of the practical difficulties required in manufacturing THz sources and detectors that are highly efficient and tightly compact, which lead to it been otherwise known as the THz gap [68]. The manufacturing difficulties are mainly due to the lack of natural materials with appropriate response properties at THz frequency ranges. Nevertheless, researchers have recently invested much resources and attention into this technological gap, potential applications include security screening, military detection, medical diagnosis, biological sensing, radio astronomy, and high speed communication [69 - 72].

In order for THz gap to diminish, it is necessary to develop components and devices that respond appropriately in the THz range. This gap means that significant devices have not yet been fabricated, nor even designed. Such devices include switches, modulators, phase shifters, and multiplexers/demultiplexers [73].

This THz range/gap is where the optics and electronics meet. Below the gap are electronic technologies and above the gap are photonics and optics.

7.3 Terahertz Applications and Properties

7.3.1 THz applications

The THz spectral range of 30 μm to 3 *mm* has many special features associated with fundamental physical processes such as rotational transitions of molecules, where the electromagnetic field exerts a torque on the molecule, molecular vibrational motions of organic compounds known as vibrational spectroscopy, which measures transitions from one molecular vibrational energy level to another, lattice harmonics in solids, and intraband transitions or intersubband absorptions in semiconductors and quantum wells [67].

THz waves show very high atmospheric opacity, where the main cause of THz attenuation in the atmosphere is water vapour. Fig. 7.1 displays the spectral range that THz occupies, and shows the atmospheric effects upon the spectrum.

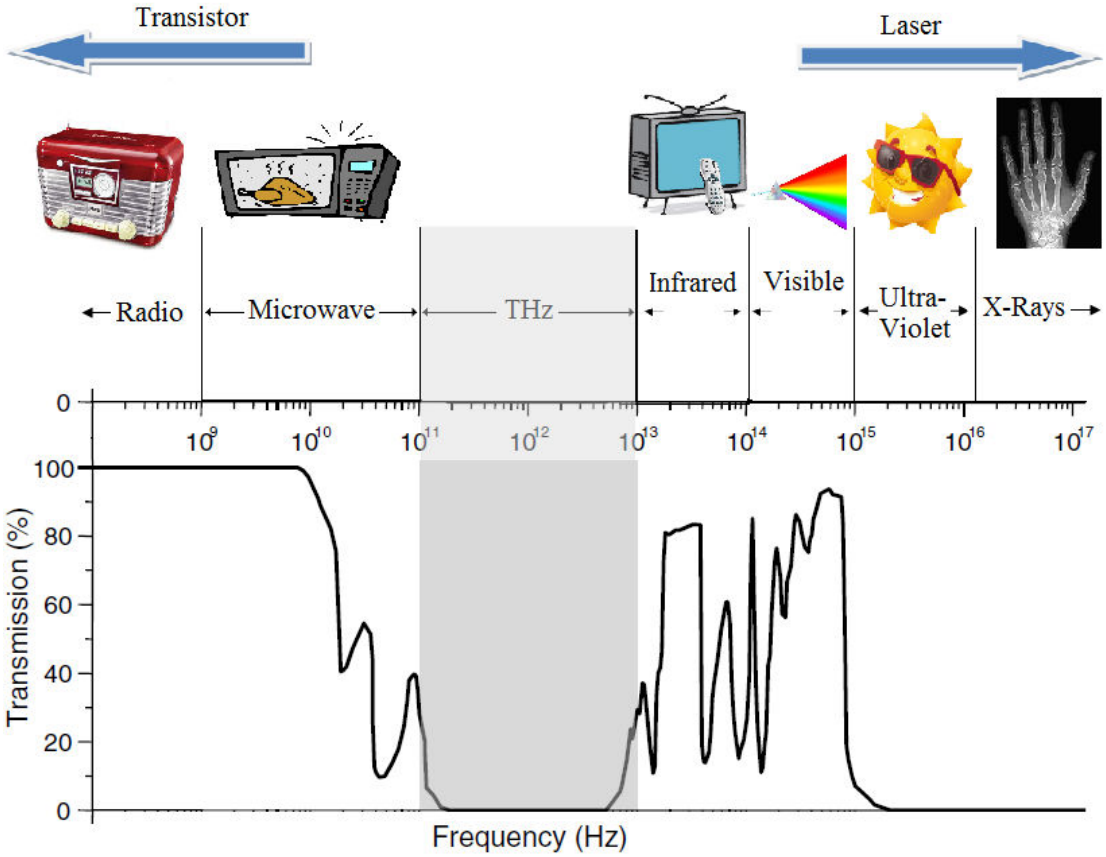

Figure 7.1THz range in the electromagnetic spectrum, and the corresponding atmospheric transmission, data from [69]

7.3.2 THz properties

In general, a waveguide is a transmission instrument used to carry electromagnetic waves from the source to the destination with insignificant losses. As explained in chapter 2, a waveguide in photonic crystals is particularly designed by inserting a line of defects within the periodic lattice.

The conventional waveguide used near the lower THz range, in the microwave range, is the hollow metal pipe, while optical fibre is the dominant means of wave guiding in optical communication. Such technologies have been researched and

investigated for the purposes of implementing in the THz range. However, these techniques use unsuitable materials that cause high absorption of the THz waves, therefore, artificial materials have been explored. These artificial materials mainly include metamaterials [74], photonic crystals [73], and plasmonics [75]. Due to the nature of this research, and the many attributes of photonic crystals in channelling electromagnetic waves, these PhCs have been heavily investigated for the purpose of designing, modelling, and simulating THz waveguide switching devices that are highly efficient in transmission and tightly compact in design.

7.4 THz Ring Resonator Cavity

The two-channel ring resonator based on a PhC waveguide coupler considered in this study consists of a background dielectric of Silicon Oxide (SiO_2) with periodic holes in a square lattice. The SiO_2 used in the structure has refractive index 1.5 in THz range with negligible absorption [71]. All holes were filled with electrorheological fluids, which have a phenomenon that fluidity of liquids such as silicon oil can be modified by application of an electric field. Electrorheological fluids using polyaniline have a refractive index that varies from 4.848 to 4.393 at THz range by applying an external electric field of 2.8 V/*mm* with a response time of 100 μs [71].

The radii of the polyaniline holes is $r = 0.185a$ where a is the lattice constant, $a = 68.75\mu m$. The PBG ranges from the normalised frequency units (a/λ) 0.20 to 0.29, where λ is the wavelength in vacuum. The design of the two-channel PCRR in [76] is investigated. This structure has been initially reported by Maleki *et al*. [76], where the waveguide coupler consists of two parallel photonic crystal waveguides, WG1 and

WG2, separated by a 5 × 5 square ring resonator, the ring resonator is as shown in Fig.7.2. Since the square ring has sharp corners, there is a counter propagating mode resulting from back reflection. In order to minimise this effect, an extra hole is added at the centre of the unit cell in each corner creating a semi-square ring.

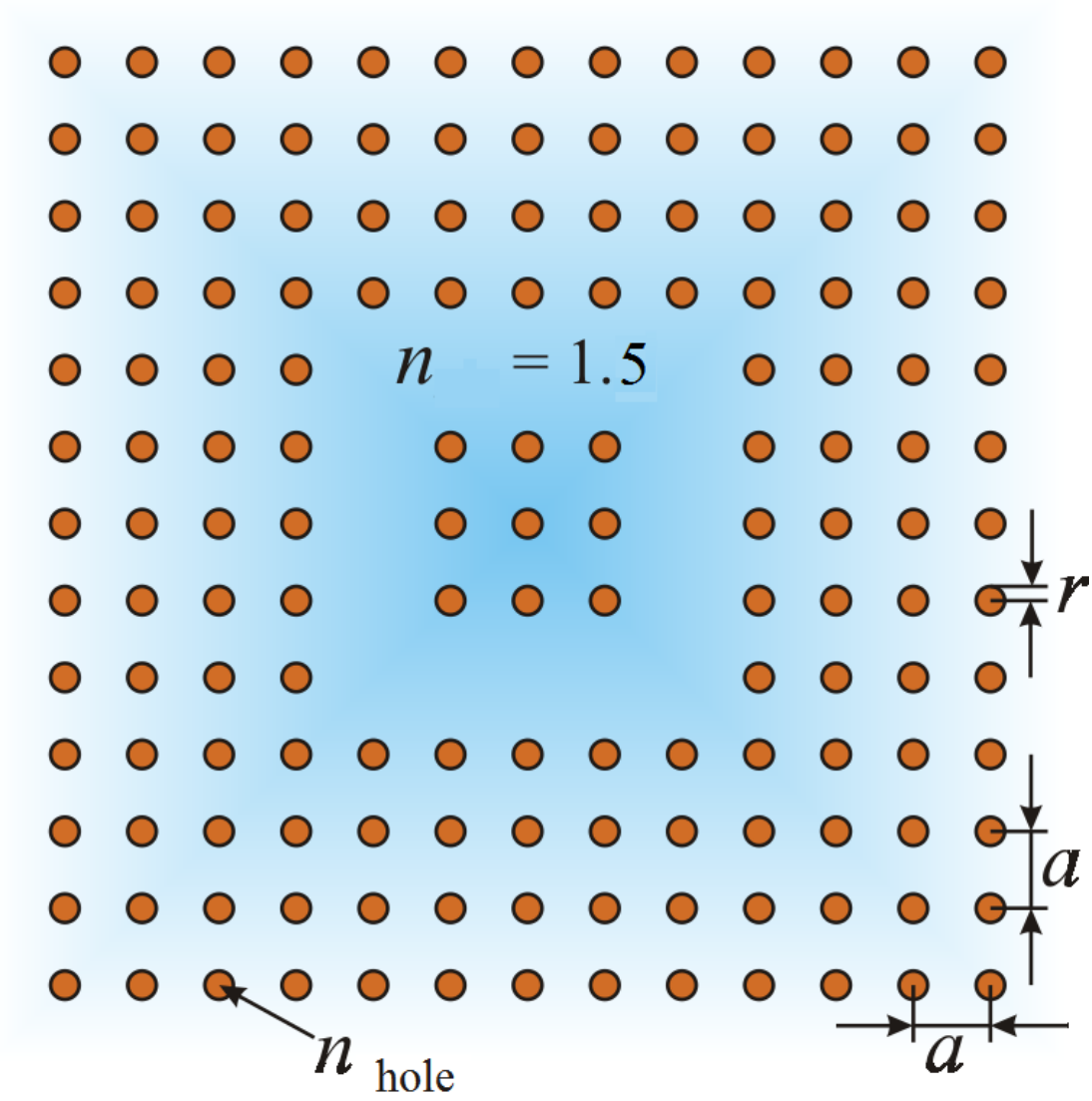

Figure 7.2 Schematic diagram of a 5 × 5 square ring resonator

All the resonant modes in this photonic crystal ring resonator can be excited as reported in [73] by inserting a modulated Gaussian pulse with spectrum covering the entire PBG inserted in an asymmetric direction of the structure. With several detectors placed in the ring resonator, the electric field can be monitored at any time step, and at

the end the fast Fourier transform of the received signal can be derived, the electric field propagation and spectrum are shown in Figures 7.3 and 7.4, respectively.

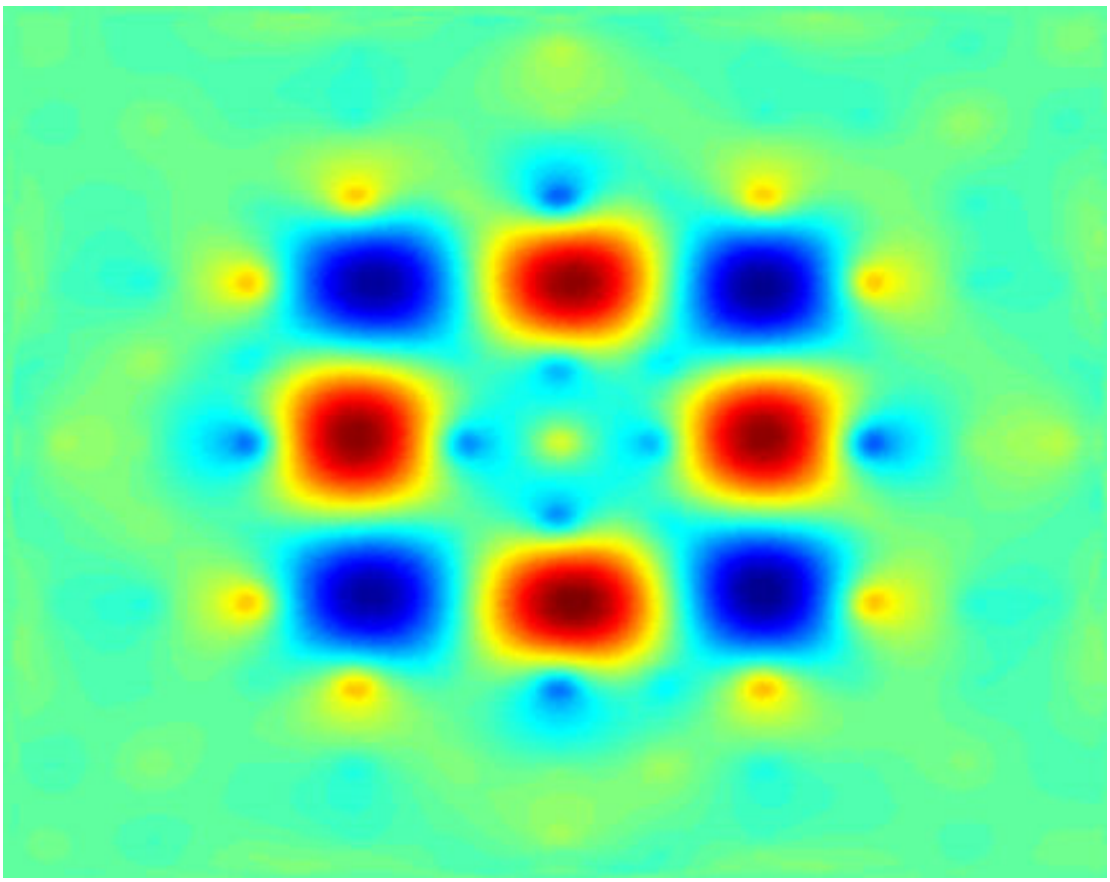

Figure 7.3 Electric field propagation in the 5 × 5 photonic crystal semi square ring resonator

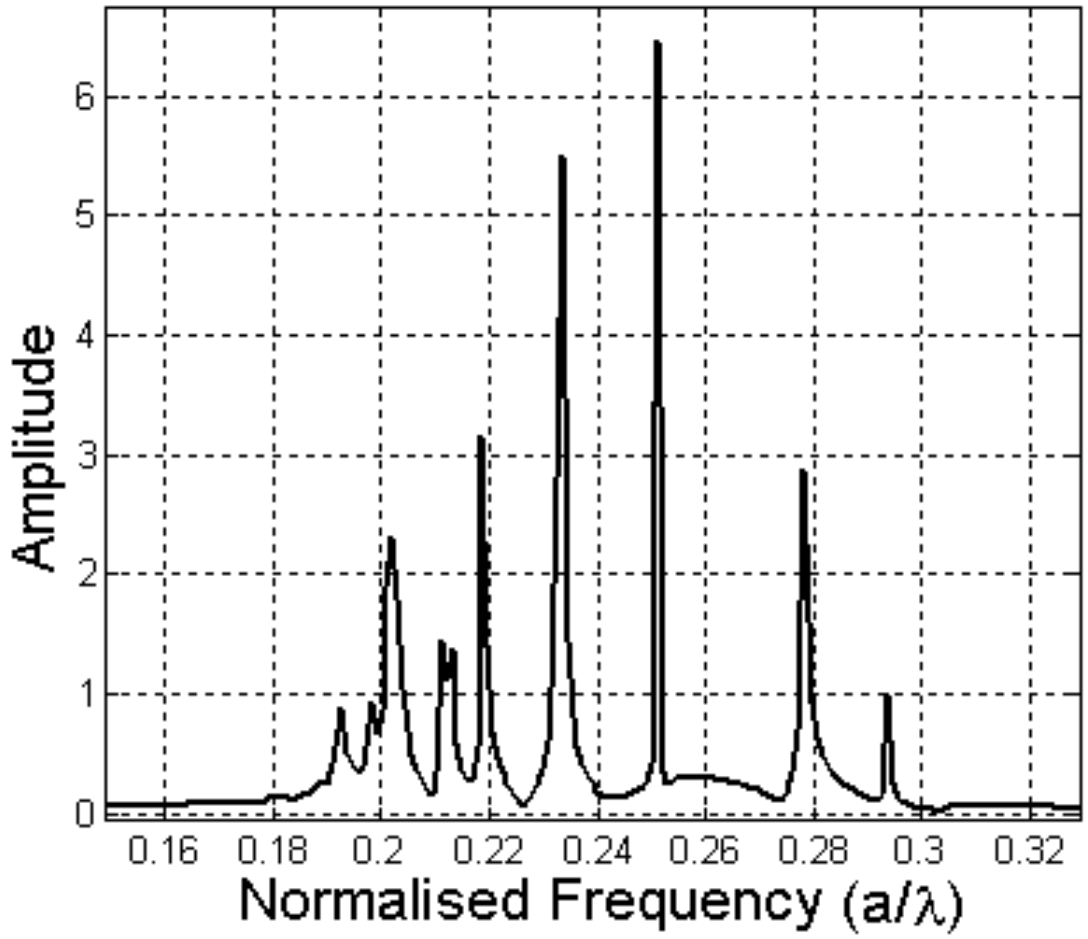

Figure 7.4 Spectrum of the 5 × 5 photonic crystal semi square ring resonator

It can be noticed from figures 7.3 and 7.4 that the resonant modes are supported by the PBG and that the spectral response has many peaks that are the resonant frequencies of the structure. In comparison with point defects, such a structure has multi-modes therefore offering more flexibility in mode design.

7.5 THz Ring Resonator Switch

The WG coupler that consists of two parallel photonic crystal waveguides, WG1 and WG2, separated by a 5 × 5 semi-square ring resonator, the ring resonator is as shown in Fig.7.5.

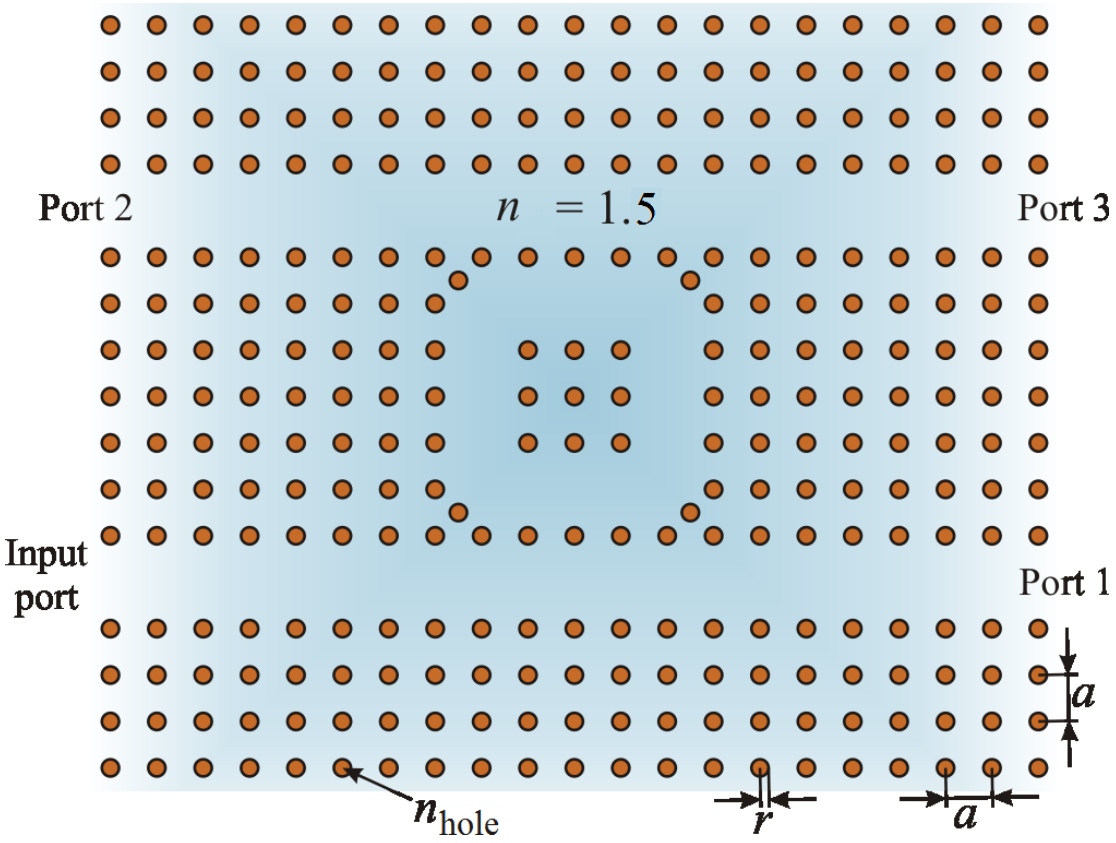

Figure 7.5 5 × 5 Photonic crystal semi square ring resonator switching device

This structure was selected to enable direct comparison between the design results here and those recorded in [73].

A Gaussian shaped profile was modulated by a continuous wave source in time with the wavelength fixed to $\lambda = 268.55\ \mu m$. This source was used to excite the structure

in Fig.7.5. The signal propagated in the structure, such that the wave coupled from the input waveguide to the output waveguide via the ring resonator. Fig.7.6 illustrates the E-field propagation in the structure that confirms the results in [73].

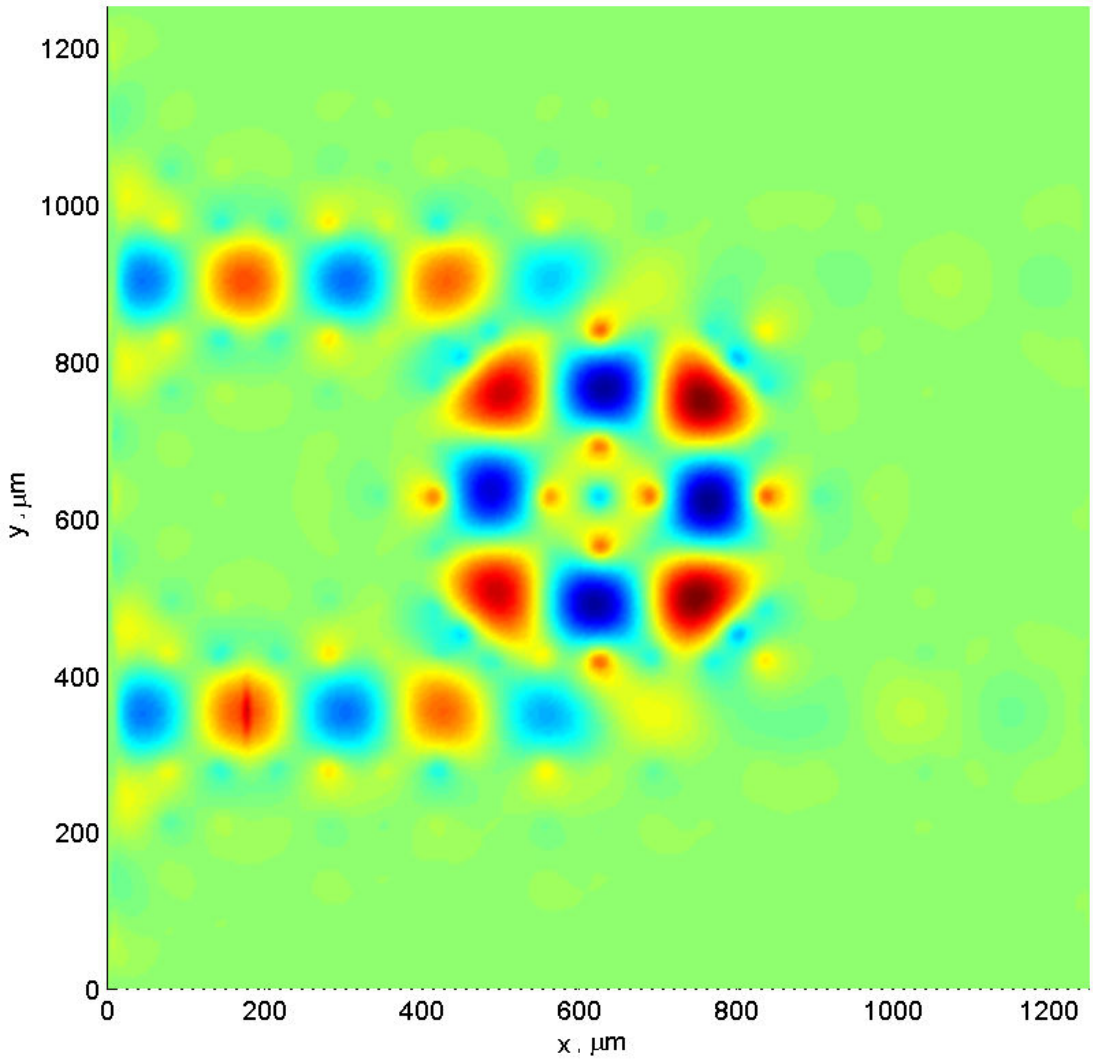

Figure 7.6 Electric field propagation without external electric field

In order to demonstrate the switching performance of the structure of Fig.7.5, the electric field distribution at steady state without applied external electric field is as

shown above in Fig.7.6, while the electric field distribution at steady state with applied external electric field is as illustrated in Fig.7.7.

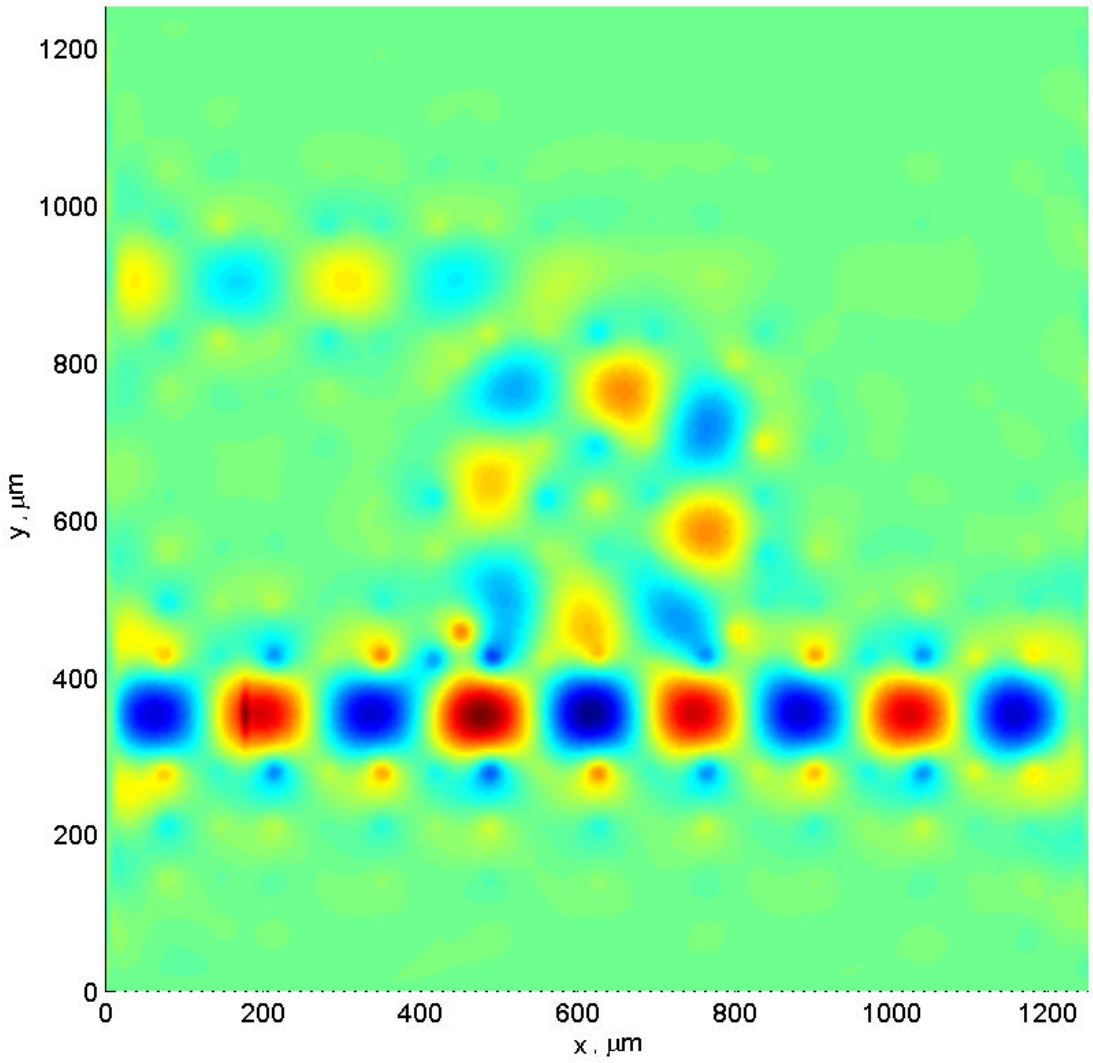

Figure 7.7 Electric field propagation with external electric field applied

It is clear that at normalised frequency of 0.256, which is the resonant frequency of the ring resonator, the input lightwave is coupled to the output at port II. However, when a suitable voltage is applied to the electrodes of the electro-optic switch the lightwaves of the output at port II are switched to output at port I.

7.6 Improved Design of THz Ring Resonator Switch

In order to improve on the performance and coupling between the two waveguides of this structure, which was reported to have a transmission of 83.38%, several solutions can be implemented. In [30] and [64] dielectric holes/rods with different refractive index have been used in order to improve trapping photons and controlling the lightwave. However, this solution requires the use of different dielectric material which can be difficult to realise practically. The optimisation approach taken in this study was to introduce defects in order to better trap photons and enhance controlling the lightwave. Several defects were introduced with careful geometrical consideration so as to optimised the efficiency of the device in terms of the ratio of the output signals port II to port I. Five tests were carried out in order to thoroughly investigate the effect of inserting defects into the system

7.6.1 Four-sided wall cavity

First, the radius of the holes around the parameter of the semi square ring resonator was varied from its original value of $r = 0.185a$ to selected radii values ranging from $r = 0.16a$ to $r = 0.20a$, Fig.7.8 illustrates the schematics of this switch. Then, the continuous wave used above was inserted into the structure and the efficiency of the output signal ratio of port II to port I was recorded. The results are displayed in Fig. 7.9.

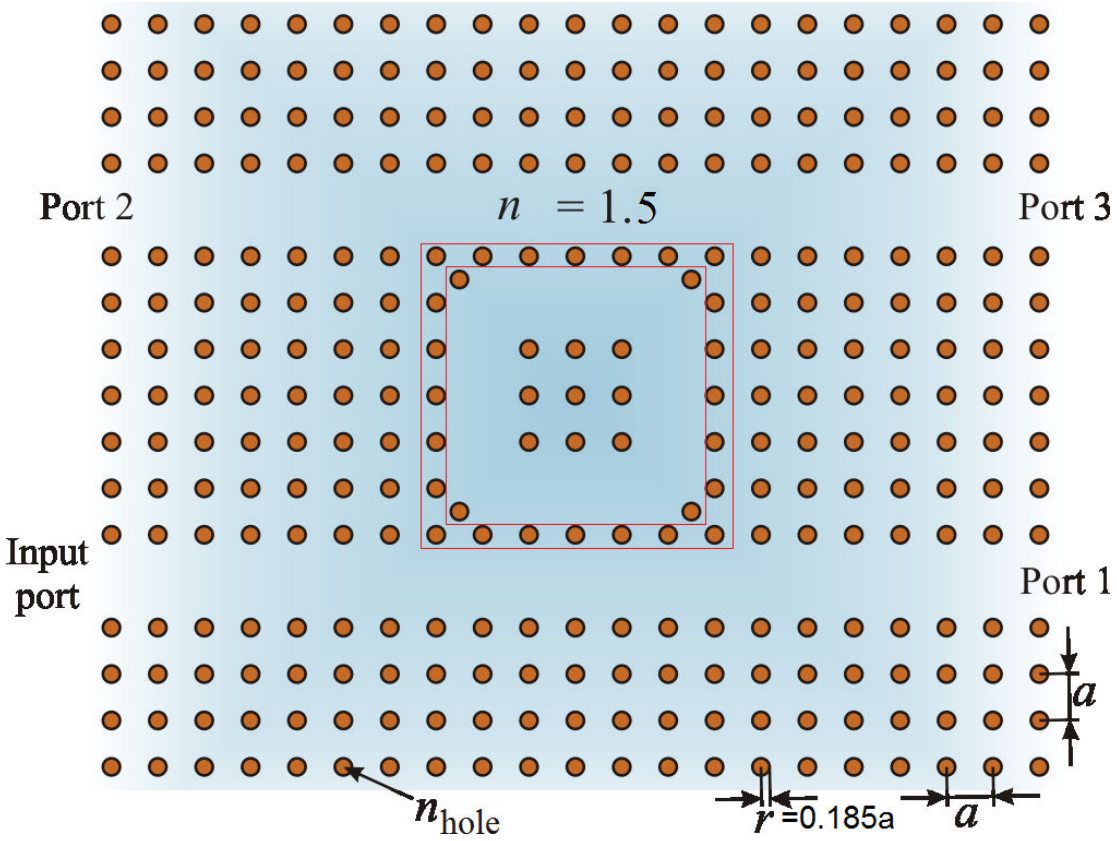

Figure 7.8 Schematics of the PCRR with the holes around the RR varied in radius

Physically, the size of the hole can be changed by removing the original holes and then replacing it with a new smaller hole from the same material.

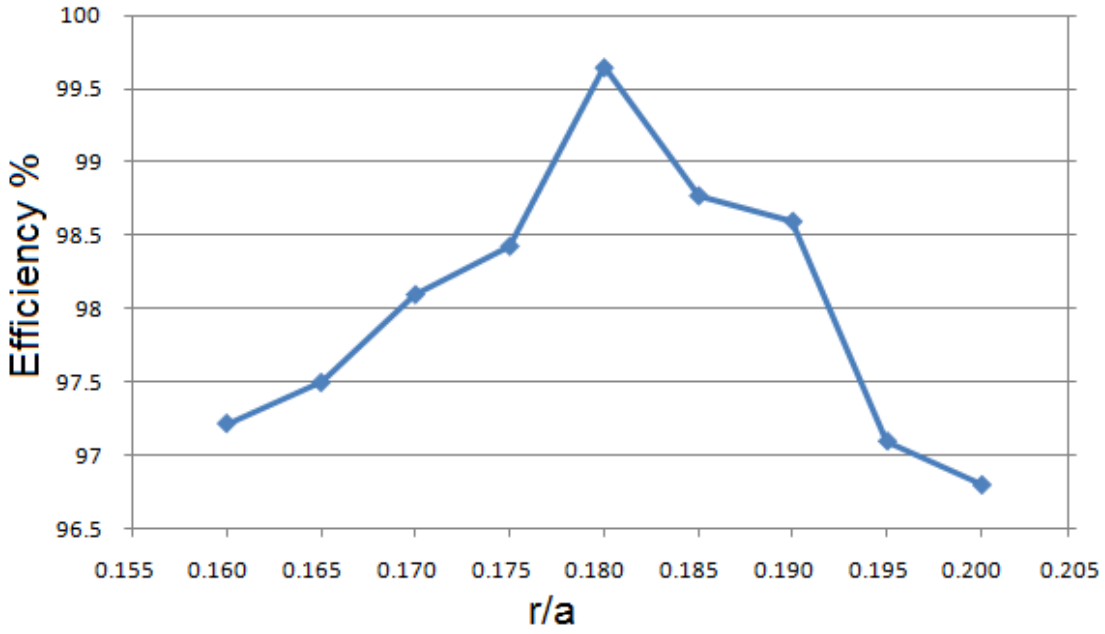

Figure 7.9 Radius of the holes surrounding the ring resonator is varied.

Fig. 7.9 shows the effect of the defects inserted into the ring resonator structure illustrated in Fig. 7.8. The performance, which is in terms of efficiency, clearly indicates that as the size of the defect rods varies, the efficiency changes such that the optimum output occurs at $r = 0.18\ a$, producing an efficiency $eff = 99.65$ %.

7.6.2 Two-sided wall cavity

In the second test, the radius was again varied, but this time, only the holes separating the ring resonator and the adjacent waveguides were changed. Again, the radius range was between $r = 0.16a$ to $r = 0.20a$, Fig.7.10 illustrates the schematics of this switch. Then, the same continuous wave was inserted into structure and the efficiency of the output signal ratio of port II to port I was recorded. The results are displayed in Fig. 7.11.

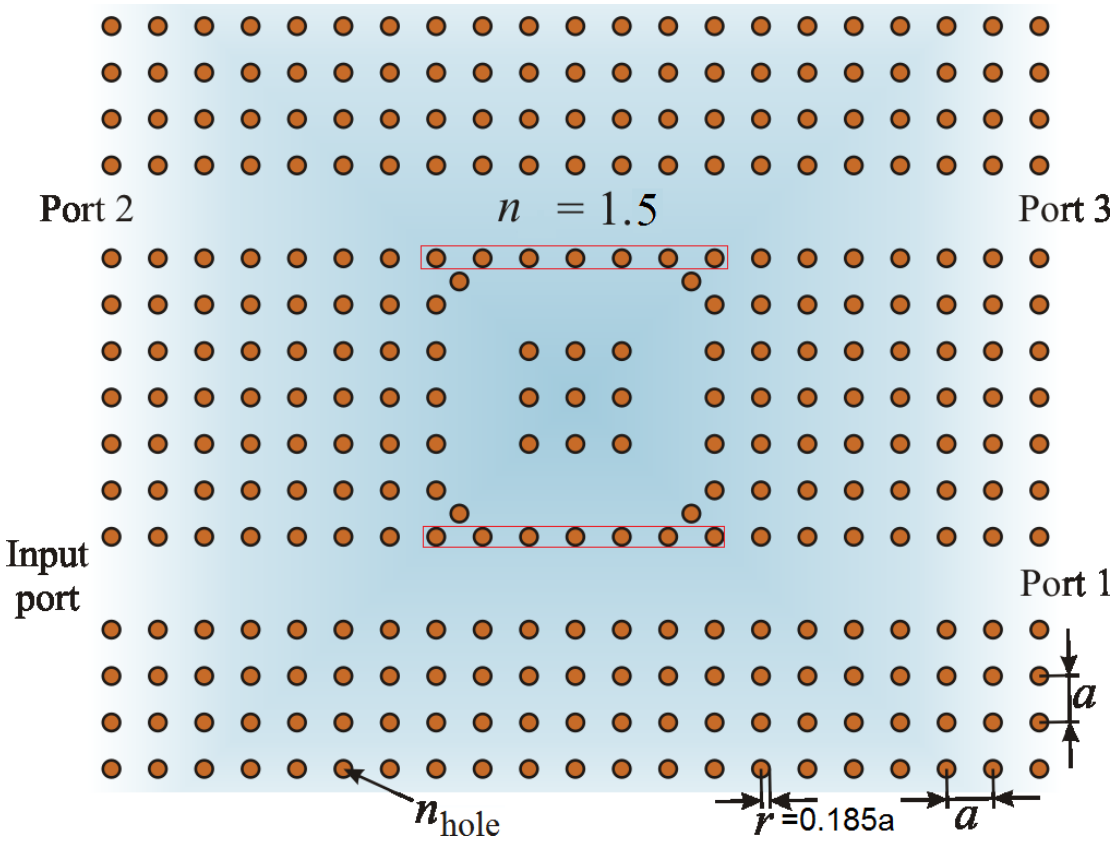

Figure 7.10 Schematics of the PCRR with the holes separating the RR and the waveguides varied in radius

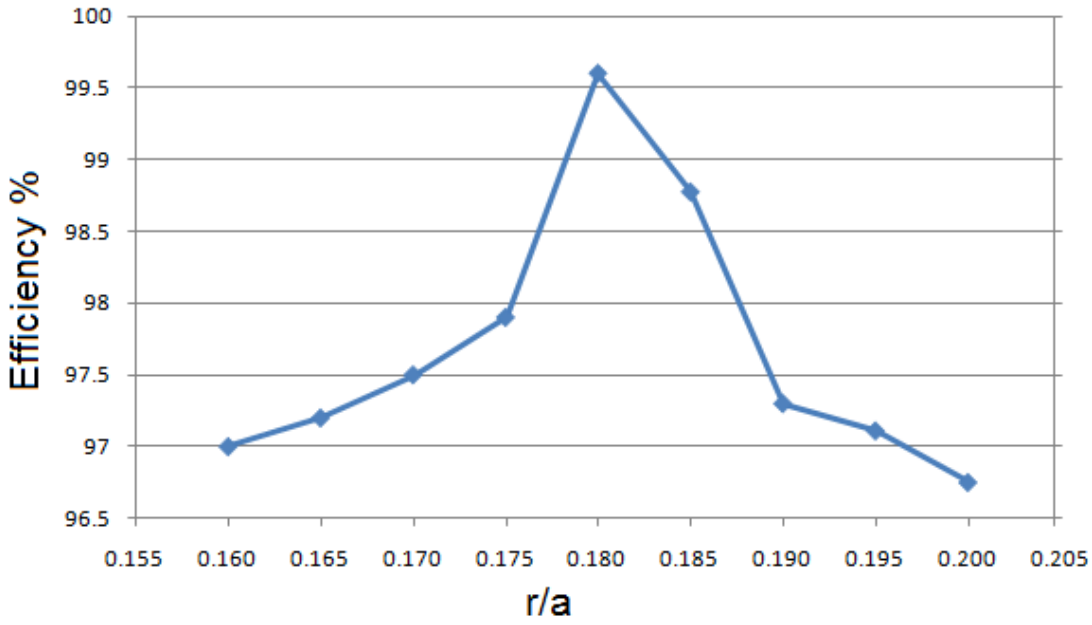

Figure 7.11 Radius of the holes separating the ring resonator and the waveguides is varied.

Fig. 7.11 shows the effect of the defects inserted into the ring resonator structure illustrated in Fig. 7.10. The performance, which is in terms of efficiency, clearly indicates that as the size of the defect rods varies, the efficiency changes such that the optimum output occurs at $r = 0.18\ a$, producing an efficiency $eff = 99.6$ %.

7.6.3 Single-sided wall cavity

In the third test, the radius was again varied, such that the holes separating the ring resonator and the adjacent output waveguide were changed. Again, the radius range was between $r = 0.16a$ to $r = 0.20a$, Fig.7.12 illustrates the schematics of this switch. Then, the same continuous wave was inserted into structure and the efficiency of the output signal ratio of port II to port I was recorded. The results are displayed in Fig. 7.13.

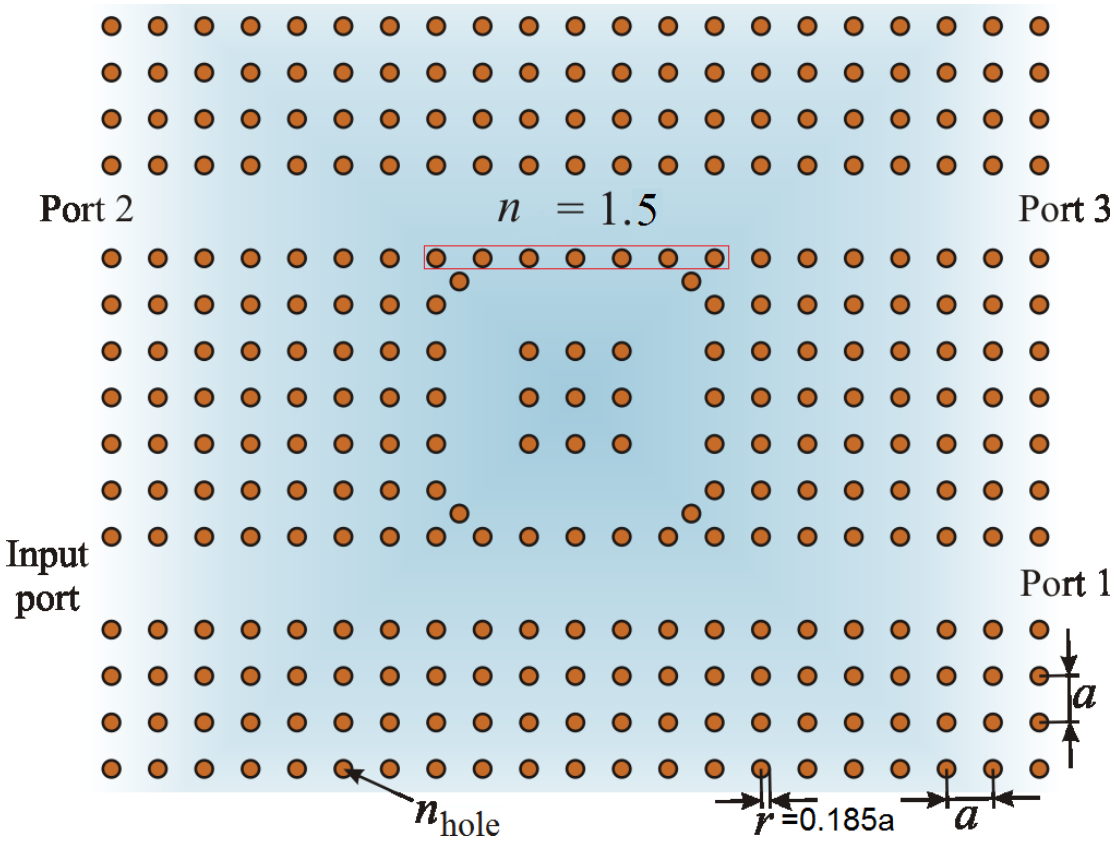

Figure 7.12 Schematics of the PCRR with the holes separating the RR and the output waveguide varied in radius

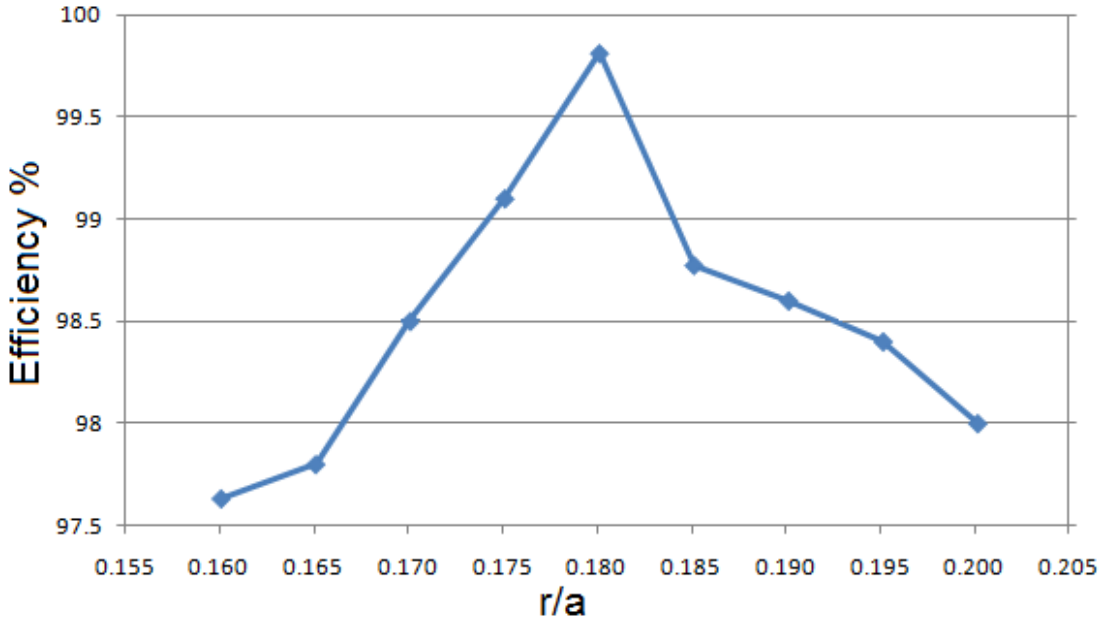

Figure 7.13 Radius of the holes separating the ring resonator and the output waveguide is varied.

Fig. 7.13 shows the effect of the defects inserted into the ring resonator structure illustrated in Fig. 7.12. The performance, which is in terms of efficiency, clearly indicates that as the size of the defect rods varies, the efficiency changes such that the optimum output occurs at $r = 0.18\ a$, producing an efficiency $eff = 99.8$ %.

7.6.4 Corners cavity

In the fourth test, the radius was again varied. The holes at the corners of the ring resonator were changed. Again, the radius range was between $r = 0.16a$ to $r = 0.20a$, Fig.7.14 illustrates the schematics of this switch. Then, the same continuous wave was inserted into structure and the efficiency of the output signal ratio of port II to port I was recorded. The results are displayed in Fig. 7.15.

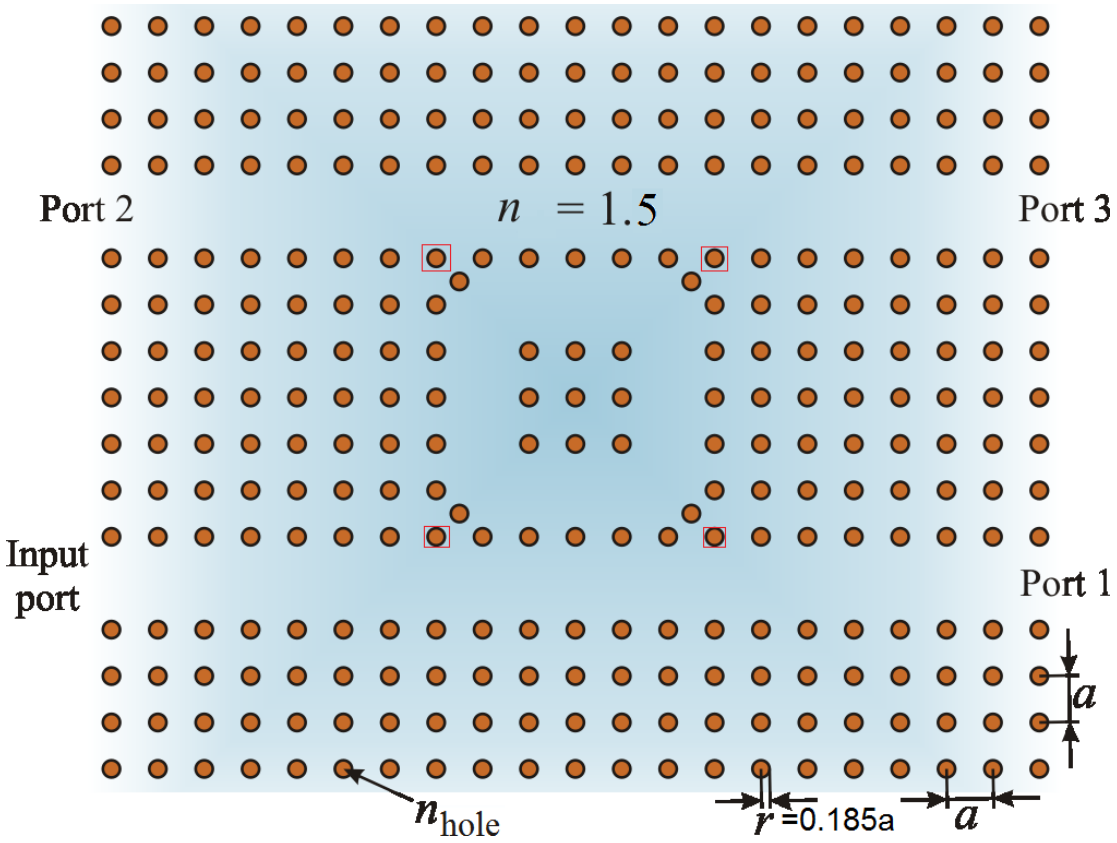

Figure 7.14 Schematics of the PCRR with the corner holes of the RR varied in radius

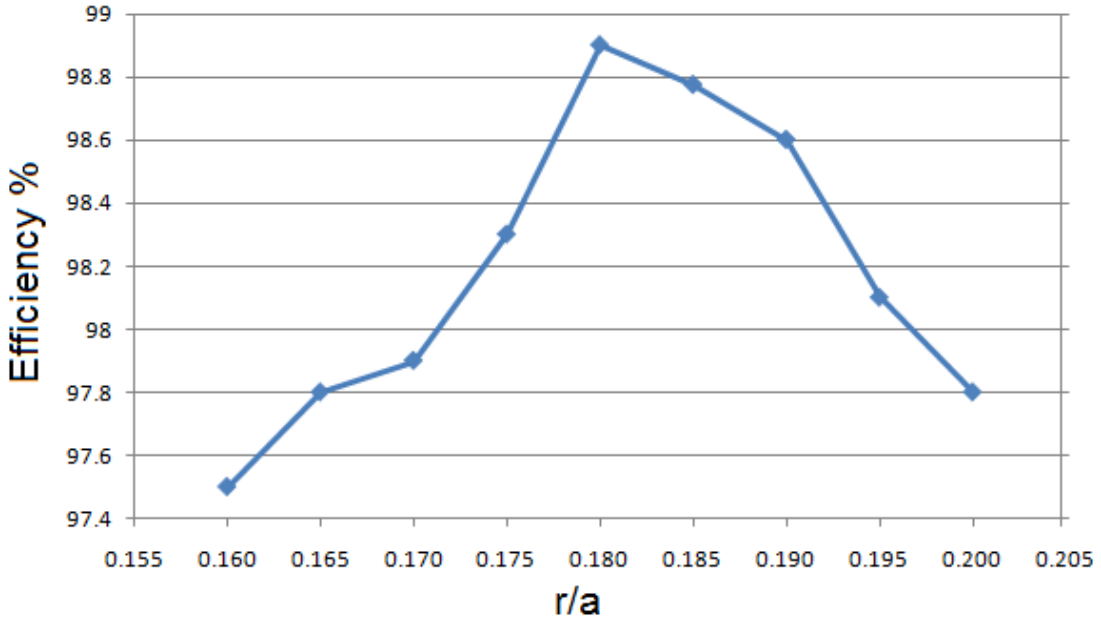

Figure 7.15 Radius of the holes at the corners of the ring resonator is varied.

Fig. 7.15 shows the effect of the defects inserted into the ring resonator structure illustrated in Fig. 7.14. The performance, which is in terms of efficiency, clearly indicates that as the size of the defect rods varies, the efficiency changes such that the optimum output occurs at $r = 0.18\ a$, producing an efficiency $eff = 98.9$ %.

7.6.5 Single-sided wall and single corner cavity

In the fifth and final test, the radius was again varied such that a combination was used where the holes separating the ring resonator and the output waveguide were changed as well as the corner hole at the transition point between the input waveguide and the ring resonator. Again, the radius range was between $r = 0.16a$ to $r = 0.20a$, Fig.7.16 illustrates the schematics of this switch. Then, the same continuous wave was

inserted into structure and the efficiency of the output signal ratio of port II to port I was recorded. The results are displayed in Fig. 7.17.

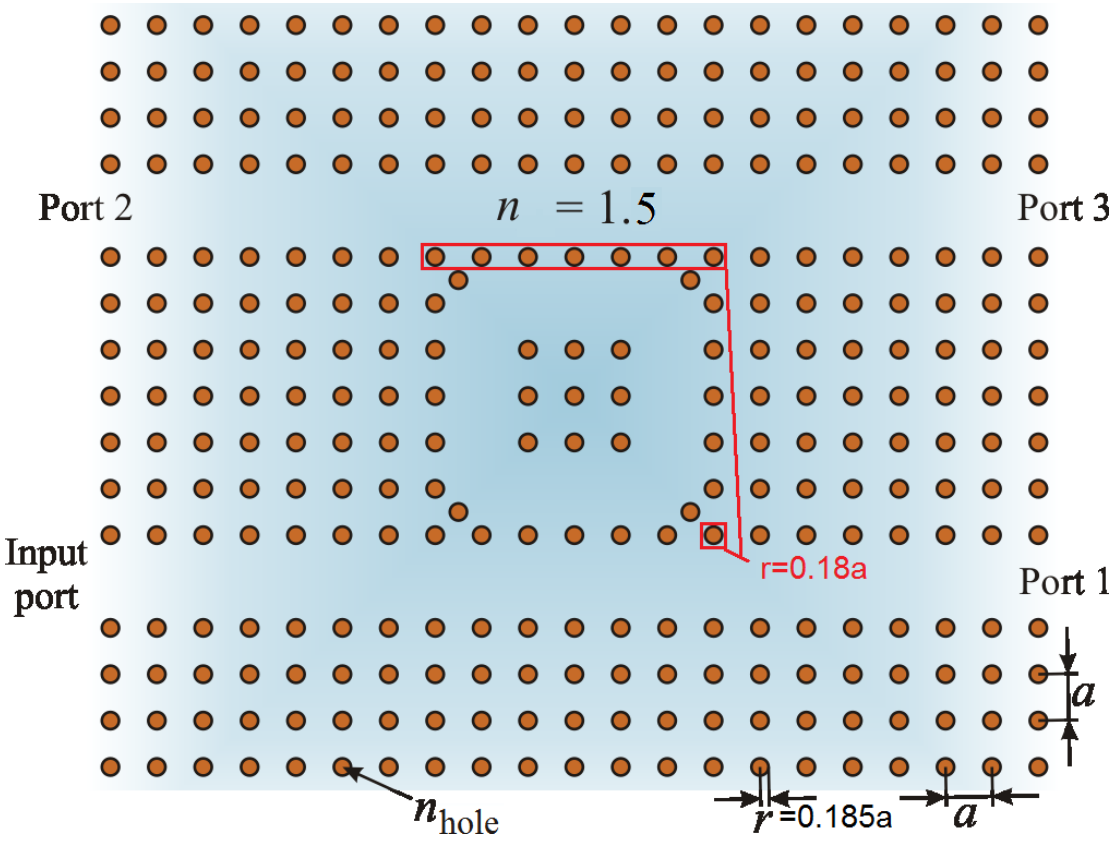

Figure 7.16 Schematics of the PCRR with the holes separating the RR and the output waveguide as well as the far corner hole near the input waveguide varied in radius

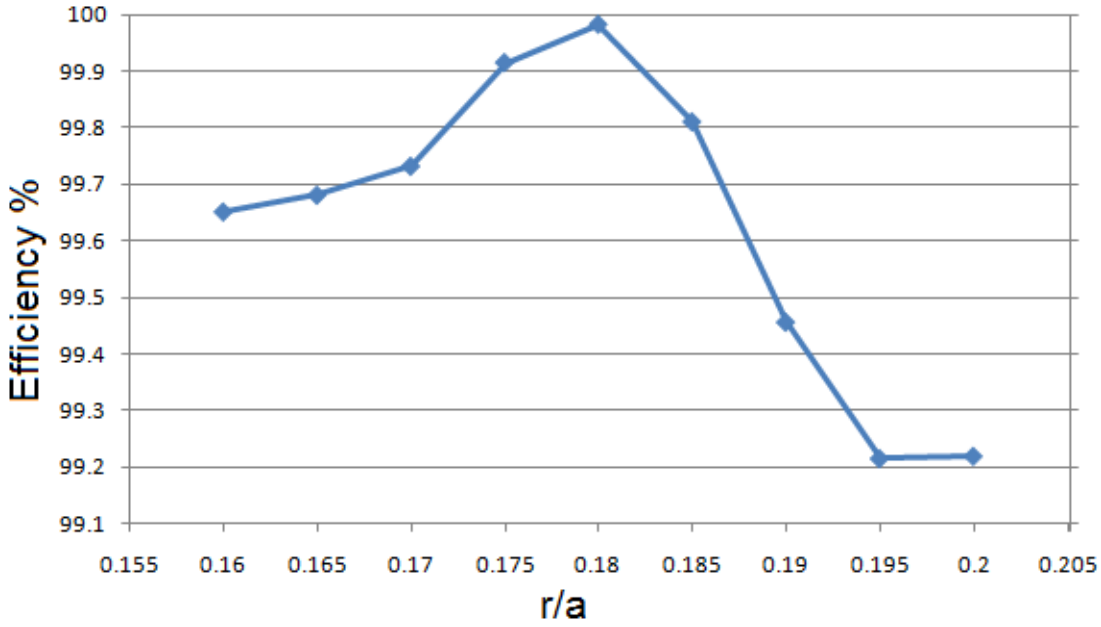

Figure 7.17 Radius of the holes separating the ring resonator and the output waveguide as well as the corner hole at the transition point between the input waveguide and the ring resonator is varied.

It should be noted here that the defect is introduced inside the 2D photonic bandgap structure on the crossing point between the input waveguide and the adjacent ring resonator. Also, on the far side of the ring resonator, the row of holes between the ring resonator and the output waveguide, defects are also inserted. Other holes were also investigated in terms of the optical efficiency, however, these particular holes illustrated in Fig.7.17, showed a better performance of the power efficiency compared to other holes, particularly, at $r = 0.18\ a$, with an efficiency $eff = 99.9$ %.

7.7 Transmission Characteristics

7.7.1 Transmission in switch without added cavities

After that, the study of transmission at each port of the device with four ports (input port, port I, port II, and port III) was carried out, the transmission is the ratio of the selected output port to the input port. Variation of the transmission with normalised frequency, when two photonic crystal waveguides are separated by a 5 × 5 semi-square ring resonator in its original reported form in [73] is shown in Fig.7.18.

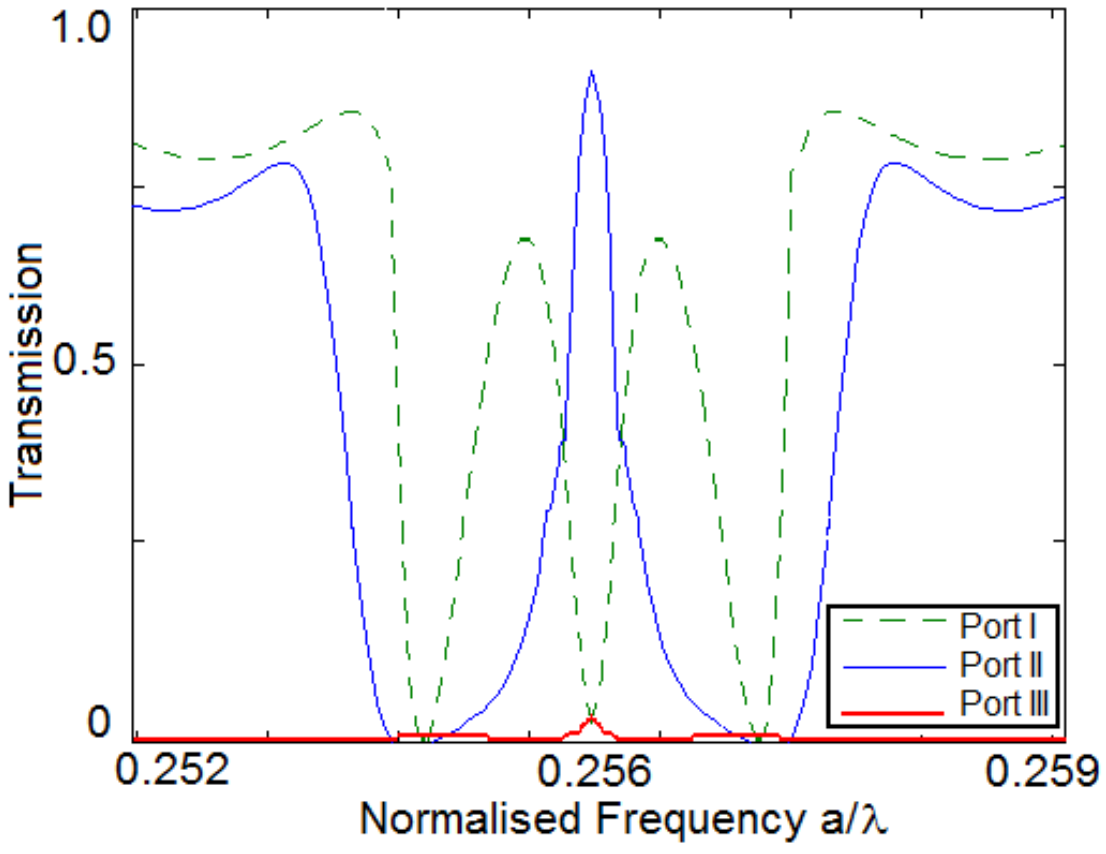

Figure 7.18 Transmission in the structure without defects.

In Fig. 7.18 the transmission in port I, port II, and port III are shown with green

dashed, blue solid, and red solid curves, respectively. It can be observed that in port I transmission is very low and the optical power is transferred to the output waveguide.

7.7.2 Transmission in switch with single-sided wall and single corner cavity

The transmission across the three ports with the inserted defects from Fig.7.16 was as shown in Fig.7.19.

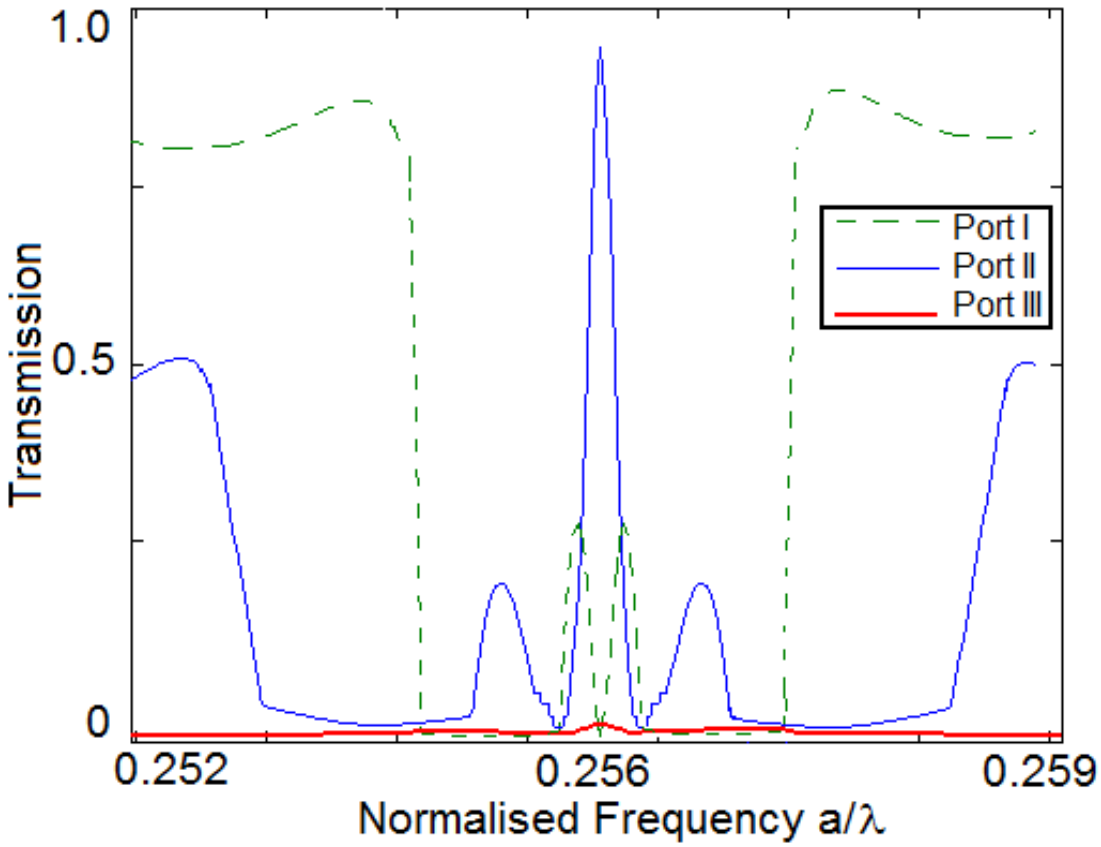

Figure 7.19 Transmission in the structure with inserted defects

In Fig. 7.19 the transmission in port I, port II, and port III are shown with green dashed, blue solid, and red solid curves, respectively. It can be observed that in all ports

there is substantial transmission that subsequently affects the overall optical power transferred to the selected output port.

7.7.3 Transmission in switch with defects and only two output ports

Fig.7.20 illustrates the structure with the defects and port III removed, this structure with the removed port is based on the work reported in Chein *et al*. [77] such that the backward coupled wave can merge with the forward wave through constructive interference at a merging point in order to obtain maximum output power.

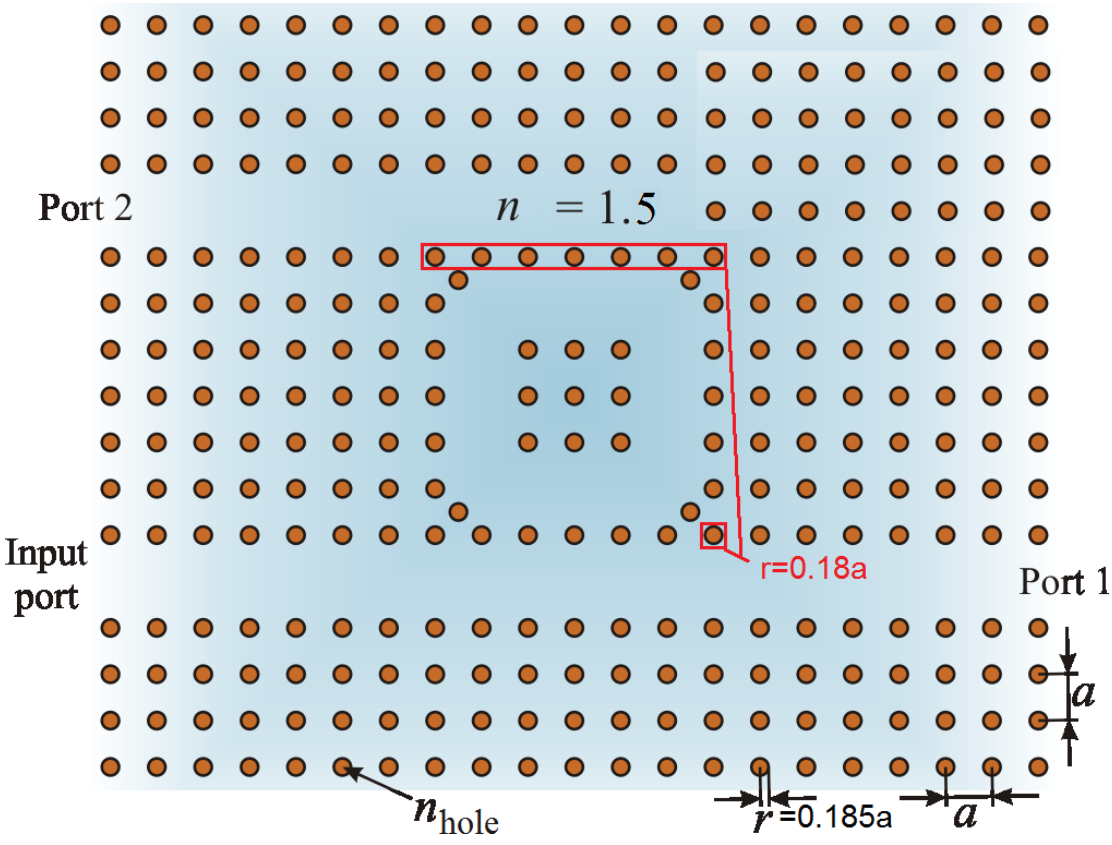

Figure 7.20 Schematics of the PCRR with port III removed

The corresponding E-field propagation and transmission of ports I and II for the structure with the inserted defects where port III is removed are shown in figures 7.20 and 7.21, respectively.

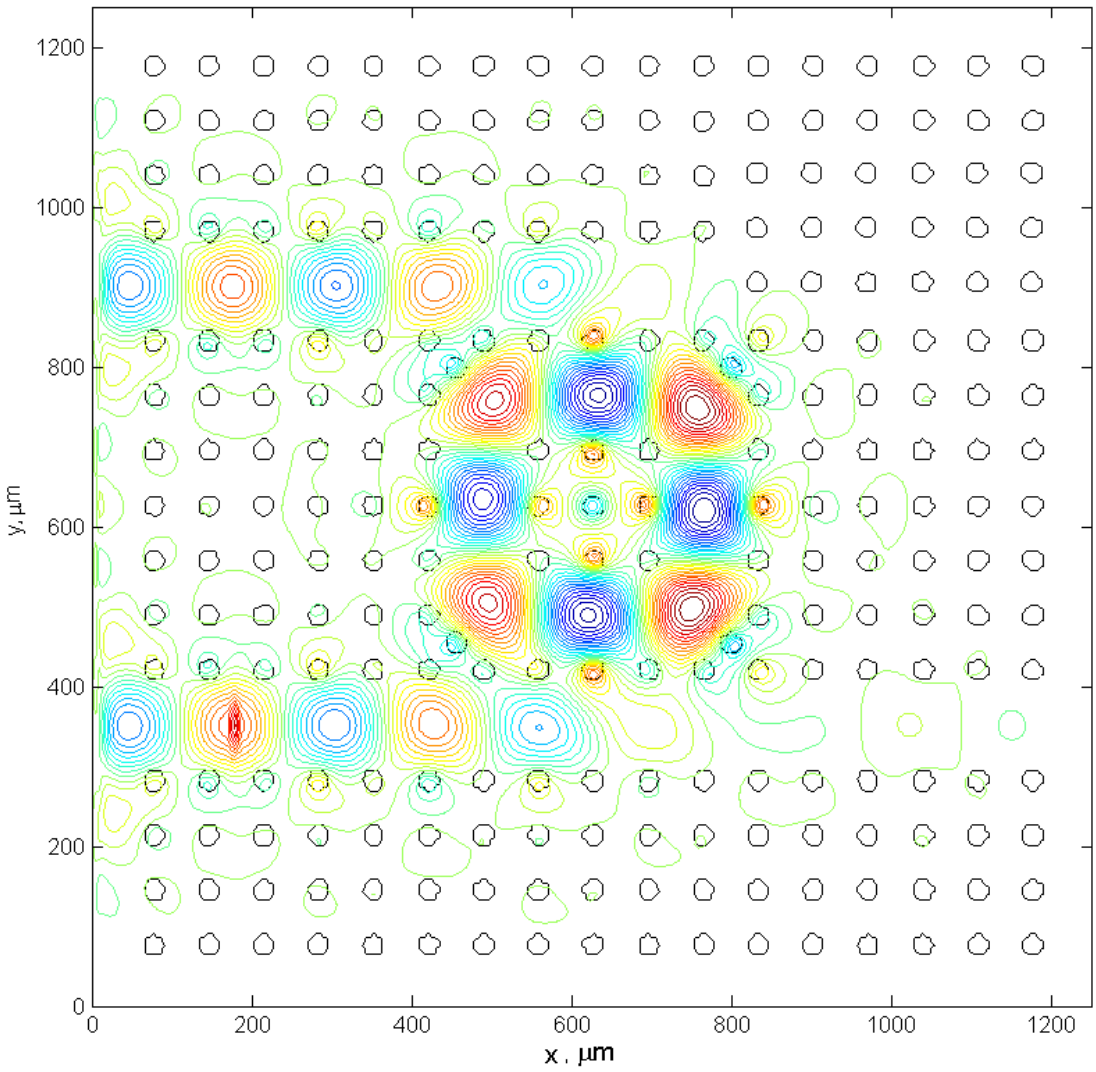

Figure 7.21 Contour map of electric field propagation in the structure with port III removed

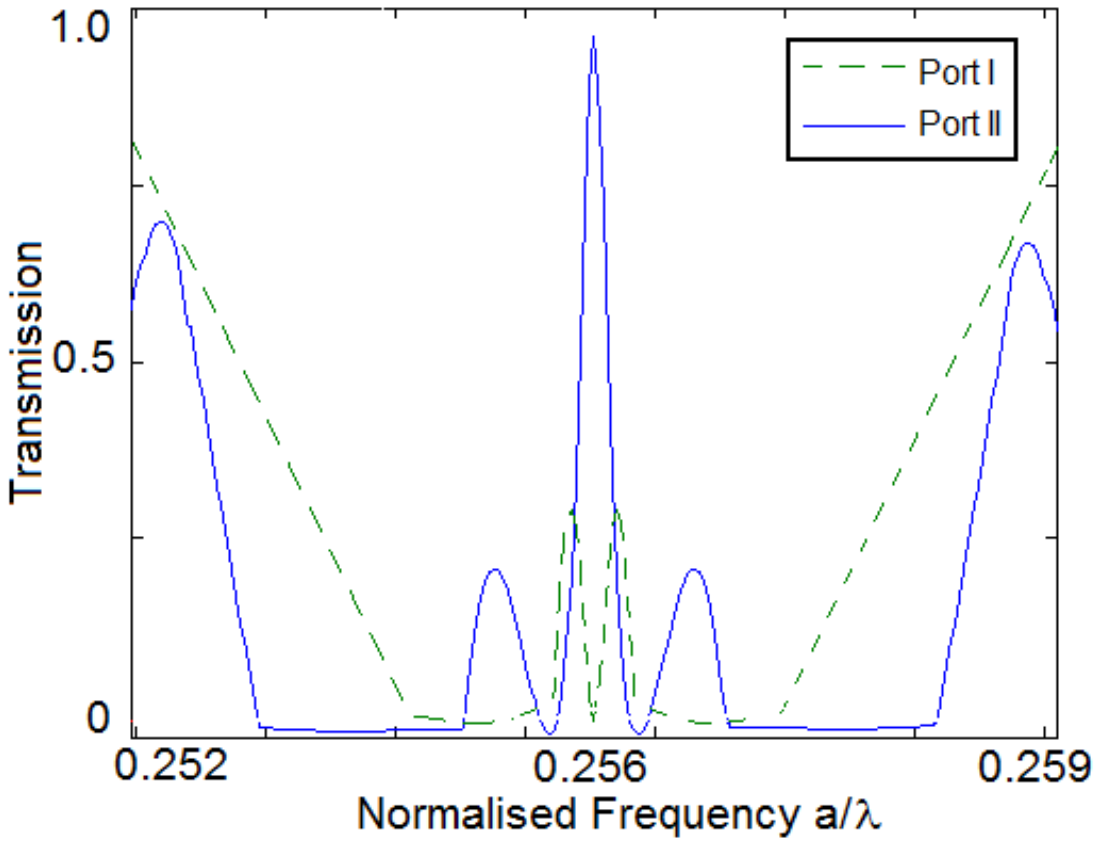

Figure 7.22 Transmission with inserted defects and removed port III

In Fig. 7.22 the transmission in port I, and port II are shown with solid and dashed curves, respectively. It can be observed that the optical power is transferred to the output waveguide at the selected output port is optimum as port I shows almost zero transmission at the selected wavelength.

Table 7.1 below holds a direct comparison between all three structures and their performances in terms of transmission and efficiency, which can both be expressed as in the equations below

Transmission = (Input Port / Output Port) × 100

Efficiency = (Port I / Port II) × 100

Table 7.1 THz structure performance comparison

Structure	Transmission	Efficiency
Without defect	83.38 %	98.77%
With defect	97.00%	99.90 %
With defect, and port III removed	98.67%	99.97%

From Table 7.1, it is observed that the new design, that includes the inserted defect and has port III removed, is the optimum design, surpassing the other two competitive designs including the structure reported in [73].

7.8 Summary

A new photonic crystal ring resonator design with a single line defect has been proposed to improve the demultiplexing efficiency and wavelength directionality. The CE-ADI-FDTD has been employed to analyse and optimise the performance of a new ring resonator based on photonic crystals. Mode selection operation has been numerically investigated by using 2D CE-ADI-FDTD. It has been demonstrated that the complete power transfer from one port to another can be achieved. The output power ratio has been significantly improved by introducing the line defect at the crossing point between the ring resonator and the WG2. By using CE-ADI-FDTD method waveguide parameters have been optimised to control and manipulate the flow of light in the THz range.

Chapter 8

Conclusions and Future Research Directions

8.1 Conclusions

The work presented in this thesis is concerned with the properties and applications of photonic crystals. Accordingly, the numerical modelling in time domain of PhC based devices for MUX/DEMUX applications has been studied. Three designs in the photonic range and five in the THz range have been considered and compared to counterparts in literature. In Chapter 4, comparisons are made between PML and UPML in the context of the CE-ADI-FDTD technique. This is followed by introducing the

concept of accounting for error discretisation in PML boundaries; this provides rigorous truncation of the computational grid with a gradual attenuation.

Chapter 5 presented an in depth assessment of the newly implemented PML that takes into account the error discretisation. Simulations results have proved the robustness, accuracy, and improvement of the new PML, where reflection coefficient from the boundary of a planar waveguide has been calculated to show the effectiveness of scheme.

In consideration of existing switches based on PhC structure, enhanced alternative designs based on careful geometric tailoring of microcavities have been presented in Chapter 6 to improve the transmission, and sensitivity of such devices.

Chapter 7 has presented the improvement of existing THz region PhC based switches. This was achieved by introducing geometrically tailored defects between an output waveguide and an embedded ring resonator. All simulations were carried out based on the CE-ADI-FDTD method.

8.2 Future Research Directions

The recent burst in telecommunications and their technological advancement has led to a surge in demands for high quality, efficient electronic and optical systems that are extremely fast.

The objective in the near future is two-fold; the development from 2D to 3D photonic crystal switching devices in order to include the analysis of radiation loss and polarisation conversion. Secondly, follow up this research by making use of the properties and characteristics of these designs in surface plasmonic dielectrics [78 - 81].

Research related with PhCs and their performance can be carried out upon surface plasmonic dielectrics in the view of adapting the CE-ADI-FDTD code at hand in order to cope with dispersion within the field. This can then be followed by bridging the gap between PhCs and surface plasmonic dielectrics through validating the work with simulations of an elementary Surface Plasmonic Photonic Crystal (SP-PhC) structure, and designing SP-PhC device applications that are ready for fabrication. The aims and milestones set at the beginning of this project have been met, and the main contributions to knowledge generated in this work can be summarised as follows

1. Became thoroughly familiar with the CE-ADI-FDTD numerical modelling technique and developed numerical technique for minimising discretisation error in PML boundary conditions, successfully implemented them within the CE-ADI-FDTD method, and made a full assessment of its performance.

2. Created novel design MUX/DEMUX photonic crystal based switches for the purpose of optical communication.

3. Carried out the analysis of THz photonic crystal based ring resonators.

4. Offered new highly competitive and highly efficient designs of PhC based THz switches.

References

[1] E. Yablonovitch, “Photonic band-gap structures,” *Optical Society of America*, Vol. 10, no. 2, Feb. 19903.

[2] D. Pinto, S. S. A. Obayya, “Improved Complex-Envelope Alternating-Direction-Implicit Finite-Difference-Time-Domain Method for Photnic-Bandgap Cavities,” *Journal of Lightwave Technology*, Vol. 25, no. 1, Jan. 2007.

[3] Günther Arnold and Henry Kressel, "*Semiconductor Devices for Optical Communication*," Springer, 1987.

[4] S. Johnson, and J. Joannopoulos, "*Photonic Crystals: The Road from Theory to Practice,*" Springer, ed. 1, Jan. 2002.

[5] P. I. Borel, L. H. Frandsen, A. Harpøth, J. B. Leon, H. Liu, M. Kristensen, W. Bogaerts, P. Dumon, R. Baets, V. Wiaux, J. Wouters, and S. Beckx, "Bandwidth engineering of photonic crystal waveguide bends," *Electron. Lett.*, Vol. 40, pp. 1263–1264, 2004

[6] R. Costa, A. Melloni, and M. Martinelli, "Bandpass resonant filters in photonic-crystal waveguides," *IEEE Photon. Technol. Lett.*, Vol. 15, pp. 401–403, 2003

[7] E. Pistono, P. Ferrari, L. Duvillaret, J. L. Coutaz, and A. Jrad, "Tunable bandpass microwave filters based on defect commandable photonic bandgap waveguides," *Electron. Lett.*, Vol. 39, pp. 1131–1133, 2003

[8] P. R. Villeneuve, S. Fan, and J. D. Joannopoulos, "Microcavities in photonic crystals: Mode symmetry, tunability, and coupling efficiency," *Phys. Rev. B, Condens. Matter*, Vol. 54, pp. 7837–7842, 1996

[9] H. M. H. Chong and R. M. De La Rue, "Tuning of photonic crystal waveguide microcavity by thermooptic effect," *IEEE Photon. Technol. Lett.*, Vol. 16, pp. 1528–1530, 2004

[10] A. Mekis, M. Meier, A. DodaBalapur, R. E. Slusher, and J. D. Joannopulos, "Lasing mechanism in two dimensional photonic crystal lasers," *Appl. Phys., A Mater. Sci. Process.*, Vol. 69, pp. 111–114, 1999

[11] O. Painter, R. K. Lee, A. Scherer, A. Yariv, J. D. O'Brien, P. D. Dapkus, and I. Kim, "Two-dimensional photonic band-gap defect mode laser," *Science*, Vol. 284, pp. 1819–1821, 1999

[12] J. C. Maxwell, "A Dynamic Theory of the Electromagnetic Field," Dec. 1864.

[13] http://ab-initio.mit.edu/photons (as of January 2010)

[14] R. Letizia, "*Numerical Modelling of Photonic Crystal Devices for Second Harmonic Generation*," Doctorate Thesis, University of Leeds, 2009.

[15] J. D. Joannopoulos, R. D. Meade, and J. N. Winn, *Photonic Crystals: Molding the Flow of Light, Princeton*, NJ: Princeton Univ. Press, 1995

[16] S. Haussühl, *Physical Properties of a Crystal: An Introduction*, Weinheim: Wiley-VCH, 2007

[17] J.F. Nye, *Physical properties of crystals: their representation by tensors and matrices*, Oxford: Clarendon Press, 1957

[18] D. Pinto, "*Numerical Modelling of Photonic Crystals Devices for All-Optical Signal Processing*," Doctorate Thesis, University of Leeds, 2009.

[19] Jean-Michel Lourtioz , "*Photonic Crystals Towards Nanoscale Photonic Devices*," Springer, 2003

[20] E. Yablonovitch, "Photonic Crystals", *J. Modern Opt.,* Vol. 41, pp. 173-194, 1994

[21] H. M. H. Chong, and R. M. De La Rue, "Tuning of Photonic Crystal Waveguide Microcavity by Thermooptic Effect", *IEEE Photon. Technol. Lett.*, Vol. 16, pp. 1528-1530, 2004

[22] A. Mekis, J. C. Chen, I. Kurland, S. Fan, P. R. Villeneuve, and J. D. Joannopoulos, "High transmission through sharp bends in photonic crystal waveguides", *Phys. Rev. Lett.,* Vol. 77, pp. 3787-3790, 1996

[23] M. Baylindir, B. Temelkuran, and E. Ozbay, "Propagation of photons by hopping: A waveguiding mechanism through localized coupled cavities in three-dimensional photonic crystals", *Phys. Rev. B*, Vol. 61, pp. 11855-11858, 2000

[24] M. Loncar, D. Nedeljkovic, T. Doll, J. Vuckovic, A. Scherer, and T. P. Pearsall, "Waveguiding in planar photonic crystals", *Appl. Phys. Lett.,* Vol. 77, pp. 1937-1940, 2000

[25] C. J. Jin, B. Y. Cheng, B. Y. Man, Z. L. Li, and D. Z. Zhang, "Band gap and wave guiding effect in a quasiperiodic photonic crystal", *Appl. Phys. Lett*., Vol. 75, pp. 1848-1850, 1999

[26] T. Baba, N. Fukaya, and Y. Yonekura, "Observation of light propagation in photonic crystal waveguides with bends", *Electr. Lett.,* Vol. 35, pp. 654-655

[27] Z. Qiang, W. Zhou, and R. A. Soref, "Optical add-drop filters based on photonic crystal ring resonators", *Optics Express*, Vol. 15, pp. 1823-1831, 2007

[28] H. S. Lu, Y. J. Chiang, and L. Wang, "Photonic Crystal Based Optical Add/Drop Multiplexer Using Narrow-Band Reflection Filters", *Jpn. J. Appl. Phys*., Vol. 46, pp. 6898-6902, 2007

[29] M. Koshiba, “Wavelength Division Multiplexing and Demultiplexing with Photonic Crystal Waveguide Couplers”, *J. Lightwave Tech*., Vol. 19, pp. 1970-1975, 2001

[30] S. Haxha, W. Belhadj, F. AbdelMalek, and H. Bouchriha, “Analysis of wavelength demultiplexer based on photonic crystals”, *IEE Proc.-Optoelectron*., Vol. 152, pp. 193-198, 2005

[31] Song, J., and W. C. Chew, “The fast Illinois solver code: Requirements and scaling properties,” *IEEE Comp. Sci. Eng*. Col. 5, July-Sept. 1998, pp. 19-23.

[32] A. Taflove, and S. C. Hagness, *Computational Electrodynamics: the finite-difference time-domain method*, Artech House, 2005

[33] K. Yee, "Numerical solution of initial boundary value problems involving Maxwell's equations in isotropic media," *IEEE Transactions, Antennas and Propagat.* pp. 302–307, 1966.

[34] J. Berenger (1994). "A perfectly matched layer for the absorption of electromagnetic waves". *Journal of Computational Physics*, Vol. 114, pp. 185–200

[35] D. S. Katz, E. T. Thiele, and A. Taflove, "Validation and extension to three dimensional of the berenger PML absorbing boundary condition for FDTD meshes", *IEEE Microw. Guided Wave Lett.*, Vol. 4, no.4, pp. 268 – 270, Aug. 1994

[36] T. Namiki, "3-D ADI-FDTD Method – Unconditionally Stable Time-Domain Algorithm for Solving Full Vector Maxwell's Equations", *IEEE Trans. Microw. Theory Tech.*, Vol. 48, no. 10, pp. 1743 – 1748, Oct. 2000

[37] T. Namiki, and K. Ito, "Investigation of Numerical Errors of the Two-Dimensional ADI-FDTD Method", *IEEE Trans. Microw. Theory Tech.*, Vol. 48, no. 11, pp. 1950 – 1956, Nov. 2000

[38] F. Zheng, and Z. Chen, "Numerical Dispersion Analysis of the Unconditionally Stable 3-D ADI-FDTD Method", *IEEE Trans. Microw. Theory Tech.*, Vol. 49, no. 5, pp. 1006 – 1009, May 2001

[39] F. Zheng, Z. Chen, and J. Zhang "Toward the Development of a Three-Dimensional Unconditionally Stable Finite-Difference Time-Domain Method", *IEEE Trans. Microw. Theory Tech.*, Vol. 48, no. 9, pp. 1550 – 1558, Sept. 2000

[40] A.N. Zhao, "Two Special Notes on the Implementation of the Unconditionally Stable ADI-FDTD Method", *Microw. Opt. Technol. Lett.*, Vol. 33, no. 4, pp. 273 – 277, May 2002

[41] S.S.A. Obayya, B.M.A. Rahman and K.T.V. Grattan, "Accurate finite element modal solution of photonic crystal fibres," *IEE Proc-Optoelectron*, Vol. 152, no. 5, Oct. 2005.

[42] Ju Han Lee and Young-Geun Han, "Novel Dispersion Properties of Photonic Crystal Fiber," *Japanese Journal of Applied Science*, pp. 5408-5413, Aug. 2007.

[43] S.G. García, T.W. Lee, and S.C. Hagness, "On the Accuracy of the ADI-FDTD Method", *IEEE Antennas Wireless Propag. Lett.*, Vol.1, pp. 31 – 34, 2002

[44] M. Koshiba, "Optical Waveguide Analysis," *Advanced Science and Technology Series*, 1990.

[45] H. Rao, R. Scarmozzino, and R. M. Osgood, "An improved ADI-FDTD method and its application to photonic simulations," *IEEE Photon. Technol. Lett.*, Vol. 14, no. 4, pp. 477-479, Apr. 2002

[46] S.S.A. Obayya's seminar titled "New Modelling Techniques for Photonic Crystals," *IIIS University of Leeds*, Feb. 2008.

[47] J.S. Juntunen, and T.D. Tsiboukis, "Reduction of Numerical Dispersion in FDTD Method Through Artificial Anisotropy", *IEEE Trans. Microw. Theory Tech.*, Vol. 48, no. 4, pp. 582 – 588, Apr. 2000

[48] G. Mur, "Absorbing boundary conditions for the finite-difference approximation of the time-domain electromagnetic field equations", *IEEE Trans. Electromagn. Compat.*, Vol. 23, no. 4, pp. 377 – 382, Nov. 1981

[49] L.N. Trefethen, and L. Halpern, "Well-posedness of one-way wave equations and absorbing boundary conditions", *Math. Comp.*, Vol. 47, no. 176, pp. 421 – 435, Oct. 1986

[50] R.L. Higdon, "Numerical absorbing boundary conditions for the wave equation", *Math. Comp.*, Vol. 49, no. 179, pp.65 – 90, Jul. 1987

[51] Z.P. Liao, H.L. Wong, B.P. Yang, and Y.F. Yuan, "A transmitting boundary for transient wave analyses", *Scientia Sinica (series A)*, Vol. XXVII, no. 10, pp. 1063 – 1076, 1984

[52] O.M. Ramahi, "The concurrent complementary operators method for FDTD mesh truncation", *IEEE Trans. Antennas Propagat.*, Vol. 46, no. 10, pp. 1475 – 1482, Oct. 1998

[53] J. P. Berenger, “A perfectly matched layer for the absorption of electromagnetic waves”, *J. Comput. Phys.*, Vol. 114, no. 2, pp. 185 – 200, Oct. 1994

[54] L. Zhao and A. C. Cangellaris, “A general approach for the development of unsplit-field time-domain implementations of perfectly matched layers for FDTD grid truncation”, *IEEE Microw. Guided Wave Lett.*, Vol. 6, no. 5, pp. 209 – 211, May 1996

[55] D. M. Sullivan, “An unsplit step 3-D PML for use with the FDTD method”, *IEEE Microw. Guided Wave Lett.*, Vol. 7, no.7 pp. 184 – 186, July 1997

[56] D. S. Katz, E. T. Thiele, and A. Taflove, “Validation and extension to three dimensional of the berenger PML absorbing boundary condition for FDTD meshes”, *IEEE Microw. Guided Wave Lett.*, Vol. 4, no.4, pp. 268 – 270, Aug. 1994

[57] I.V. Pérez, S.G. García, R.G. Martín, and B.G. Olmedo, “Generalization of Berenger’s Absorbing Boundary Conditions for 3-D Magnetic and Dielectric Anisotropic Media”, *Microw. Opt. Technol. Lett.*, Vol. 18, no. 2, pp. 126 – 130, Dec. 1998

[58] O. Ramadan, "Accuracy improved multi-stage ADI-PML algorithm for dispersive open region FDTD problems", *Electron. Lett.*, Vol. 44, no. 20, pp. 1168 – 1170, Sept. 2008

[59] Sacks, Z. S., D. M. Kingsland, R. Lee, and J. F. Lee, "A perfectly matched anisotropic absorber for use as an absorbing boundary condition," *IEEE Trans. Antennas Propagat.*, Vol. 43, pp. 1460 – 1463, 1995.

[60] S. Wang, and F.L. Teixeira, "An efficient PML implementation for the ADI-FDTD method", *IEEE Microw. Wireless Comp. Lett.*, Vol. 13, no. 2, pp. 72 – 74, Feb. 2003

[61] J. M. Lopez-Villegas and N. Vidal, "Modelling and minimization of discretisation error in one-dimensional PML's using FDTD," *IEEE*, 2007.

[62] Theodor Tamir, "*Guided-Wave Optoelectronics*", Springer-Verlag., Springer Series in Electronics and Photonics, Vol. 96, ed. 2, Apr. 1990

[63] Ju Han Lee and Young-Geun Han, "Novel Dispersion Properties of Photonic Crystal Fiber," *Japanese Journal of Applied Science,* pp. 5408-5413, Aug. 2007.

[64] Y. Shi, D. Daoxin, and S. He, "Novel Ultracompact Triplexer Based on Photonic Crystal Waveguides," *IEEE Photon. Technol. Lett.*, Vol. 18, pp. 2293-2295, 2006.

[65] F. Chien, S. Cheng, Y. Hsu, and W. Hsieh, "Dual-band multiplexer/demultiplexer with photonic-crystal waveguide couplers for bidirectional communications," *Optics Communications*, Vol. 266, no. 2, pp. 592–597, 2006.

[66] F. Chien, Y. Hsu, W. Hsieh, and S. Cheng, "Dual wavelength demultiplexing by coupling and decoupling of photonic crystal waveguides," *Optics Express*, Vol. 12, no. 6, pp. 1119–1125, 2004.

[67] Y. Lee, "*Principles of Terahertz Science and Technology,*" Springer, 2009

[68] H. Chen, Padilla, J. Zide, A. Gossard, A. Taylor, and R. Averitt, "Active terahertz metamaterials devices," *Nature*, Vol. 444, pp. 597 – 600, 2006.

[69] B. Gang, W. Huajuan, Y. Dongxiao, L. Shenggang, and C. Kangsheng, "Theoretical study on THz components and systems based on photonic crystals," *12th International Conference on Terahertz Electronics*, Karlsruhe, Germany, pp. 687 – 688, 2004.

[70] D. Woolard, E. Brown, M. Pepper, and M. Kemp, “Terahertz frequency sensing and imaging: a time of reckoning future applications,” *Proc. IEEE*, Vol 93, pp. 1722 – 1743, 2005.

[71] M. Shur, “Terahertz technology devices and applications,” *Solid-State Device Research Conference,* ESSDERC, France, pp. 13 – 21, 2005.

[72] H. Kurt, and D. Citrin, “New approaches in biochemical sensing using photonic crystals in the terahertz region,” *13th International Conference on Terahertz Electronics*, Williamsburg, USA, pp. 36 – 37, 2005.

[73] A. R. Maleki Javan, and N. Granpayeh, “Terahertz wave switch based on photonic crystal ring resonators,” *Opt Quant Electron*, Springer, 2008.

[74] Xomalin G. Peralta, Evgenya I. Smirnova, Abul K. Azad, Hou-Tong Chen, Antoinette J. Taylor, Igal Brener, and John F. O'Hara, "Metamaterials for THz polarimetric devices," *Opt. Express*, Vol. 17, pp. 773-783, 2009.

[75] Zhan Fu Qiaoqiang Gan Ding, Y.J. Bartoli, F.J., “From Waveguiding to Spatial Localization of THz Waves Within a Plasmonic Metallic Grating,”, *IEEE J. Quantum Electron*., Vol. 14, No. 2, pp. 486-490, 2008.

[76] N. Jukam and M. S. Sherwin, "Two-dimensional terahertz photonic crystals fabricated by deep reactive ion etching in Si," *Appl. Phys. Lett.* Vol. 83, pp. 21–23, 2003.

[77] W. Chiu, T. Huang, Y. Wu, Y. Chan, C. Hou, H. Chien, et al. "A photonic crystal ring resonator formed by SOI nano-rods," *Opt. Express*, Vol. 15, pp. 1500 – 1506, 2007.

[78] J. Shibayama, R. Takahashi, J. Yamauchi, and H. Nakano, "Frequency-Dependent LOD-FDTD Implementation With a Combined Dispersion Model for the Analysis of Surface Plasmon Waveguides," *MEXT, Grant-in-Aid for Scientific Research*, 2007.

[79] D. Kelley, R. Luebbers, "Peicewise Linear Recursive Convolution for Dispersive Media Using FDTD," *IEEE Trans., Antennas and Propagat*., Vol. 44, No.6, Jun. 1996.

[80] O. Ramadan, "Unsplit field implicit PML algorithm for complex envelope dispersive LOD-FDTD simulations," *Electronsic. Lette.*, Vol. 43, No. 5, Mar. 2005.

[81] S. Staker, C. Holloway, A. Bhobe, M. Piket-May, "Alternating-Direction Impilcit (ADI) Formulation of the Finite-Difference Time-Domain (FDTD)

Method: Algorithm and Material Dispersion Implementation," *IEEE Trans. on Electromagnetic Compatibility*, Vol. 45, No. 2, May. 2003.

List of Publications

As a result of hard work and intensive research throughout the duration of this PhD, several journal papers and conference papers have been submitted, accepted for publication, and presented. The journal papers are listed below

- R Selim, D Pinto, and S S A Obayya, “Improved Design of Photonic Crystal Based Multiplexer/Demultiplexer Devices,” accepted for publication in the Special Issue of IET Optoelectronics.

- R Selim, D Pinto, and S S A Obayya, “Ultra Fast Terahertz Switching Ring Resonator Based on Photonic Crystals,” submitted to IEEE Journal of Selected Topics in Quantum Electronics, and awaiting acceptance.

- R Selim, D Pinto, and S S A Obayya, "Novel Fast Photonic Crystal Multiplexer-Demultiplexer Switches," submitted to Optical and Quantum Electronics, awaiting acceptance.

And the conferences papers are listed below

- R Selim, D Pinto, and S S A Obayya, "Terahertz Ultra Fast Switching Device Based Photonic Crystals," submitted to the Semiconductor and Integrated Optoelectronics, SIOE'10, Cardiff, 2010.

- R Selim, D Pinto, and S S A Obayya, "THz Switches Based on PhCs," submitted to the International Workshop on Optical Waveguide Theory and Numerical Modelling, OWTNM'10, Cambridge, 2010.

- R. Selim, D Pinto, and S S A Obayya, "Ultra-Fast Photonic Crystal Based Terahertz Switches," presented at UK Semiconductors, Sheffield, July 2009.

- R Selim, D Pinto, and S S A Obayya, "Analysis of a 3 × 1 Demultiplexer Photonic Crystal Using CE-ADI-FDTD," presented at the International Workshop on Optical Waveguide Theory and Numerical Modelling, OWTNM'09, Jena, Germany, April 2009.

- R Selim, D Pinto, and S S A Obayya, "Analysis of New Ultra-Fast Photonic Crystal MUX/DEMUX," presented at the Semiconductor and Integrated Optoelectronics, SIOE'09, Cardiff, April 2009.

- R Selim, D Pinto, and S S A Obayya, "Ultra-Fast Photonic Multiplexer-Demultiplexer Switches," presented at the First International Workshop on Theoretical and Computational Nano-Photonics, TaCoNa-Photonics 2008, Physikzentrum Bad Honnef, Germany, December 2008.

- R Selim, D Pinto, and S S A Obayya, "MUX/DEMUX Based on Photonic Crystals," presented at the 8th International Conference for Numerical Simulations of Optoelectronic Devices, NUSOD08, Nottingham, September 2008.

- R Selim, D Pinto, and S S A Obayya, "Complex Envelope Alternating Direction Implicit Finite Difference Time Domain Analysis of Ultra-Fast Photonic Bandgap Switches," presented at the Semiconductor and Integrated Optoelectronics, SIOE'08, Cardiff, April 2008.